


ENSURING NAVIGATION INTEGRITY AND CONTINUITY USING
MULTI-CONSTELLATION GNSS

BY
YAWEI ZHAI

Submitted in partial fulfillment of the
requirements for the degree of
Doctor of Philosophy in Mechanical and Aerospace Engineering
in the Graduate College of the
Illinois Institute of Technology

Approved 

Advisor

Approved 

Co-Advisor

Chicago, Illinois
May 2018

© Copyright by
YAWEI ZHAI
May 2018

ACKNOWLEDGMENT

I would like to thank my advisor and dissertation committee chair, Professor Boris Pervan, for giving me the opportunity to get into this research field. His broad vision, comprehensive knowledge and clear guidance not only helped me breakthrough various barriers to make this thesis possible, but also educated me the general methods to pursue research work, which will benefit my entire career. I would also like to thank my co-advisor and committee member, Professor Mathieu Joerger, for his enthusiasm, encouragement, and patience when guiding me at the first two years after I joined the navigation lab without any relevant background knowledge. Thank the rest of my committee: Professors Kevin Cassel, Seebany Datta-Barua, and Yongyi Yang.

I gratefully acknowledge the Federal Aviation Administration (FAA) for sponsoring this research. Thank Dr. Juan Blanch, Dr. Todd Walter, Dr. Carl Milner and Dr. Young Lee for their valuable suggestions, comments and feedbacks throughout my doctoral study. It had been a great honor to cooperate with them under the same working group.

I must thank all my fellow colleagues in the Navigation and Guidance Laboratory: Dr. Samer Khanafseh, Dr. Michael Jamoom, Dr. Cagatay Tanil, Dr. Jing Jing, Dr. Stefan Stevanovic, Adriano Canolla, Jaymin Patel, Wengxiang Zhao, Santiago Perea, Ryan Cassel, Tejas Desai, Raisa Vitto, Soowon Kim, Shahriar Kiarash, Elisa Gallon for their friendship and assistance.

To my friends, Dr. Jun Cao, Dr. Ming Yin, Dr. Yang Zhou, Dr. Yang Su, Dr. Mateos Kassa, Dr. Ningchao Wang, Dr. Peng Zhao, Shan-ju Chiang, Jingyan Wang, Siwei Dong, Jialiang Wei, Hui Jia, Yuanchang Gao, Wenbo Sui, Roohollah Parvizi. Their accompany had made my stay in Chicago be a memorable time with full of happiness and enjoyment.

I can never thank enough to my parents, Yuxia Xu and Dejun Zhai. It is their endless love and encouragement that keep motivating me. Any success of mine is a testament to them. I would also like to thank my sister, Dr. Yaxin Zhai, for her support and for suggesting PhD pursuit at the time when I was searching for a direction. To all the other family members in my home country, who never stopped encouraging me, I owe a great debt. Finally and most importantly, I want to thank Wen Yuan Hou, the woman of my life, for accompanying me through the daily joys and upsets of this adventure.

TABLE OF CONTENTS

	Page
ACKNOWLEDGEMENT	iii
LIST OF TABLES	viii
LIST OF FIGURES	x
ABSTRACT	xi
CHAPTER	
1. INTRODUCTION	1
1.1. GNSS Background	1
1.2. Navigation Integrity and Continuity	6
1.3. Research Motivation	8
1.4. Prior Work	9
1.5. Advanced RAIM	11
1.6. Dissertation Outline and Contributions	12
2. ARAIM FUNDAMENTALS	16
2.1. Navigation Requirements	16
2.2. Integrity Support Message	20
2.3. Measurement Model and Least-Squares Estimation	21
2.4. Baseline Fault Detection User Algorithm	23
2.5. Parity Space	32
2.6. Navigation Performance of ARAIM Detection Function	35
3. QUANTIFYING CONTINUITY RISK	39
3.1. Causes of Loss of Continuity	39
3.2. Continuity Risk Contribution of Fault Occurrence	40
3.3. Need for Exclusion Function	43
3.4. Requirements for Exclusion Function	47
3.5. Loss of Continuity Contribution of Unscheduled Satellite Out- ages	49
4. FAULT EXCLUSION SCHEME	53
4.1. Real-Time FDE Algorithm	53
4.2. Evaluating FDE Thresholds	57
4.3. Bounding the Instantaneous Integrity Risk	58

4.4. Predictive Integrity Risk	61
5. MULTI-CONSTELLATION ARAIM NAVIGATION PERFORMANCE	63
5.1. Achievable V-ARAIM FD Navigation Performance with Multiple Constellations	64
5.2. Sensitivity Analysis of V-ARAIM FD Navigation Performance to ISM	65
5.3. Overall ARAIM Performance Using Both Detection and Exclusion	67
5.4. Impact of USO on Navigation Performance	69
6. IMPACT OF TEST STATISTIC TIME CORRELATION ON INTEGRITY AND CONTINUITY	71
6.1. Actual Integrity Risk over the Exposure Time	71
6.2. Actual False Alarm Probability over the Exposure Time	75
6.3. Characterizing Time Correlation of Measurement Error	77
6.4. Analytical Results	79
6.5. Experimental Results Using Collected Data	80
7. OFFLINE GROUND MONITOR TO VALIDATE ISM	83
7.1. Offline Monitor Concept and Required Performance	83
7.2. Offline Monitor Architecture	86
7.3. Estimator Design	90
7.4. Monitor Performance Analysis	93
8. CONCLUSION	100
8.1. ARAIM Navigation Performance	100
8.2. ARAIM Offline Monitor Performance	101
8.3. Summary of Achievements	101
8.4. Recommendations for Future Work	102
8.5. Closing	104
APPENDIX	105
A. DERIVATION OF EQUATIONS TO COMPUTE FDE THRESHOLDS USING NON-EQUAL $C_{REQ,H}$ ALLOCATION	105
B. DERIVATION OF THE ACTUAL FA PROBABILITY UPPER BOUND	108
C. DERIVATION OF THE AUTOCORRELATION FUNCTION OF THE USER ERROR	111

D. DERIVATION OF THE AUTOCORRELATION FUNCTION OF THE SIGNAL-IN-SPACE ERROR	117
E. CHARACTERIZING THE USER ERROR PROFILE OF THE IIT ARAIM PROTOTYPE	120
F. KALMAN FILTER APPROACH FOR THE OFFLINE GROUND MONITOR	122
BIBLIOGRAPHY	124

LIST OF TABLES

Table	Page
2.1 Integrity and Continuity Requirements for ARAIM Operations . . .	17
2.2 V-ARAIM Accuracy and EMT Requirements	19
2.3 Baseline Simulation Conditions of Dual-Constellation ARAIM . . .	38
3.1 V-ARAIM Continuity Budget Allocation	44
3.2 H-ARAIM Continuity Budget Allocation	48
3.3 H-ARAIM Continuity Budget Allocation among OF and USO Con- ditions	52
5.1 99.5% Availability Coverage Using Constellations with Equivalent Performance to GPS	65
5.2 99.5% Availability Coverage Using Constellations with Equivalent Performance to GPS	67
5.3 99.5% Availability Coverage Using Constellations with Currently Broad- cast GPS σ_{URA}	67
7.1 Maximum σ_{SISRE} Values under Four Scenarios	96

LIST OF FIGURES

Figure	Page
1.1 GNSS Architecture.	3
1.2 Joint Constellation of Future GNSS (Figure Courtesy of Dr. M. Joerger).	5
1.3 Navigation Integrity Interpretation.	7
2.1 Interpretation of SS Test Statistics.	26
2.2 Parity Space Representation of ARAIM Fault Detection.	34
2.3 Baseline V-ARAIM FD Worldwide Availability Performance.	36
2.4 Baseline H-ARAIM FD Worldwide HPL Map.	37
3.1 Two Categories of the LOC Sources.	40
3.2 Probability Bound of LOC due to Fault with Varying Numbers of Measurements.	45
3.3 P_{sat} vs. P_{const} for One Constellation to Meet the Allocated Continuity Requirement.	46
3.4 H-ARAIM LOC Tree.	50
4.1 Flow Diagram of the Real-Time FDE Process.	54
4.2 Parity Space Representation of ARAIM FDE Algorithm.	56
5.1 Achievable VPL Levels (in meters) Using Constellations with Equivalent Performance to GPS.	64
5.2 Achievable VPL Levels (in meters) Using Constellations with ISM Values in Set 1.	66
5.3 Achievable VPL Levels (in meters) Using Constellations with ISM Values in Set 2.	66
5.4 Achievable VPL Levels (in meters) Using Constellations with Currently Broadcast GPS σ_{URA}	67
5.5 VPL Map (in meters) Using Four-Constellation V-ARAIM FDE.	68
5.6 H-ARAIM Availability Map Using Dual-Constellation ARAIM FDE.	68
5.7 Overall H-ARAIM Availability when Accounting for Single SV USO.	69

5.8	Overall H-ARAIM Availability when Accounting for Multiple SV USO.	70
6.1	Numbers of TTAs and Time Epochs over the Exposure Interval. . .	72
6.2	HMI Events over the Exposure Interval.	72
6.3	H-ARAIM P_{FA} over 1 hour.	79
6.4	H-ARAIM HPL Maps by Increasing the Detection Threshold. . .	80
6.5	H-ARAIM FA Probability Evaluated Using Experimental Data. . .	81
7.1	$\sigma_{VALIDATE}$ vs. $\sigma_{MONITOR}$ over Varying σ_{ACTUAL} Values.	86
7.2	All Existing SBAS Stations (Left) and Example Network of 20 RS Used in This Work (Right) (Figure Courtesy of Dr. Michael Jamoom).	87
7.3	Covariance Matrix Projections along LOS for All Locations. . . .	94
7.4	Example Profiles of Error Deviations along One Fitting Interval for Case 1 (Left) and Case 4 (Right).	95
7.5	Maximum σ_{SISRE} over One Day (Left) and Their Distribution (Right) for Case 4.	95
7.6	Best Fit Residual SISRE Orbit over One Day.	98
7.7	Residual SISRE Orbit Ranges.	98
7.8	Residual SISRE Orbit Overbound.	99
C.1	Airborne Mean and Standard Deviation.	112
C.2	Airborne Autocorrelation Traces.	113
C.3	Airborne Autocorrelation Distributions at Various Lag Times. . .	114
D.1	Monthly 95 % Bound of User Position Error on Each Satellite (Fig- ure Courtesy of Dr. Todd Walter).	118
D.2	Autocorrelation of SIS Error for Two Example Satellites (Figure Courtesy of Dr. Todd Walter).	118
D.3	SIS Error Autocorrelation Ratios.	119
E.1	CMC CDF Using Data Collected by IIT Prototype.	121

ABSTRACT

Global navigation satellite system (GNSS) measurements are vulnerable to faults including satellite and constellation failures, which can potentially lead to catastrophic consequences in safety-critical applications. To mitigate their impact, receiver autonomous integrity monitoring (RAIM) fault detection has been designed and used in aviation as a backup navigation tool. Future GNSS has been foreseen to provide dramatically increased measurement redundancy and reduced measurement error. These crucial developments, together with important advancements in the RAIM concept itself, will open the possibility to independently support aircraft navigation using GNSS, from takeoff, through en-route flight and final approach to landing, with minimal investment in ground infrastructure. Therefore, this research focuses on developing new dual-frequency, multi-constellation advanced RAIM (ARAIM) fault detection and exclusion methods to ensure high navigation integrity and continuity.

In this thesis, the theoretical basis is established to quantify the impact of fault events and unscheduled satellite outages on continuity risk. Accordingly, the need for airborne fault exclusion is assessed, and the requirements for the exclusion function itself are specified. To improve continuity, a new fault exclusion scheme is developed, for which the real-time implementation of the algorithm is described and the associated integrity risk bound is derived. With the theoretical methods being fully characterized, this thesis comprehensively quantifies the achievable ARAIM navigation performance over various numbers and qualities of constellations. The results show that high service availability can be achieved using multi-constellation GNSS, while meeting both integrity and continuity requirements. Furthermore, this work investigates the impact of test statistic time correlation on integrity and continuity risk, and rigorously derives the new methods to evaluate the actual risk over the exposure time. The results show that the false alarm probability is two orders of magnitude

higher than previously thought. A feasible solution to resolve this issue at the user receiver is provided, and the performance is analyzed.

The most significant new feature of ARAIM is the integrity support message (ISM), which provides assertions on the GNSS signal-in-space performance. This dissertation describes the design, analysis, and evaluation of the offline ground monitor, which aims at validating the ISM broadcast to the users. The proposed architecture utilizes a worldwide network of sparsely distributed reference stations, and parametric satellite orbital models to estimate the satellite position and clock. Two separate analyses, covariance analysis and model fidelity evaluation, are carried out to respectively quantify the impact of measurement errors and of residual model errors on the estimation. The results indicate this ground monitor design is adequate for ARAIM ISM validation.

CHAPTER 1

INTRODUCTION

The main challenge when using global navigation satellite systems (GNSS) in safety-critical civil aviation applications is to mitigate the integrity threats caused by measurement faults [1]. For the single constellation case, using the global positioning system (GPS) only, fault detection (FD) has been implemented using receiver autonomous integrity monitoring (RAIM) [2, 3, 4]. The core principle of RAIM is to exploit redundant measurements to achieve self-contained FD at the user receiver [11]. Nowadays, four GNSS constellations are becoming available for aviation users, which will provide many more satellites in view than we have available today using GPS alone. This crucial development in GNSS, together with important advancements in the RAIM concept itself, will open the possibility to independently support aircraft navigation using GNSS, from takeoff, through en-route flight and final approach to landing, with minimal investment in ground infrastructure. Therefore, this dissertation focuses on developing new dual-frequency, multi-constellation advanced RAIM (ARAIM) fault detection and exclusion (FDE) methods to ensure high navigation integrity and continuity.

1.1 GNSS Background

During the last two decades, GNSS have been significantly developed worldwide. As the leading pioneer, the GPS has been widely used for various civilian and military applications. In the near term, four constellations including GPS (U.S.), GLONASS (Russia), Galileo (European Union) and Beidou (China) are expected to finish their modernizations and/or full deployments [12], which brings satellite based navigation into a new era. Currently, the unprecedented research interest in

autonomous system technology, together with the historically consistent and reliable performance of GNSS, have motivated the expansion of GNSS in safety-critical applications.

1.1.1 GNSS Principle. As shown in Figure 1.1, GNSS architecture is composed of three segments: the space segment, the control segment, and the user segment [10]. For GPS, the space segment consists of 31 medium Earth orbit (MEO) satellites distributed in six orbital planes at 55 degree inclinations. Each satellite circles the Earth twice a day, and transmits signals in L band radio frequency range. These signals carry the information of ranges (i.e., distances) from the users to the satellites, and provide navigation messages that can be used to identify each satellite and determine its position.

The control segment includes a master control station, satellite monitor stations, and data upload antennas. The monitor stations track satellites and collect the navigation signals. The master control station computes the satellite orbit predictions and generates navigation messages. The data are then uploaded to each satellite by the ground antennas at least once a day.

The user segment is composed of all civilian and military users, for which the applications vary from personal cellphone navigation to shipboard landing at an aircraft carrier. The GNSS user receivers receive the signals broadcast by the satellites, decode the navigation messages, and compute the user positions.

GNSS positioning relies on the concept of multilateration. At the user receiver, one GNSS measurement gives the distance from itself to a known satellite location. With a certain number of such measurements, the receiver can solve for its position. In principle, a minimum of three measurements are required to obtain the three-dimensional user position. However, the method that receiver employs to

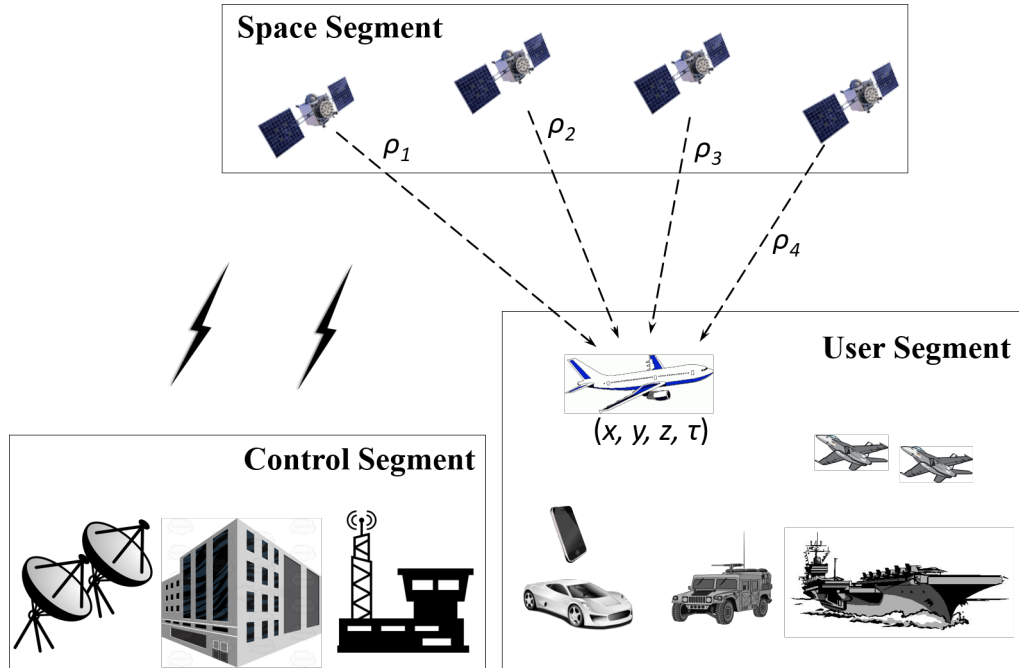


Figure 1.1. GNSS Architecture.

determine the distance is by differencing the time at signal emission from satellites and time-of-arrival at the receiver. Since most users are only equipped with low-cost quartz oscillator clocks, their deviations from GNSS time may invalidate the position estimates. Therefore, an additional unknown parameter, the receiver clock bias, is introduced to synchronize the clocks between users and satellites. In addition, although the satellite clocks of the same constellation are well synchronized, each constellation has its own unique GNSS time standard. As a result, the number of unknown clock biases to be estimated is equal to the number of constellations used for positioning. So, the minimum number of satellites to provide navigation service is three plus the number of constellations. In Figure 1.1, the links between the aircraft and the space segment briefly illustrate a GNSS positioning example using one constellation. In this case, at least 4 ranging measurements (ρ_1 to ρ_4) are required to estimate the aircraft position x, y, z and the receiver clock bias τ .

1.1.2 Current and Future GNSS. The GPS project was launched by the U.S.

Department of Defense (DoD) in the early 1970s, and the constellation is now operated by the US Air Force Space Command. It is the most mature GNSS and has been used worldwide since it started to provide full coverage service in 1995. Despite its consistent and reliable navigation performance history, the evolution of GPS has never stopped. Currently, the modernization of GPS is on-going. So the 31 in-orbit GPS satellites is a mix of old and new ones distinguished by block types. With the last block IIA satellite decommissioned in 2016, all the 12 currently operational legacy satellites are from block IIR. The remaining 19 are modernized satellites, which provide improved accuracy, signal strength and quality over the legacy ones, belong to blocks IIR-M and IIF. Moreover, the next generation of GPS block III satellites is in development, and the first launch is planned in 2018.

The major goal of the GPS modernization is adding new navigation signals to the constellation. Other than the legacy L1 C/A signal, the future modernized GPS will provide three more signals for civilian users including L2C, L5, and L1C. These signals enable the receivers to cancel the first-order ionospheric delay, which is the largest error source affecting the GNSS measurements [10]. Therefore, navigation accuracy can be significantly improved. According to [14], the L2C signal is designed specifically for commercial applications, and it had been broadcast since 2005. The L5 signal is of the most interest in this dissertation because it is intended to serve for safety-critical applications such as civil aviation. In 2010, the first GPS IIF satellite with a full L5 transmitter was launched, and all satellites launched since then are broadcasting L5 signal. As the new generation civilian signal, L1C is planned to be broadcast by GPS block III satellites. The key new feature of L1C is its interoperability among GPS and other satellite navigation systems such as Galileo and Beidou.

Also born in 1970s, the Russia's GLONASS is almost at the same age as GPS.

Even though the constellation had achieved full operational capability in 1995, it fell into disrepair since the late 1990s, due to the economic crisis of Russia. It was not until 2011 when the full constellation of 24 satellites was restored, and these satellites are now in three orbital planes inclined at 65 degrees to provide better satellite visibility in high latitudes. Unlike GPS, whose signals are code division multiple access (CDMA), GLONASS uses frequency division multiple access (FDMA) signals, transmitted in both L1 and L2 frequencies. New GLONASS CDMA signals have been developed and scheduled to be broadcast by the GLONASS-K2 satellites in 2018.

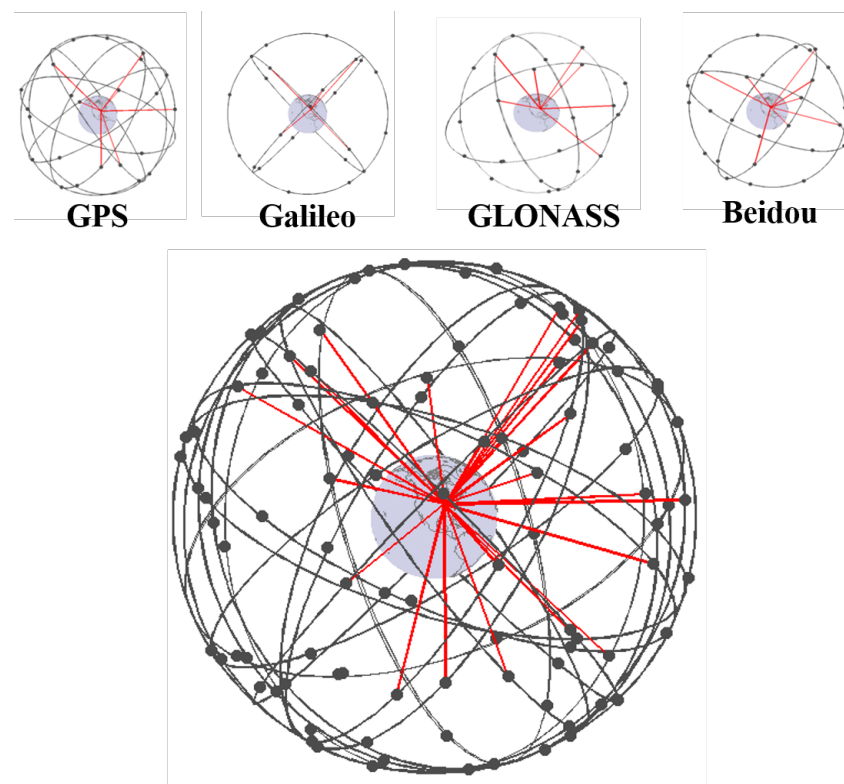


Figure 1.2. Joint Constellation of Future GNSS (Figure Courtesy of Dr. M. Joerger).

Other than these two fully operational constellations, GPS and GLONASS, the European Union (E.U.) and China have both started their own satellite navigation projects, respectively named Galileo and Beidou. Both constellations are currently under construction, and both are expected to be completed by 2020 [12]. A full constellation of Galileo is composed of 30 MEO satellites distributed in three orbital

planes. A full Beidou constellation consists of total 35 satellites including 5 in geostationary orbit (GEO), 3 in inclined geosynchronous orbit (IGSO) and 27 in MEO. Because these two constellations are being developed after GPS and GLONASS, their designs have taken advantage of prior experience of these GNSS developments. Once completed, both Galileo and Beidou will directly broadcast modernized GPS-equivalent CDMA signals on multiple frequencies for civilian users.

In summary, future multi-constellation GNSS will provide greatly increased number of measurements with modernized signals on multiple frequencies. After all four constellations have finished their modernization and full deployment, it is expected that any user on earth will see 25 to 35 visible satellites at all times. Figure 1.2 shows an example of satellite visibility at Chicago, U.S.A. The red thick lines represent the signals received from the satellites in multiple constellations.

1.2 Navigation Integrity and Continuity

The safety critical aviation has stringent requirements on navigation systems. To quantify their performance, the international civil aviation organization (ICAO) has respectively specified the metrics for different navigation methods [22]. Among these metrics, accuracy is the most intuitive one, which measures the navigation output deviation from the true position. However, using satellite based navigation, accuracy requirement can usually be satisfied without great difficulty; instead, the two most challenging requirements are navigation integrity and continuity, which are the main focus of this research effort.

Integrity is a measure of trust that can be placed in the correctness of the information supplied by the navigation system [22]. Integrity risk is defined as the probability that an undetected navigation system error results in hazardous misleading information (HMI), which is the situation where an undetected positioning error

exceeds a predefined alert limit (AL). Loss of integrity (LOI) in aviation navigation can result in catastrophic consequences, so the integrity requirement I_{REQ} is of the greatest significance during any phase of aircraft flight.

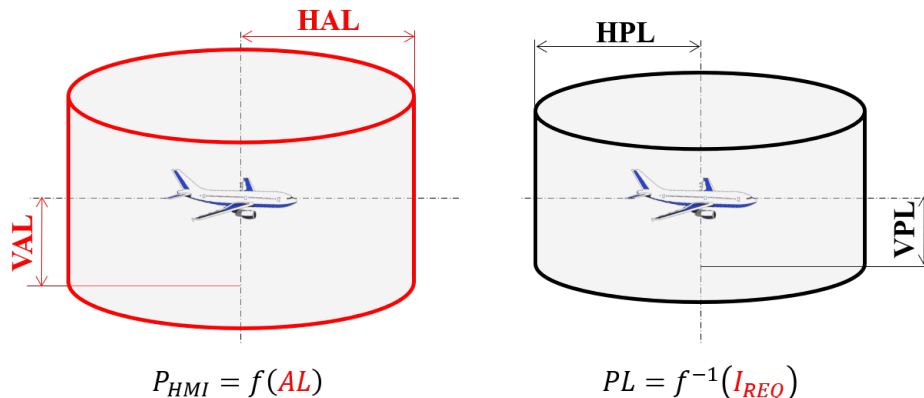


Figure 1.3. Navigation Integrity Interpretation.

Figure 1.3 interprets the integrity concept in two ways. Both cylinders are centered at the actual aircraft position. On the left figure, the red cylinder is predefined respectively by the horizontal AL (HAL) and vertical AL (VAL). As a function of the ALs, the integrity risk P_{HMI} is the probability that the GNSS position estimate locates outside of it. Alternatively, as shown on the right figure of 1.3, integrity can be interpreted from the perspective of protection level (PL). Using this approach, a black cylinder is defined such that the probability that the aircraft is outside of it is equal to I_{REQ} , and the PLs in each dimension are the horizontal PL (HPL) and vertical PL (VPL). The aircraft is regarded to be operating safely only if all neither PL exceeds its corresponding ALs.

In addition to integrity, navigation continuity is another crucial metric; it measures the capability of the system to perform its function without unscheduled interruptions during the intended operation. Continuity risk, or probability of loss of continuity (LOC), is the probability of a detected but unscheduled navigation function interruption after an operation has been initiated [22]. There are many

sources that can lead to LOC event, and all of the them need to be properly accounted for or limited in order to meet the specified requirement C_{REQ} . For the cases where alternative navigation tools are not available, LOC can lead the aircraft to be left without means of navigation, which is another severe threat to safety.

1.3 Research Motivation

At the time when GPS was originally designed, one of the main intended applications was civil aviation. Even though existing aviation navigation systems had historically provided consistent performance with an excellent safety record, many limitations and problems exist. For example, aircraft are restricted to pathways dictated by ground based radio navigation, which limits the airspace capability and increases the fuel and time cost [13]. Also, current systems for aircraft approach such as the instrument landing system (ILS) only support straight approaches. So aircraft need to take turns in starting approaches when the airspace complexity becomes heavier. With satellite navigation available for aviation users, the aircraft can fly directly from point to point using the most fuel-efficient path. It also enables aircraft to fly closer to increase the arrival and departure rates. Moreover, GNSS provides flexibility to optimally design new flight procedures such as optimized profile decent and en-route flight. Most importantly, GNSS enables curved approaches, and helps aircraft land in mountainous terrain where signals transmitted from the ground are usually obstructed or reflected. Therefore, it is imperative to apply GNSS in aviation field.

One major problem potentially affecting GNSS measurements is they are vulnerable to faults, including satellite and constellation failures, which will result in large position estimate error. There are many factors that can lead to faults, such as satellite clock anomalies, mistakes in orbit determination from the control segment, or sudden space environment changes [1]. The probability of fault occurrence

is generally small: for example, the GPS constellation service provider (CSP) has successfully limited the number of satellite faults to be less than three per year. With such a small likelihood, this issue is of little concern in many applications, such as in car or cellphone navigation. However, despite the low fault rate and its downtrend over the last decade, there have been several GPS satellite faults observed since 2009 [27, 30]. Moreover, GLONASS experienced a serious constellation failure that lasted for more than 10 hours in 2014 [15]. It is widely understood that such faults could occur in any other GNSS constellation as well. Therefore, the main challenge when using multi-constellation GNSS in aviation applications is to mitigate the integrity threats caused by measurement faults.

GNSS service can also be interrupted by many sources, including fault detection, satellite outages, radio frequency interference, ionospheric scintillation, etc [37]. Such interruptions can significantly reduce navigation continuity. Because future GNSS will serve as the main source for navigation, the importance of continuity has increased. In response, this research focuses on developing new methods to ensure high navigation integrity and continuity for aviation users.

1.4 Prior Work

There has been a lot of research effort put into improving GNSS navigation performance, and the outcomes have been serving aviation well [4, 6, 7]. All the current existing satellite navigation tools for aircraft use only the GPS constellation, although they are generally called GNSS augmentation techniques because they are in principle applicable to other constellations as well. Depending on where the augmentations are implemented, these systems can be assigned to one of the following three categories: aircraft based augmentation systems (ABAS), ground based augmentation systems (GBAS), and satellite based augmentation systems (SBAS).

The concept of ABAS had been proposed at the very start of the full operation of GPS. It only uses on-board equipment to meet the required navigation performance, so it has no coverage limitations. The most widely used ABAS is RAIM, which achieves self-contained FD by exploiting redundant measurements at the user receiver. RAIM became operational in the mid-1990s as a backup navigation tool to support aircraft en-route flight using GPS only. According to ICAO regulations, all the on-board GNSS receivers are required to have RAIM capability. However, due to the limited satellite redundancy from a single constellation, RAIM is only able to provide limited availability, and can only support operations with less stringent navigation requirements.

GBAS is a type of differential GNSS systems [10]. It is designed to support aircraft approach and landing, so it only serves the airport region. The principle of GBAS is using the ground infrastructures to generate differential correction messages and integrity parameters, and then broadcast the information to the aircraft in a very high frequency band (VHF) band. The information provides high accuracy and integrity, which opens the possibility to achieve up to the most stringent category III precision landing.

In comparison with GBAS, SBAS can provide services for all phases of flight (except precision landing) within a continent-wide area. SBAS also relies on a ground segment to generate corrections and compute integrity. But it uses geostationary satellites to broadcast the information so it benefits all the users within the satellite coverage. The wide area augmentation system (WAAS), the most mature operational SBAS, can now provide both horizontal and vertical navigation for approach operations at all locations in the U.S. However, SBAS also has many disadvantages, including its limited regional application, over-reliance on the ground infrastructures,

as well as the high cost to establish the communication links.

1.5 Advanced RAIM

As discussed in Section 1.1.2, future multi-constellation GNSS will provide many more satellites in view than we have available using GPS alone. In addition, the application of dual-frequency signals will remove the largest measurement error caused by ionospheric delay. Moreover, the satellite clock and ephemeris errors have been significantly reduced in the past decade [26], which in turn improves navigation accuracy. All these developments in GNSS, together with important advancements in the RAIM concept itself, will open the possibility to independently support aircraft navigation using GNSS, from takeoff, through en-route flight and final approach to landing, with minimal investment in ground infrastructure. Therefore, considerable effort has recently been expended, especially in the E.U. and the U.S. [9, 19, 20, 21, 8], to develop new dual-frequency, multi-constellation ARAIM fault detection and exclusion methods. In 2004, an agreement was signed between U.S. and E.U. on GPS/Galileo cooperation. The agreement foresaw a working group on developing dual-constellation based ARAIM services for aviation, was formed as working group C (WG-C) in 2010. As a member of WG-C, this research effort is motivated by using GPS/Galileo constellations, but the methods derived in this dissertation can also be extended to multi-constellation applications.

Currently, two versions of ARAIM, corresponding to two different operational scenarios are being investigated [21]. Vertical ARAIM (V-ARAIM) is intended to meet localizer precision requirements for aircraft landing with vertical guidance down to 200 feet altitude (LPV-200). LPV-200 approach is a relatively new operation proposed by Federal Aviation Administration (FAA) and it has the most stringent navigation requirements among the SBAS-achievable operations. Even though LPV-200 has similar landing procedures as ILS category I including same decision height

and visibility, it is still considered a non-precision approach due to its larger VAL of 35 m. Other than V-ARAIM, horizontal ARAIM (H-ARAIM) aims at providing horizontal navigation for aircraft en-route, terminal, initial approach, non-precision approach (NPA) and departure operations. Required navigation performance (RNP) 0.1 is used as examples in this work to investigate H-ARAIM performance (RNP 0.1 is the most stringent navigation requirement for H-ARAIM operations). H-ARAIM may be considered an evolution of conventional RAIM that takes advantage of GNSS modernization and of newly deployed GNSS. According to the timeline, ARAIM is scheduled to first provide horizontal service (H-ARAIM) and then V-ARAIM.

With multiple GNSS constellations available for future ARAIM, the impact of having a large number of available measurements on navigation performance is not entirely obvious. From the integrity perspective, we can naturally expect the *conditional* integrity risk under any given fault hypothesis to be reduced. But there is a chance that the accumulation of monitored fault modes increases the *total* (i.e., unconditioned) integrity risk. This is especially concerning given, that new emerging constellations may not provide the same (low) levels of nominal ranging error and prior fault probabilities as GPS, especially in the early phases of their deployments [20]. From the continuity perspective, because any reasonable FD algorithm will detect most faults, the accumulated likelihood of satellite and constellation faults with multiple constellations could dramatically increase ARAIM continuity risk. Moreover, since LOC becomes a more serious safety event in ARAIM, other continuity risk contributions such as satellite outages also need to be quantified.

1.6 Dissertation Outline and Contributions

After this introductory chapter, Chapter 2 introduces ARAIM fundamentals. The navigation requirements for ARAIM operations are specified. The integrity support message (ISM) and the baseline user algorithm is described. In addition, the

parity space is introduced and the navigation performance of the baseline ARAIM FD function presented.

Chapters 3 to 7 respectively correspond to the five main contributions to knowledge in this dissertation. These contributions are outlined in the following subsections.

1.6.1 Establishing the Theoretical Basis to Quantify Continuity Risk.

Most prior ARAIM work focused on developing theoretical methods to reduce integrity risk, but only few investigated other navigation metrics. In particular, nearly all prior literature regards false alarm (FA) as the only concern for LOC, whereas there are actually many other sources that contribute to continuity risk. In response, V- and H-ARAIM continuity risks are now quantified by accounting for the impact of both fault occurrences and unscheduled satellite outages (USO). New methods are introduced to limit the impact of each source on navigation continuity. In addition, we interpret continuity requirements with respect to different operational scenarios, and identify the cases when an airborne fault exclusion function is required. It is shown that exclusion is not needed for dual-constellation V-ARAIM, while it is always needed to provide H-ARAIM services. (Chapter 3)

1.6.2 Develop Fault Exclusion Scheme and New Bound on the Associated Integrity Risk.

A solution separation based fault exclusion algorithm is designed and the practical implementation procedure is detailed. This algorithm can be executed efficiently in real-time with a low probability of wrong exclusion. The approach is motivated by a parity space representation of RAIM detection, and the key is to use the relative magnitudes of the parity vector projections for each failure mode. To ensure safety, a second-layer detection test is performed to verify that the satellite subset after exclusion is fault free. The associated FDE integrity risk depends on the details of the exclusion algorithm, since the design of the algorithm provides the

criteria that determine the satellites to exclude. In this work, the integrity risk equations are bounded step by step, by accounting for all the exclusion options. (Chapter 4)

1.6.3 Quantify Achievable Multi-Constellation ARAIM Performance. Only dual-constellation implementations have been applied in current ARAIM performance analysis, although we foresee four full constellations. As discussed in Section 1.5, the impact on ARAIM FDE availability with increased number of GNSS measurements is still unknown. Using the new methods derived in this thesis, the ARAIM navigation performance is comprehensively investigated over various numbers and qualities of constellations, and the results are presented in terms of specific ARAIM operation scenarios. (Chapter 5)

1.6.4 Investigate the Impact of Test Statistic Time Correlation on ARAIM Integrity and Continuity Risk. According to the current baseline ARAIM user algorithm, the integrity and continuity risk are evaluated based on one sample test, assuming the test statistic correlation time is large compared to the exposure interval. However, other relevant research on GBAS have found this assumption is not true. For the GBAS case, the actual FA probability over the interval is found to be much higher than the probability evaluated at one sample even if the test statistic correlation time is longer than the exposure interval. Therefore, this work investigates the impact of ARAIM test statistic time correlation on both integrity and continuity, by deriving new methods to rigorously evaluate the risks over the exposure time. Both the analytical and experimental results show that the actual FA probability is two orders of magnitude higher than previously thought. A feasible solution to reduce the false alarm probability is provided, without degrading the ARAIM navigation availability. (Chapter 6)

1.6.5 Design a ARAIM Offline Ground Monitor to Validate the Integrity

Support Message. One of the most significant new features of ARAIM is the ISM, which provides assertions on the GNSS signal-in-space (SIS) performance. This dissertation describes the design, analysis, and evaluation of the offline ground monitor, which aims at validating the ISM broadcast to the users. The proposed architecture utilizes a worldwide network of sparsely distributed reference stations, and parametric satellite orbital models to estimate the satellite position and clock. Two separate analyses, covariance analysis and model fidelity evaluation, are carried out to respectively quantify the impact of measurement errors and of residual model errors on the estimation. The results of those analyses indicate this ground monitor design is adequate for ARAIM ISM validation. (Chapter 7)

1.6.6 Conclusion. Finally, Chapter 8 provides conclusions and opportunities for future research.

CHAPTER 2

ARAIM FUNDAMENTALS

This chapter introduces the fundamental knowledge of ARAIM, including the navigation requirements for ARAIM operations, the ISM, the user algorithm, the parity space representation, and the navigation performance of the ARAIM FD function. The current ARAIM architecture was proposed by WG-C, and it had been evolving over time. In comparison with traditional RAIM, the most innovative designs in ARAIM are (a) employing the ISM to provide assertions on the constellation performance and (b) creating new user algorithm to accommodate the dramatically increased measurement redundancy using multiple GNSS constellations. As the most important outcome of prior work on ARAIM, the baseline FD algorithm has been well defined in [8, 21]. Even though the author has been involved in modifying and updating the algorithm, it is not regarded as a major contribution in this dissertation. Therefore, this chapter will take advantage of much of the relevant prior work, and provide detailed and comprehensive derivations of the ARAIM solution separation (SS) FD algorithm, from the fundamental GNSS measurement equation to the final integrity risk upper bound.

2.1 Navigation Requirements

The navigation requirements for ARAIM operations are specified by ICAO in [22], and they are interpreted in detail in this section. RNP 0.1 and LPV-200, which respectively correspond to the most stringent requirements for H- and V-ARAIM services, are employed as representatives throughout this thesis. If these two operations can be provided by ARAIM, the others can be achieved as well. The integrity and continuity risk requirements (I_{REQ} and C_{REQ}), which are the focus of this disserta-

tion, are listed in Table 2.1.

Table 2.1. Integrity and Continuity Requirements for ARAIM Operations

Operations	VAL	HAL	Integrity Risk Requirement	Time to Alert (TTA)	Continuity Risk Requirement
LPV-200	35 m	40 m	10^{-7} /approach	6 sec	8×10^{-6} /15sec
RNP 0.1	N/A	185 m (0.1 nm)	10^{-7} /hour	10 sec	10^{-8} /hour to 10^{-4} /hour

As shown in Table 2.1, there is no VAL requirement for H-ARAIM because it only provides horizontal navigation. In addition, the ALs of LPV-200 are significantly smaller than those of RNP 0.1, which reflects the fact that LPV-200 has the most stringent integrity requirement for ARAIM. V-ARAIM integrity requirement $I_{REQ,V}$ is specified on a per approach basis, for which the exposure time is 150 seconds [6]. However, when computing the probability of fault occurrence during an approach, one must properly account for the time that the ground segment needs to inform the user, i.e., mean time to alert (MTTA). For example, a 1-hour MTTA means that a latent fault can be existing before the approach and manifests at any time epoch while approaching. As for the H-ARAIM integrity risk requirement $I_{REQ,H}$, it is stated in [22] that $I_{REQ,H}$ for a single aircraft is 10^{-5} /hour. Nevertheless, since GNSS based navigation may simultaneously serve a large number of aircraft over a large area, a system integrity failure could cause a much more serious consequence. To account for the impact of multiple aircraft, as listed in Table 2.1, the value of 10^{-7} /hour is used for H-ARAIM $I_{REQ,H}$.

The TTA column in Table 2.1 specifies the maximum allowable time for the navigation system to notify the user after a hazardous event occurs. For example, the aircraft must be notified within 6 seconds if a hazardous fault is detected during

LPV-200 approach. It is noteworthy that the TTA requirements are for the airborne navigation systems, whereas the MTTA is the time that the GNSS control segment needs to detect the faults. MTTA is usually much larger than TTA, because there is no direct safety threat involved.

The continuity risk requirement $C_{REQ,V}$ for LPV-200 is 8×10^{-6} per 15 seconds, which is the same as the requirement for category I precision approach. According to ICAO, this requirement applies to average risk (over time) of LOC, and is normalized to a 15-second exposure time. Unlike LOI, which can lead to catastrophic consequences, V-ARAIM LOC only causes a missed approach, which is considered a normal operation because it does not lead to safety threats. An approach can always be aborted before the touch-down point so the significance of LOC during approach is far less than LOI. Nevertheless, the system still needs to be designed to ensure the average sense $C_{REQ,V}$ to limit the frequency of missed approaches, which if left unconstrained, would obviously lead to undesirable operational consequences both for aircraft users and air traffic controllers (ATC).

The occurrence of H-ARAIM LOC is regarded as a major failure condition when other navigation means are not available [16]. As shown in Table 2.1, H-ARAIM has more stringent continuity requirements. This is because LOC during a V-ARAIM operation leads the aircraft to abort the approach, go around, and try again. As just noted, such maneuvers are considered to be more-or-less normal occurrences and do not impact safety. In contrast, an H-ARAIM operation cannot be easily aborted once started, because alternate navigation means must be found when LOC occurs. Otherwise, pilots and ATC would face potentially dangerously stressful situations.

The H-ARAIM continuity risk requirement $C_{REQ,H}$ is specified per hour in a range from 10^{-8} /hour to 10^{-4} /hour. The existence of a range, rather than a single value, accounts for the impact on multiple aircraft. According to [22], the navigation

system continuity requirement for a single aircraft is 10^{-4} /hour. But this requirement is flexible for satellite-based systems, depending on the traffic density and airspace complexity. For example, the most stringent requirement 10^{-8} /hour is suitable for the area where many aircraft use the same service and additional navigation tools are not available. The intermediate value 10^{-6} /hour can be used for the situations of high air traffic density and airspace complexity, but the means to mitigate the LOC impact are present. The specifications for $C_{REQ,H}$ vary somewhat across aviation literatures. For example: [17] specifies that $C_{REQ,H}$ for en-route flight is 10^{-5} /hour and 10^{-6} /hour for lateral navigation only (LNAV) approach; [7] uses a different range for the continuity risk requirement from 10^{-7} /hour to 10^{-5} /hour. Therefore, the actual H-ARAIM $C_{REQ,H}$ applied to any particular aircraft may be variable, and is highly dependent on the operation. For simulation purposes later in this thesis, the value of $C_{REQ,H}$ will be selected to be generally consistent with most of these specifications. Since equipping with backup navigation tool is mandatory for civilian commercial aircraft, we choose $C_{REQ,H} = 10^{-6}$ /hour based on the ICAO specification. This value implies 100 aircraft are assumed to simultaneously use the same GNSS navigation service in the region of the operation [18], and possible mitigation means are available if a LOC occurs.

Table 2.2. V-ARAIM Accuracy and EMT Requirements

Accuracy	Fault-Free Accuracy	EMT
4 m (95%)	10 m (99.99999%)	15 m (99.999%)

In addition to the I_{REQ} and C_{REQ} , V-ARAIM also needs to meet the accuracy and effective monitor threshold (EMT) requirements. Those criteria are described in [8, 9] and listed here in Table 2.2. The first column refers to the typical accuracy criterion, which is specified in terms of 95% performance. The fault free (FF)

accuracy requirement indicates that the position estimate error should be less than 10 m over 99.99999% of the time under FF conditions. EMT is defined to reduce the occurrence of the vertical error being larger than 15 m, because such error will result in significantly increased workload for the flight crew. The EMT requirement in Table 2.2 limits the probability of such occurrence to be smaller than P_{EMT} , which is 10^{-5} .

2.2 Integrity Support Message

The performance of RAIM/ARAIM is measured either in terms of integrity risk or in terms of PL. It is highly dependent on the assumed GNSS nominal signal-in-space error models and on the a-priori fault probabilities. In current conventional RAIM implementations, this information is defined by the GPS CSP commitments, and is hardcoded in the receiver. As an evolution of RAIM, ARAIM will (a) additionally use constellations that are not as mature as GPS, and (b) seek to provide assured navigation for vertical guidance. To provide flexibility in the evolution of RAIM to multi-constellation ARAIM, and to minimize invasiveness into the avionics, ARAIM will include an ISM. The ISM will carry information defining SIS error and fault statistics, including nominal measurement biases b_{nom} , standard deviations of the ephemeris and clock errors σ_{URA} , prior probabilities of satellite faults P_{sat} , and prior probabilities of constellation-wide faults P_{const} [8]. The ISM parameters will be generated and validated at the ground, and updated to users as needed. Various methods of ISM dissemination are presently being considered, including on-aircraft databases and data broadcast through geosynchronous satellites or one or more of the GNSS core constellations. To validate the ISM, this dissertation describes an offline ground monitor design in Chapter 7, which is applicable regardless of the method of dissemination.

The ISM parameters b_{nom} and σ_{URA} specify a Gaussian bound on the SIS

performance under nominal conditions, (i.e., no faults). So the ephemeris and clock error model for integrity risk evaluation is bounded by the pair of normal distributions $N(\pm b_{nom}, \sigma_{URA})$. However, because continuity risk applies to average sense probability and its hazard classification is much lower than integrity, the error model applied for continuity should be representing the actual observed error distribution instead of a bounding one. Therefore, when evaluating the continuity risk, it will be assumed that the actual ephemeris/clock error is characterized by a zero-mean Gaussian distribution with a standard deviation of $\sigma_{URE} = 2/3\sigma_{URA}$.

As for the prior probabilities P_{sat} and P_{const} , current work on defining them is based on the GPS commitment and observations of historical data [28]. Since the other CSPs have not yet clearly established the fault descriptions for their constellations, this paper employs GPS as the representative. The GPS standard positioning service (SPS) performance standard (PS) commits to have less than three space vehicle (SV) faults per year with 1-hour MTTA by the ground segment [5]. This commitment corresponds to the satellite failure rate R_{sat} of 10^{-5} /hour/SV. Along with the MTTA value, it can be easily computed that the single satellite fault probability P_{sat} within one-hour interval is 10^{-5} [29]. Therefore, unless otherwise specified, 10^{-5} will be used for single SV fault mode in this thesis. As for constellation faults, even though it is expected that GPS CSP will commit a constellation fault prior probability P_{const} of 10^{-6} in future SPS PS, we stay consistent with current ARAIM fault assertions at this stage. Based on [28], a GPS P_{const} of 10^{-4} needs to be applied for V-ARAIM operations, and 10^{-8} can be used for H-ARAIM. For constellations other than GPS, P_{const} of 10^{-4} must be always assumed regardless of the operation. Note that these P_{sat} and P_{const} values are employed here just for demonstration purposes, and they may change in the future.

2.3 Measurement Model and Least-Squares Estimation

This dissertation focuses on the ‘snapshot’ ARAIM method, which uses carrier-smoothed code (CSC) measurements to estimate the user position and clock bias. Let n and m respectively be the numbers of GNSS measurements and states. That is, n is the number of all visible satellites and m is equal to three plus the number of constellations. In this work, it is assumed that there are always enough measurement redundancies to support ARAIM FDE. So the measurement equation can be linearized and expressed as [11, 23]:

$$\mathbf{z} = \mathbf{H}\mathbf{x} + \mathbf{v} + \mathbf{f} \quad (2.1)$$

where \mathbf{z} is the $n \times 1$ measurement vector, \mathbf{H} is the $n \times m$ observation matrix that is composed of line-of-sight vectors and ones, \mathbf{x} is the $m \times 1$ state vector, \mathbf{v} is the $n \times 1$ error vector, and \mathbf{f} is the $n \times 1$ fault vector, where the elements are zeros if their corresponding measurements are fault free.

The ARAIM error model has been well established and specified in [8, 21]. It accounts for three error sources including ephemeris/clock error, tropospheric delay, and the user error (receiver multipath and noise). The ionospheric delay is not considered here since ARAIM will always use dual-frequency GNSS measurements. However, an iono-free factor needs to be applied for the user error. Given the error model, \mathbf{v} can be bounded by a normal distribution $\mathbf{v} \sim N(\mathbf{b}, \mathbf{V})$, where \mathbf{V} is the covariance matrix of the measurement errors, and \mathbf{b} corresponds to the nominal bias vector with $\pm b_{nom}$ for each element.

As the most commonly used estimation method, the Least-squares (LS) estimator is used in the baseline ARAIM algorithm. Other proposed ARAIM ‘optimal’ estimation methods, which will be introduced in later sections, are developed based on the LS approach [25, 31]. Using a LS estimator, the states in equation 2.1 are estimated as:

$$\hat{\mathbf{x}}_0 = (\mathbf{H}^T \mathbf{V}^{-1} \mathbf{H})^{-1} \mathbf{H}^T \mathbf{V}^{-1} \mathbf{z} \quad (2.2)$$

and the corresponding covariance matrix of $\hat{\mathbf{x}}_0$ is:

$$\mathbf{P}_0 = (\mathbf{H}^T \mathbf{V}^{-1} \mathbf{H})^{-1} \quad (2.3)$$

In addition, to simplify the notations, a system matrix \mathbf{S}_0 is defined as:

$$\mathbf{S}_0 = (\mathbf{H}^T \mathbf{V}^{-1} \mathbf{H})^{-1} \mathbf{H}^T \mathbf{V}^{-1} \quad (2.4)$$

The subscript ‘0’ in equations 2.2 to 2.4 indicates the usage of the full set of satellites, i.e., all the available measurements are used to obtain the position solution. To extract the state of interest, a $1 \times m$ vector $\boldsymbol{\alpha}_r$ is defined, where the subscript ‘ r ’ notes the r^{th} element of \mathbf{x} . For example, $r = 3$ corresponds to extracting the vertical component of the position estimate. If GPS/Galileo constellations are employed,

$$\boldsymbol{\alpha}_3 = [0 \ 0 \ 1 \ 0 \ 0] \quad (2.5)$$

Accordingly, when using a local east-north-up coordinate system, we use the following notation to define the vertical position estimate, variance and system matrix:

$$\hat{x}_0^{(3)} = \boldsymbol{\alpha}_3 \hat{\mathbf{x}}_0, \sigma_0^{(3)^2} = \boldsymbol{\alpha}_3 \mathbf{P}_0 \boldsymbol{\alpha}_3^T, \text{ and } \mathbf{S}_0^{(3)} = \boldsymbol{\alpha}_3 \mathbf{S}_0 \quad (2.6)$$

Since same approach can be applied for any of the three dimensions, the derivations are written in terms of only one ($r = 1, 2, \text{ or } 3$) for the rest of the thesis. And to simplify notations, the subscript (r) is removed in the final expression. Therefore, the position estimation error of the state of interest ε_0 is written as:

$$\varepsilon_0 = \hat{x}_0 - x = \mathbf{S}_0^{(r)} (\mathbf{v} + \mathbf{f}) \quad (2.7)$$

$$\varepsilon_0 \sim N \left(\mathbf{S}_0^{(r)} (\mathbf{b} + \mathbf{f}), \sigma_0^2 \right) \quad (2.8)$$

2.4 Baseline Fault Detection User Algorithm

The user algorithm consists of two parts: FD implementation and the corresponding integrity risk (or PL) evaluation. This section starts with the definitions of P_{HMI} and P_{FA} , then describes the solution separation (SS) FD algorithm, and then provides a computationally efficient upper bound on the integrity risk.

2.4.1 Integrity Risk and False Alarm. The integrity risk P_{HMI} for ARAIM FD is the joint probability of undetected faults resulting in HMI:

$$P_{HMI} = P(HI_0, \bar{D}_0) \quad (2.9)$$

where HI_0 represents the event of hazardous information existing in the full-set solution, i.e., $|\varepsilon_0| > \ell$, where ℓ is the AL. \bar{D}_0 is the event of no fault detection using all satellites in view, i.e., $|q| < T$, where q is the detection test statistic and T is the threshold (to be defined in the next subsection).

Therefore, equation 2.9 can be written as:

$$P_{HMI} = P(|\varepsilon_0| > \ell, |q| < T) \quad (2.10)$$

ARAIM employs a multiple fault hypothesis approach to evaluate the integrity risk [24]. Equation 2.10 becomes:

$$P_{HMI} = \sum_{i=0}^H P(|\varepsilon_0| > \ell, |q| < T | H_i) P_{H_i} \quad (2.11)$$

where H_i denotes the fault hypotheses for $i = 1, 2, \dots, H$, which account for all faulty SV combinations of the measurements including FF (H_0), single satellite fault, multiple satellite faults, constellation fault. P_{H_i} is the prior probability of the corresponding fault mode H_i , which can be evaluated from P_{sat} and P_{const} . To avoid confusion, it is worth mentioning that the subscript ‘0’ on H_0 indicates the FF state, whereas the ‘0’ in equations 2.2 to 2.10 represent the use of all-in-view satellites (i.e., if the measurements are fault free all of them can be used).

For those hypotheses that account for multiple simultaneous faults, the prior probabilities are small in comparison with the integrity risk requirement. For example, the probability of having three simultaneous SV failures is 10^{-15} , which is negligible compared to I_{REQ} . In these cases, to improve computational efficiency, the associated conditional integrity risks can be upper bounded by 1. Therefore, equation 2.11 can be rewritten and bounded by:

$$P_{HMI} = \sum_{i=0}^h P(|\varepsilon_0| > \ell, |q| < T | H_i) P_{H_i} + \sum_{i=h+1}^H P(|\varepsilon_0| > \ell, |q| < T | H_i) P_{H_i} \quad (2.12a)$$

$$< \sum_{i=0}^h P(|\varepsilon_0| > \ell, |q| < T | H_i) P_{H_i} + \sum_{i=h+1}^H P_{H_i} \quad (2.12b)$$

where h is the number of fault modes that need to be monitored. The second summation term on the right side of 2.12b is defined as P_{NM} , which accounts for the events with small probabilities that are not monitored (NM). An integrity budget P_{THRES} is allocated to limit P_{NM} , and a detailed description of how to determine the monitored fault modes and compute the P_{NM} is provided in [8] and [11].

FA is one of the main causes for LOC, and it is usually limited by setting the detection threshold T appropriately. FA occurs when there is a deceptive alarm under FF condition:

$$P_{FA} = P(D_0 | H_0) P_{H_0} = P(|q| > T | H_0) P_{H_0} \quad (2.13)$$

where D_0 indicates the fault detection event using satellites in view.

2.4.2 Defining the Test Statistic. The SS RAIM detection method had been derived in [11], and it has been selected as the baseline algorithm by the ARAIM working group. The SS test statistics are defined in position domain, which are the differences between the full-set position solution \hat{x}_0 and the subset solutions \hat{x}_d :

$$\Delta_d = \hat{x}_0 - \hat{x}_d = \varepsilon_0 - \varepsilon_d, \text{ for } d = 1 \dots h. \quad (2.14)$$

where the subscript d indexes the number of detection test statistics from $1 \dots h$, and h equals to the number of monitored fault modes. \hat{x}_d is the position estimate using satellites without the one(s) in fault mode d . ε_d is the position estimate error of \hat{x}_d , i.e., $\varepsilon_d = \hat{x}_d - x$.

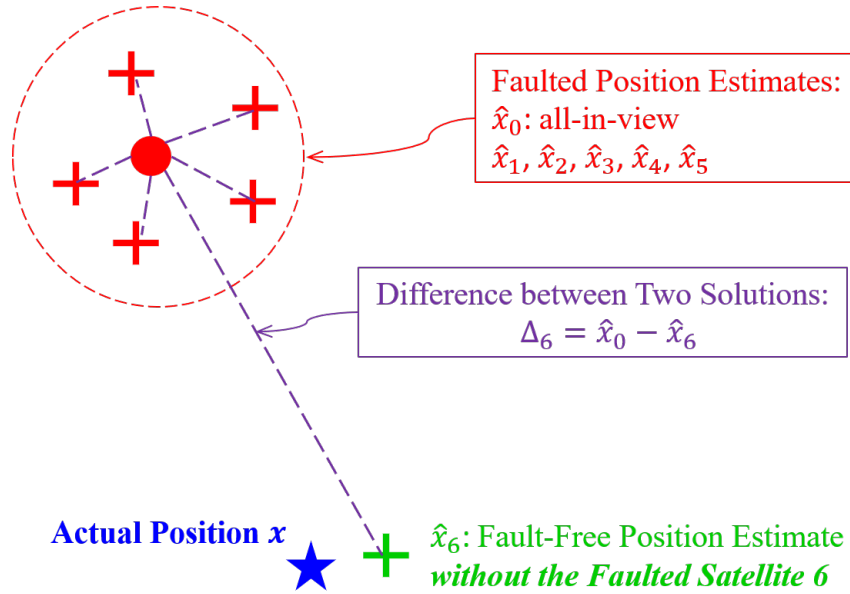


Figure 2.1. Interpretation of SS Test Statistics.

As the result, the h detection statistics Δ_d respectively correspond to each of the fault hypotheses H_i ($i = 1 \dots h$). If *any* of the statistics exceed the threshold, an alarm is issued, indicating fault exists in the system. Otherwise, if *all* the test statistics are smaller than their thresholds, there is no detection event and the operation continues. To further interpret the SS approach, Figure 2.1 illustrates an example case in the position domain: 6 SVs are employed for positioning; only a single satellite fault is considered; the measurement of SV 6 is faulted. Therefore, among the 7 position estimates, only \hat{x}_6 (denoted in green) provides a FF estimate, which is close to the actual position denoted by the blue star. All the faulted position estimates are circled by the dashed red line in Figure 2.1, where the solid red dot corresponds to the all-in-view position estimate and the others are the subset solutions. In this

figure, the SS test statistics are expressed by the purple dashed lines. Δ_6 is expected to be the maximum because it corresponds to the distance between a faulted and a FF estimate.

To compute the subset position estimate \hat{x}_d , let \mathbf{W} be defined as the inverse of the covariance matrix \mathbf{V} , i.e., $\mathbf{W} = \mathbf{V}^{-1}$, and let \mathbf{W}_d be defined as the inverse covariance matrix under hypothesis H_d , where \mathbf{W}_d is equal to \mathbf{W} except the elements associated with the faulted mode are set to be 0. For example, if H_d indicates the faults are on the 2nd and 4th measurements, then those two diagonal elements in \mathbf{W}_d are set to 0. Similar to the all-in-view case, the subset position solution \hat{x}_d and the estimation error ε_d can be expressed as:

$$\hat{x}_d = \mathbf{S}_d^{(r)} \mathbf{z}, \text{ and } \varepsilon_d = \mathbf{S}_d^{(r)} (\mathbf{v} + \mathbf{f}) = \mathbf{S}_d^{(r)} \mathbf{v} \quad (2.15)$$

where

$$\mathbf{S}_d^{(r)} = \boldsymbol{\alpha}_r (\mathbf{H}^T \mathbf{W}_d \mathbf{H})^{-1} \mathbf{H}^T \mathbf{W}_d \quad (2.16)$$

In equation 2.15, the faulted measurements are removed in $\mathbf{S}_d^{(r)}$. So, the faults have no impact on \hat{x}_d and ε_d , and the subset estimation error is distributed as following:

$$\varepsilon_d \sim N \left(\mathbf{S}_d^{(r)} \mathbf{b}, \sigma_d^2 \right) \quad (2.17)$$

where

$$\sigma_d^2 = \boldsymbol{\alpha}_r \mathbf{P}_d \boldsymbol{\alpha}_r^T, \text{ and } \mathbf{P}_d = (\mathbf{H}^T \mathbf{W}_d \mathbf{H})^{-1} \quad (2.18)$$

Plugging equations 2.15 and 2.7 into 2.14, Δ_d becomes:

$$\Delta_d = \mathbf{S}_{\Delta_d}^{(r)} (\mathbf{v} + \mathbf{f}) \sim N \left(\mathbf{S}_{\Delta_d}^{(r)} (\mathbf{b} + \mathbf{f}), \sigma_{\Delta_d}^2 \right) \quad (2.19)$$

where it is defined that $\mathbf{S}_{\Delta_d}^{(r)} = \mathbf{S}_0^{(r)} - \mathbf{S}_d^{(r)}$, and Appendix B of [11] has presented the proof that $\sigma_{\Delta_d}^2 = \sigma_d^2 - \sigma_0^2$.

2.4.3 Bounding P_{HMI} and P_{FA} . With the SS detection methodology being

clarified, the integrity risk equation 2.12 can be written in terms the test statistics:

$$P_{HMI} < \sum_{i=0}^h P \left(|\varepsilon_0| > \ell, \bigcap_{d=1}^h |\Delta_d| < T_{\Delta_d} | H_i \right) P_{H_i} + P_{NM} \quad (2.20)$$

and the false alarm equation 2.13 becomes:

$$P_{FA} = P \left(\bigcup_{d=1}^h |\Delta_d| > T_{\Delta_d} | H_0 \right) P_{H_0} \quad (2.21)$$

where the intersection \bigcap and union \bigcup signs restate the fact that \bar{D}_0 occurs only if all the test statistics are less than the thresholds, and detection D_0 occurs when any of the statistics exceed the thresholds.

Similar to most detection problems, the SS ARAIM detection thresholds are determined by limiting the FA probability. However, directly evaluating P_{FA} using equation 2.21 is cumbersome because the statistics are correlated [38]. Therefore, the following equation is usually used to bound P_{FA} :

$$P_{FA} < \sum_{d=1}^h P (|\Delta_d| > T_{\Delta_d} | H_0) P_{H_0} \quad (2.22)$$

As mentioned in section 2.2, a realistic SIS error model should be applied for continuity risk evaluation. Therefore, when computing T_{Δ_d} , the ephemeris/clock error is characterized by a zero mean normal distribution, i.e., $\mathbf{b} = \mathbf{0}$. In addition, because there is no fault ($\mathbf{f} = \mathbf{0}$) under the FF hypothesis H_0 , Δ_d in equation 2.22 has zero mean. Let $P_{FA,REQ}$ be the FA requirement allocated from C_{REQ} . To meet $P_{FA} < P_{FA,REQ}$, the detection thresholds can be computed as:

$$T_{\Delta_d} = T_d \sigma_{\Delta_d}, \text{ where } T_d = Q^{-1} \left\{ \frac{P_{FA,REQ}}{2P_{H_0} \cdot h} \right\} \quad (2.23)$$

and Q^{-1} is the inverse tail probability function.

The correlations among the test statistics also makes equation 2.20 challenging to be directly evaluated. Instead, a conservative but computationally efficient upper

bound is usually considered to compute the integrity risk. To do this, the monitored hypotheses are divided into two groups: the FF hypothesis H_0 and all the other H_i for $i = 1, 2, \dots, h$. First, let P_{HMI, H_0} be defined as the conditional integrity risk under hypothesis H_0 . It is bounded by ignoring the no detection event:

$$P_{HMI, H_0} = P \left(|\varepsilon_0| > \ell, \bigcap_{d=1}^h |\Delta_d| < T_{\Delta_d} \mid H_0 \right) \quad (2.24a)$$

$$< P (|\varepsilon_0| > \ell \mid H_0) \quad (2.24b)$$

Equation 2.24b is a tight bound because the probability of having no detection event under H_0 is close to one. In addition, the order of magnitude of this bound is usually much smaller than I_{REQ} because σ_0 is small comparing to the AL. Therefore, the integrity risk increment caused by this term is typically negligible.

Let P_{HMI, H_i} be the conditional integrity risk of other monitored fault modes where $i \neq 0$. It can be bounded by:

$$P_{HMI, H_i} = P \left(|\varepsilon_0| > \ell, \bigcap_{d=1}^h |\Delta_d| < T_{\Delta_d} \mid H_i \right) \quad (2.25a)$$

$$< P (|\varepsilon_0| > \ell, |\Delta_i| < T_{\Delta_i} \mid H_i) \quad (2.25b)$$

In equation 2.25b, only the test statistic of fault mode i is used to examine the detection event. This step is also considered a tight bound because the position differences between full-set and fault-free solution is expected to be the maximum. The upper bound of equation 2.25b is a joint probability; however, [11] has proved ε_0 and Δ_i are independent. One way to evaluate 2.25b is by searching over all the fault magnitudes and directions to find the maximum integrity risk, but this approach is computationally expensive because it requires deriving the worst case fault. In response, a further bound of equation 2.25b is developed. From equation 2.14, it can be derived that:

$$|\varepsilon_0| \leq |\varepsilon_i| + |\Delta_i| \quad (2.26)$$

Applying equation 2.26 into 2.25b, the bound becomes:

$$P_{HMI,H_i} < P(|\varepsilon_i| + |\Delta_i| > \ell, -|\Delta_i| > -T_{\Delta_i} | H_i) \quad (2.27a)$$

$$< P(|\varepsilon_i| + T_{\Delta_i} > \ell | H_i) \quad (2.27b)$$

Equation 2.27b is obtained by summing the two joint variables in 2.27a. Therefore, the final expression of the overall integrity risk bound is:

$$P_{HMI} < P(|\varepsilon_0| > \ell | H_0) P_{H_0} + \sum_{i=1}^h P(|\varepsilon_i| + T_{\Delta_i} > \ell | H_i) P_{H_i} + P_{NM} \quad (2.28)$$

The most remarkable advantage of equation 2.28 is that all the estimation errors FF, and their distributions have been characterized by equations 2.17 and 2.18. Moreover, to conservatively account for the impact of nominal biases on integrity risk, the mean of ε_i is bounded by [8]:

$$b_i = \sum_{idx=1}^n |S_{i,idx}^{(r)}| b_{nom} \geq \mathbf{S}_i^{(r)} \mathbf{b} \quad (2.29)$$

where idx denotes the measurement index. $S_{i,idx}^{(r)}$ represents each element in the $1 \times n$ vector $\mathbf{S}_i^{(r)}$.

Other than directly evaluating the integrity risk, the PL is an alternative way to express the information contained in the integrity risk bound. The PL is a more practical metric in many cases, especially when the ALs of the operations are unknown to the GNSS receiver. The PL corresponding to equation 2.28 can be computed (iteratively) using equation 2.30. The derivation of equation 2.30 can be found in Appendix D of [39], and a method to solve the equation is introduced in Appendix E of the same document.

$$I_{REQ} < 2Q\left(\frac{PL - b_0}{\sigma_0}\right) + \sum_{i=1}^h Q\left(\frac{PL - T_{\Delta_i} - b_i}{\sigma_i}\right) P_{H_i} + P_{NM} \quad (2.30)$$

2.4.4 V-ARAIM Accuracy and EMT. For V-ARAIM operations, the accuracy and EMT tests should also be implemented. The standard deviation of the vertical

position solution for the accuracy criteria can be evaluated by the following:

$$\sigma_{v,acc} = \sqrt{\boldsymbol{\alpha}_3 \mathbf{S}_0 \mathbf{V}_{acc} \mathbf{S}_0^T \boldsymbol{\alpha}_3^T} \quad (2.31)$$

where \mathbf{V}_{acc} is the covariance matrix of the measurement errors used for accuracy and continuity evaluation, i.e., the SIS error component in \mathbf{V}_{acc} is σ_{URE}^2 .

Let K_{ACC} and K_{FF} respectively be the multipliers to compute the 95% and FF accuracies, the accuracy performance is:

$$95\% \text{ accuracy} = K_{ACC} \sigma_{v,acc} \quad (2.32a)$$

$$\text{FF accuracy} = K_{FF} \sigma_{v,acc} \quad (2.32b)$$

The values of K_{ACC} and K_{FF} can be easily computed from a standard normal distribution: $K_{ACC} = 1.96$ and $K_{FF} = 5.33$ [8]. However, because $10 \text{ m}/K_{FF}$ is smaller than $4 \text{ m}/K_{ACC}$, only the FF accuracy criterion needs to be considered.

The EMT is defined as the maximum vertical detection threshold of the fault modes whose prior probabilities are larger than P_{EMT} . Therefore:

$$EMT = \max_{i|P_{H_i} \geq P_{EMT}} T_{\Delta_i}^{(3)} \quad (2.33)$$

2.4.5 V-ARAIM Optimal Estimator. Among the metrics that measures the V-ARAIM performance, VAL is the most stringent requirement, whereas the others can usually be achieved easily. To improve the overall navigation performance, an optimal estimator had been designed for V-ARAIM. The principle of it is to reduce the vertical component of the integrity risk (or VPL) at the cost of degrading the accuracy performance [25, 31]. Therefore, it will only be applied when $VPL > VAL$, while the FF accuracy meets the requirement. Letting $\sigma_{v,acc,req}$ be the requirement of $\sigma_{v,acc}$, the estimator that minimizes VPL can be obtained using the following steps [21]:

1. Among all the monitored fault hypotheses H_i , find the one with maximum standard deviation of the subset estimate error σ_i , and note the corresponding system matrix as \mathbf{S}_{imax} .

2. Compute:

$$\begin{aligned} a &= \left(\mathbf{S}_{imax}^{(3)} - \mathbf{S}_0^{(3)} \right)^T \mathbf{V}_{acc} \left(\mathbf{S}_{imax}^{(3)} - \mathbf{S}_0^{(3)} \right) \\ b &= 2\mathbf{S}_0^{(3)T} \mathbf{V}_{acc} \left(\mathbf{S}_{imax}^{(3)} - \mathbf{S}_0^{(3)} \right) \\ c &= \mathbf{S}_0^{(3)T} \mathbf{V}_{acc} \mathbf{S}_0^{(3)} - \sigma_{v,acc,req}^2 \end{aligned} \quad (2.34)$$

3. Compute:

$$t = \min \left(1, \frac{-b + \sqrt{b^2 - 4ac}}{2a} \right) \quad (2.35)$$

4. Compute:

$$\mathbf{s}_{opt} = \mathbf{S}_0^{(3)} + t \left(\mathbf{S}_{imax}^{(3)} - \mathbf{S}_0^{(3)} \right) \quad (2.36)$$

5. Replace $\mathbf{S}_0^{(3)}$ with \mathbf{s}_{opt} , and define the new all-in-view system matrix as $\mathbf{S}_{0,opt}$.
Reevaluate the full-set position estimate, P_{HMI}/VPL , and $\sigma_{v,acc}$ using $\mathbf{S}_{0,opt}$.

2.5 Parity Space

The parity space representation is the most illustrative expression of the detection process using measurement redundancy. It had been introduced for residual based (RB) RAIM in [40]. In this section, the definition of parity vector is described, the relationship between the parity vector and SS test statistics is established, and a simple measurement model is introduced to visualize the relationship in parity space.

2.5.1 Parity Vector. To get the parity vector, the measurement equation 2.1 is first normalized by pre-multiplying by $\mathbf{V}^{-\frac{1}{2}}$. Then the normalized measurement vector, observation matrix, noise vector and fault vector respectively become: $\mathbf{z}^* = \mathbf{V}^{-\frac{1}{2}}\mathbf{z}$, $\mathbf{H}^* = \mathbf{V}^{-\frac{1}{2}}\mathbf{H}$, $\mathbf{v}^* = \mathbf{V}^{-\frac{1}{2}}\mathbf{v}$ and $\mathbf{f}^* = \mathbf{V}^{-\frac{1}{2}}\mathbf{f}$. The $(n - m) \times n$ parity matrix \mathbf{Q} is

obtained by taking the singular value decomposition (SVD) of \mathbf{H}^* . Let the following equation 2.37 be the SVD result:

$$\mathbf{H}_{n \times m}^* = \mathbf{U}_{n \times n} \begin{bmatrix} \mathbf{S}_{m \times m} \\ \mathbf{0}_{(n-m) \times m} \end{bmatrix} \mathbf{V}_{m \times m}^T, \text{ where } \mathbf{U}_{n \times n} = \begin{bmatrix} \mathbf{U}_{1, n \times m} & \mathbf{U}_{2, n \times (n-m)} \end{bmatrix} \quad (2.37)$$

Defining \mathbf{U}_2^T as the parity matrix \mathbf{Q} , then the $(n-m) \times 1$ parity vector \mathbf{p} is [40, 41]:

$$\mathbf{p} = \mathbf{Q}\mathbf{z}^* = \mathbf{Q}(\mathbf{v}^* + \mathbf{f}^*) \quad (2.38)$$

Moreover, [11] has proved the following relationships:

$$\mathbf{Q}\mathbf{H}^* = \mathbf{0}_{(n-m) \times m}, \quad \mathbf{Q}\mathbf{Q}^T = \mathbf{I}_{(n-m)}, \text{ and } \mathbf{Q}^T\mathbf{Q} = \mathbf{I}_n - \mathbf{H}^*\mathbf{S}_0^* \quad (2.39)$$

where $\mathbf{S}_0^*\mathbf{V}^{-\frac{1}{2}} = \mathbf{S}_0$, and \mathbf{I}_n is identical matrix.

2.5.2 SS Test Statistics in Parity Space. To establish the relationships between SS test statistics and the parity vector, the statistics are first normalized by their standard deviations. For fault hypothesis H_i , the normalized statistic is:

$$q_i = \frac{\Delta_i}{\sigma_{\Delta_i}} = \frac{\boldsymbol{\alpha}_r (\mathbf{S}_0^* - \mathbf{S}_i^*) \mathbf{z}^*}{\sigma_{\Delta_i}} \quad (2.40)$$

In equation 2.40, \mathbf{S}_i^* is the system matrix of the normalized measurement equation for hypothesis H_i . Combining equation 2.39 with the relationship shown in [11] that $\mathbf{S}_0^* = \mathbf{S}_i^*\mathbf{H}^*\mathbf{S}_0^*$, Δ_i can be expressed as:

$$\begin{aligned} \Delta_i &= \boldsymbol{\alpha}_r (\mathbf{S}_i^*\mathbf{H}^*\mathbf{S}_0^* - \mathbf{S}_i^*) \mathbf{z}^* \\ &= -\boldsymbol{\alpha}_r \mathbf{S}_i^* \mathbf{Q}^T \mathbf{Q} \mathbf{z}^* = -\boldsymbol{\alpha}_r \mathbf{S}_i^* \mathbf{Q}^T \mathbf{p} \end{aligned} \quad (2.41)$$

The standard deviation of the test statistic σ_{Δ_i} is equivalent to:

$$\begin{aligned} \sigma_{\Delta_i} &= \sqrt{\boldsymbol{\alpha}_r (\mathbf{P}_i - \mathbf{P}_0) \boldsymbol{\alpha}_r^T} \\ &= \sqrt{\boldsymbol{\alpha}_r (\mathbf{S}_i^* \mathbf{S}_i^{*T} - \mathbf{S}_i^* \mathbf{H}^* \mathbf{S}_0^{*T} \mathbf{S}_i^{*T}) \boldsymbol{\alpha}_r^T} \\ &= \sqrt{\boldsymbol{\alpha}_r \mathbf{S}_i^* \mathbf{Q}^T \mathbf{Q} \mathbf{S}_i^{*T} \boldsymbol{\alpha}_r^T} \end{aligned} \quad (2.42)$$

Therefore, the relationship between q_i and \mathbf{p} can be expressed as:

$$q_i = \mathbf{w}_i \mathbf{p}, \text{ where } \mathbf{w}_i = \frac{-\alpha_r \mathbf{S}_i^* \mathbf{Q}^T}{\sqrt{\alpha_r \mathbf{S}_i^* \mathbf{Q}^T (\alpha_r \mathbf{S}_i^* \mathbf{Q}^T)^T}} \quad (2.43)$$

\mathbf{w}_i in equation 2.43 is defined as “fault projection line” for the hypothesis H_i . And the projection of the parity vector on this line is the corresponding normalized SS test statistic q_i . It should be noted that the derivation of \mathbf{w}_i applies for all the fault hypotheses. For single fault mode, \mathbf{w}_i is also called fault mode line [11], where the mean of the parity vector is on this line.

2.5.3 Detection Region in Parity Space. To visualize fault detection in parity space, a simple measurement model is employed. The observation matrix and the error model are:

$$\mathbf{H} = [1 \ 1 \ 1]^T, \text{ and } \mathbf{v} \sim N(\mathbf{0}_{(3 \times 1)}, \mathbf{I}_3) \quad (2.44)$$

Three fault modes $i = 1, 2, 3$, corresponding to each measurement, are considered in this problem. Since there are two redundant measurements, this example can be easily demonstrated in a two-dimensional parity space.

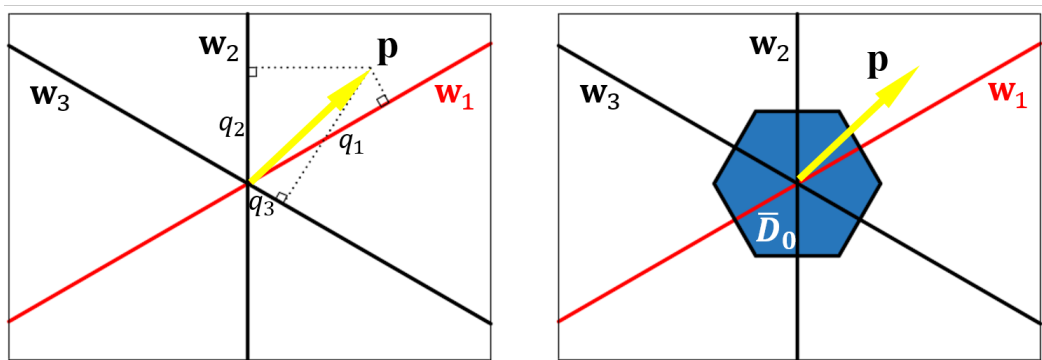


Figure 2.2. Parity Space Representation of ARAIM Fault Detection.

Figure 2.2 visualizes ARAIM FD process under the fault hypothesis H_1 , i.e., the fault is on the line \mathbf{w}_1 (highlighted red). The yellow arrow represents the parity

vector \mathbf{p} , and its projections onto three fault lines are the associated normalized SS test statistics, i.e., equation 2.43. The blue region on the right indicates no detection event \bar{D}_0 , in which all the statistics are less than the thresholds. It has regular hexagon shape because the magnitudes of the thresholds are equal for all three q_i . In this example case, the parity vector lies outside of the no detection region, so there is a detection event.

2.6 Navigation Performance of ARAIM Detection Function

Because the ARAIM WG-C was established on a bilateral basis between the EU and U.S., it was assumed that only GPS and Galileo constellations will be available to support ARAIM. As a result, the baseline fault detection user algorithm aims at providing full service capability without any reliance on other constellations except the GPS/Galileo. Therefore, this section demonstrates the navigation performance only using dual-constellation ARAIM. Multi-constellation ARAIM performance will be analyzed later in Chapter 5.

In the case of using GPS and Galileo constellations, the baseline simulation conditions have been clearly defined in [21]. Table 2.3 lists the key simulation parameters used for this analysis, which are modified from [21]. The almanac files are downloaded from the link in [21] to provide coarse SV positions, which are sufficient for covariance analysis.

2.6.1 V-ARAIM FD Availability Performance. The V-ARAIM navigation performance is demonstrated in terms of availability. Availability is defined as the fraction of time the navigation system is usable before the operation is initiated. Therefore, all the criteria in Tables 2.1 and 2.2 need to be achieved if the operation is available at a given time.

Figure 2.3 shows the worldwide availability of the LPV-200 operation. The

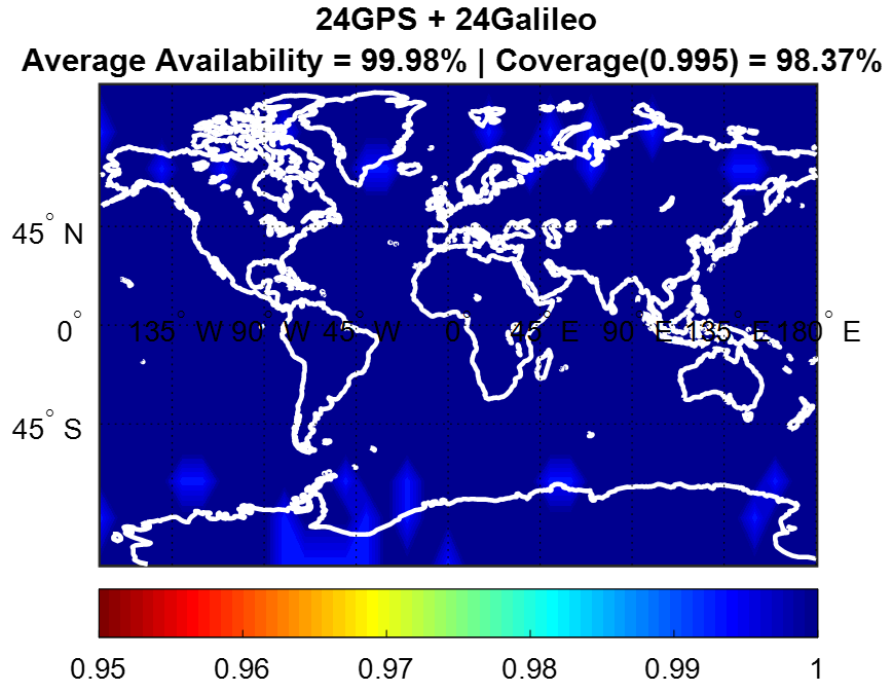


Figure 2.3. Baseline V-ARAIM FD Worldwide Availability Performance.

baseline user algorithm and optimal estimator described in Section 2.4 are employed to obtain this result. Coverage reflects the fraction of users in the investigated region that have availability greater than 0.995. When computing the average availability and coverage of Figure 2.3, user grid points are weighted by the cosine of the latitude to account for the relative area they represent. This result indicates that the dual-constellation V-ARAIM FD function is able to provide high service availability for LPV-200.

2.6.2 Worldwide HPL Map of H-ARAIM FD. The navigation performance of H-ARAIM FD is characterized in terms of HPL, and the worldwide HPL map is shown in Figure 2.4. The HPL values at each location are the maximum ones over the simulation time period. The figure shows that the HPL is significantly smaller than the HAL for RNP 0.1 over the entire Earth, which implies the availability and coverage of H-ARAIM are both 1.

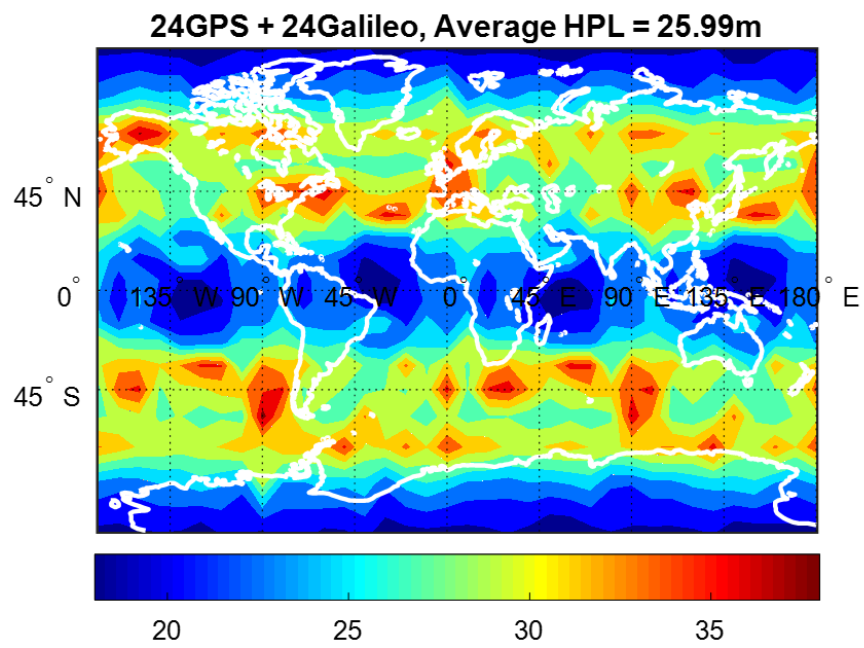


Figure 2.4. Baseline H-ARAIM FD Worldwide HPL Map.

Table 2.3. Baseline Simulation Conditions of Dual-Constellation ARAIM

Scenarios	Values
Constellation Configuration	24 GPS + 24 Galileo
Error Model	Nominal Model Described in [21]
Mask Angle	5 degrees
User Grid	Latitude by Longitude: : 10 deg \times 10 deg
Simulation Time Period	1 day
Time Steps	10 minutes
P_{sat}	10^{-5}
P_{const}	V-ARAIM: 10^{-4} for all constellations H-ARAIM: 10^{-8} for GPS, 10^{-4} for Galileo
σ_{URA}	V-ARAIM: 1 m, H-ARAIM: 2.4 m
σ_{URE}	$2/3\sigma_{URA}$
b_{nom}	0.75 m
Coverage Range	V-ARAIM: -70 deg to 70 deg latitude H-ARAIM: worldwide

CHAPTER 3

QUANTIFYING CONTINUITY RISK

As the first contribution of this dissertation, this chapter provides the theoretical basis to quantify the contributions of all sources to ARAIM continuity risk. In particular, since ARAIM will use multiple constellations, the heightened likelihood of the user encountering a fault or USO could significantly impact navigation continuity [34]. In response, a rigorous continuity risk equation is derived to quantitatively account for the LOC contributions of measurement faults and USO, based on the navigation requirements. The relationships among the failure rate, USO probability, MTTA, and the exposure time are captured. To reduce the LOC probability due to frequent FD events, a fault exclusion function can be implemented [36, 35]. However, the gain in continuity comes at the cost of increased integrity risk [24]. This is due to the fact that excluding satellites may weaken the satellite geometry, and the possibility of excluding the wrong satellite increases the integrity risk [33]. Therefore, exclusion introduces a tradeoff between integrity and continuity. Whether the exclusion function is even needed or not depends on the intended operations. Using the overall LOC equation, the need for airborne exclusion is assessed in this chapter, and the process to establish the requirements for exclusion function itself is described. In addition, the new approach developed in section 3.5 enables us to rigorously account for all the possible USO conditions, including multi-satellite outages, and to determine whether an exclusion function is still needed after a USO event. To achieve this, the assumptions are laid out and the rationale is clarified.

3.1 Causes of Loss of Continuity

Obviously, to properly evaluate the overall continuity risk, or probability of

LOC (P_{LOC}), all the sources that cause LOC must be properly accounted for. However, because ARAIM continuity has been paid less attention than integrity in the literature, FA is the only LOC source that has been considered so far [32, 42]. In reality, there are many other possible causes of LOC, including FD, USO, ionospheric scintillation (IOSC), and radio frequency interference (RFI). Among those sources, this work focuses on the impact of measurement fault and USO, because they can severely affect continuity in multi-constellation ARAIM. All other LOC sources are grouped together as P_{other} . Therefore, the overall P_{LOC} can be classified into two categories:

$$P_{LOC} = P_{alert} + P_{other} \quad (3.1)$$

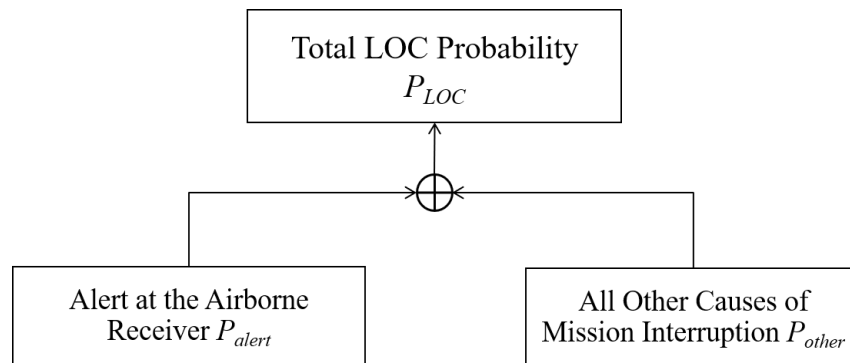


Figure 3.1. Two Categories of the LOC Sources.

In equation 3.1 and Table 3.1, P_{alert} is the probability of the airborne receiver issuing an alert. It indicates a true fault detection event under a faulted condition, or a FA event if the state is FF. Moreover, as will be addressed in later sections, the alert may also be issued under a USO condition. In this chapter, P_{alert} is first expanded to account for the measurement faults, and then even further to include the impact of USO events. As for the P_{other} , a continuity budget will be assigned for it, and this dissertation assumes that P_{other} is always below the budget.

3.2 Continuity Risk Contribution of Fault Occurrence

This section addresses the impact of GNSS faults on ARAIM continuity, and develops the basis to quantify their contribution. Because the impact of USO will be separately addressed later, the derivations in this section are based on the assumption that there is no USO, i.e., outage free (OF) conditions exist. So, FA and FD are considered as the main continuity threats here.

3.2.1 H-ARAIM Continuity Risk. Equation 3.2 shows the overall H-ARAIM continuity risk $P_{LOC,H}$ when only a detection function is implemented (i.e., without exclusion capability), where the subscript ‘H’ refers to H-ARAIM. The probability of FA and FD are respectively expressed as $P_{FA,H}$ and $P_{FD,H}$.

$$\begin{aligned} P_{LOC,H} &= P_{alert,H} + P_{other,H} \\ &= P_{FA,H} + P_{FD,H} + P_{other,H} \end{aligned} \quad (3.2)$$

where

$$P_{FA,H} = P(D_0|H_0) P_{H_0}, \text{ and } P_{FD,H} = \sum_{i=1}^H P(D_0|H_i) P_{H_i} \quad (3.3)$$

3.2.2 V-ARAIM Continuity Risk. Similar to equation 3.2, the total V-ARAIM continuity risk $P_{LOC,V}$ with only detection function, is expressed as equation 3.4.

$$\begin{aligned} P_{LOC,V} &= P_{alert,V} + P_{other,V} \\ &= m(P_{FA,V} + P_{FD,V}) + P_{other,V} \end{aligned} \quad (3.4)$$

For V-ARAIM operations, $C_{REQ,V}$ represents the allocation between one single aircraft and the non-aircraft elements, and each aircraft is considered independent. However, [22] also points out the requirement needs to be adjusted when two runways are closely-spaced. This is because navigation service can be used by many aircraft at the same time, and they may simultaneously loss continuity due to common system failure. However, a missed approach of an aircraft at one airport does not impact the ATC at other airports. Only if two runways are close with each other, the simultaneous missed approaches will result in increased stress for the same ATC. Therefore,

to be rigorous and conservative, the multiplier m is introduced in equation 3.4 to address the impact of navigation interruptions on more than one aircraft approach, and $m = 2$ is assumed in this thesis. It is worth clarifying for the use of m on FA event, which is typically caused by large error under FF condition. According to ARAIM error model, ephemeris and SV clock errors are the largest error sources, and their anomaly will have the same impact on two adjacent users, thereby causing simultaneous FA. Those scenarios have been conservatively captured in equation 3.4, which bounds the overall V-ARAIM continuity risk.

$$P_{FA,V} = P(D_0|H_0) \lambda P_{H_0}, \text{ and } P_{FD,V} = \sum_{i=1}^H \gamma P(D_0|H_i) \lambda P_{H_i} \quad (3.5)$$

where $\lambda = \frac{15 \text{ sec}}{1 \text{ hour}}$.

To accommodate the requirement $C_{REQ,V}$, the fault probabilities P_{H_i} need to be scaled to a 15-second exposure interval [37]. Unlike integrity risk, which is affected by latent faults, LOC occurs only at the transition moment from continuous service to sudden interruption. Let us conservatively assume all the faults can be detected and detection always occurs during approach. Even though a fault may last an hour or more before it is identified by the ground segment, if it does not impact the aircraft anymore once detected, so one fault will cause only one LOC in one 15 second segment regardless of when the fault is detected. Therefore, the multiplier in equation 3.5 is applied to convert the fault probability P_{H_i} into the 15-second interval.

In the justification of the last paragraph, it is implicitly assumed that a fault does not cause more than one missed approach for the same aircraft. However, despite the small likelihood, this situation may happen when (a) the aircraft is exposed to a long lasting fault, (b) a second approach is attempted following a missed approach due to FD, and (c) the fault is not detected again prior to the second approach but is detected again during the second approach. In response, another multiplier γ is

introduced in equation 3.5 to account for such scenario. On the one hand, since fault detection could occur multiple times during the 1-hour exposure period, γ should be larger than 1. On the other hand, if a fault is detected during the first attempted approach, it will most likely be detected again by the airborne algorithm prior to next approach (because the magnitude of GNSS ranging faults typically increases monotonically). Detection prior to an approach impacts availability, not continuity. Therefore, γ should be a small value which only accounts for the less likely, non-monotonically increasing faults. $\gamma = 1.1$ is employed in this thesis, which means that one tenth of aircraft are assumed to be exposed to the same fault again during their second approach.

3.3 Need for Exclusion Function

The motivation of designing an exclusion function is to mitigate the impact of fault occurrence on ARAIM continuity, so the need of this function, can be determined using the relationships established in section 3.2, based on the continuity requirements interpreted in section 2.1. When the probability of FD exceeds the continuity risk requirement, airborne exclusion should be implemented. In this section, the need of exclusion will be comprehensively assessed for both V- and H-ARAIM over multiple criteria, and the cases when an exclusion function is required are identified.

For H-ARAIM, the need of an exclusion function can be assessed by comparing the $P_{FD,H}$ in equation 3.2 with the $C_{REQ,H}$. Given the significance of H-ARAIM LOC event and the stringent value of $C_{REQ,H}$, the conclusion appears obvious. Even the single satellite fault rate for GPS ($10^{-5}/\text{hr}$) already dramatically exceeds requirement. Therefore, H-ARAIM exclusion function must be implemented to improve continuity.

For V-ARAIM, to respectively limit each LOC contribution, the overall continuity risk requirement $C_{REQ,V}$ is allocated to the different sources. Table 3.1 lists

an example allocation that will be used throughout the remainder of this thesis. The three components in the first row correspond to LOC event under the FF condition, the fault-present (FP) condition and all other causes. The values in the second row are the allocated budgets whose summation is $C_{REQ,V}$. If the LOC probabilities under each individual condition are all smaller than these budgets, the overall continuity requirement is satisfied.

Table 3.1. V-ARAIM Continuity Budget Allocation

$P_{FF,V,REQ}$	$P_{FP,V,REQ}$	$P_{other,V,REQ}$
$2 \times 10^{-6}/15 \text{ sec}$	$5 \times 10^{-6}/15 \text{ sec}$	$10^{-6}/15 \text{ sec}$

As mentioned in section 2.4, the ARAIM FA probability can be controlled by setting the detection threshold to meet $P_{FF,V,REQ}$. To examine the need of a V-ARAIM exclusion function, the FD probability under the FP condition should be computed. To do this, we use the first two terms in equation 3.6 below, The rightmost term in equation 3.6 is a tight bound on this probability, because the likelihood of detecting a fault under H_i will be very close to 1 by design. If it turns out that the bound is smaller than $P_{FP,V,REQ}$, then a V-ARAIM exclusion function is not required for continuity.

$$mP_{FD,V} = m \sum_{i=1}^H \gamma P(D_0|H_i) \lambda P_{Hi} < m\gamma \sum_{i=1}^H \lambda P_{Hi} \quad (3.6)$$

As revealed by equation 3.6, the value of the bound is most directly influenced by the fault mode prior probabilities and the total number of fault modes, H . The latter, in turn, is depends on the number of constellations and satellites used. Whether an V-ARAIM exclusion function is needed or not could vary over different operational scenarios. We investigate multiple representative cases using two, three, and four constellations, for which $m = 2$ and $\gamma = 1.1$ are applied. The sensitivity analyses are

achieved by varying the number of measurements and the values of P_{sat} and P_{const} .

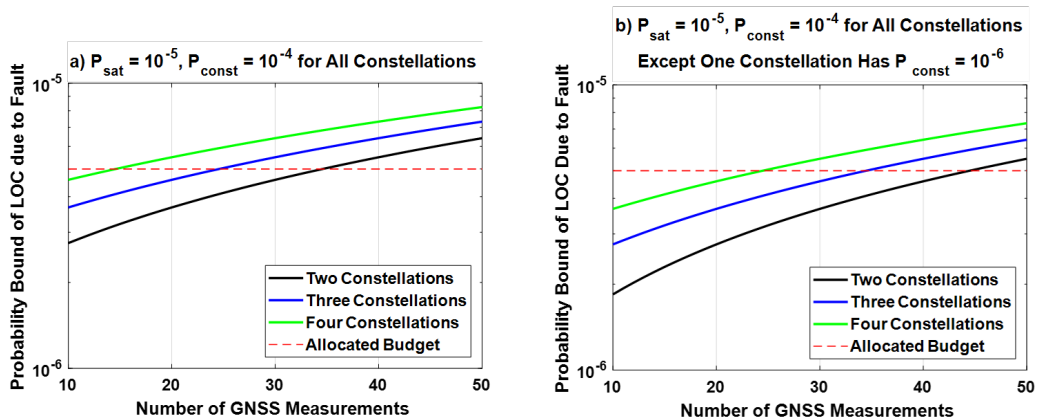


Figure 3.2. Probability Bound of LOC due to Fault with Varying Numbers of Measurements.

Figure 3.2 illustrates the probability bound of equation 3.6 as a function of the average number of visible satellites. In each figure, three solid lines distinguished by color correspond to number of constellations being investigated, and the red dashed line is the allocated continuity budget $P_{FP,V,REQ}$. An exclusion function is not required for the cases when the solid lines are below the red lines. The only difference between the Figures 3.2a and 3.2b is the assumption on fault probability, where Fig. 3.2a applies nominal P_{sat} and P_{const} for all constellations, and Fig. 3.2b assumes one of the investigated constellations is subject to a smaller P_{const} of 10^{-6} . Under dual-constellation scenario in Fig. 3.2a, the intersection between the black line and the threshold occurs when the average number of satellites is more than 35. It is highly unlikely that this number will ever be reached with any two constellations, which implies airborne exclusion function is not needed using dual-constellation V-ARAIM. For the four-constellation scenario in Fig. 3.2a, the green line is above the threshold if the average number of SVs exceeds 15. In this case, with four constellations, it is quite likely that the average number of visible satellites will exceed 15 visible SVs using four constellations, so the heightened continuity risk will need to be reduced by an exclusion function. When three constellations are applied, the intersection in Fig.

3.2a occurs 25 visible SVs. Therefore, at any given location, the need for exclusion with three constellations will depend on the actual average number of satellites visible at that location. In comparison with Fig. 3.2a, all the lines are moved to the right in Fig. 3.2b, which implies more SVs can be accommodated while still meeting the continuity budget. To further investigate the sensitivity on fault probability values, a more dedicated analysis is carried out.

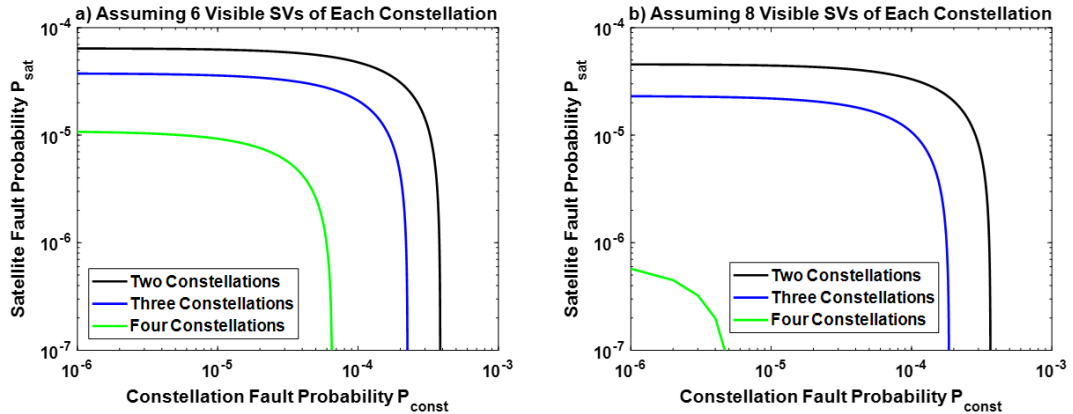


Figure 3.3. P_{sat} vs. P_{const} for One Constellation to Meet the Allocated Continuity Requirement.

Figure 3.3 shows the tolerable P_{sat} and P_{const} values for one constellation to meet the allocated continuity budget, while assuming all other constellations are subject to nominal fault probabilities, i.e., $P_{sat} = 10^{-5}$ and $P_{const} = 10^{-4}$. The three lines in each figure define the borders of whether or not implementing exclusion function is required. In other words, an exclusion function is not needed if the values of P_{sat} and P_{const} are located in the region under and to the left of the solid lines. Comparing those lines, the green one forms the smallest area because of the large number of measurements with four constellations. The difference between figures 3.3a and 3.3b is the assumed average number of visible SVs from each constellation. And Fig. 3.3b shows how the acceptable fault probability values decrease when more SVs are visible. The results show that, in all cases, a V-ARAIM exclusion function would be required for continuity if any one of the constellations is subject to P_{sat} of

10^{-4} , or P_{const} of 10^{-3} .

3.4 Requirements for Exclusion Function

3.4.1 Requirements for V-ARAIM Exclusion. According to the analyses in last section, a V-ARAIM exclusion function is required to improve continuity when four constellations are in use, and/or the constellations are subject to larger fault probabilities. In this case, only those detection events that the exclusion function cannot resolve would result in LOC. These can further separated into two classes: (1) under FF conditions, we can have a FA followed by no exclusion (FANE), and (2) in the case of a FD with no exclusion (FDNE) after. The continuity requirements for the V-ARAIM FDE functions must be defined to limit these two events.

The probability of FANE can be quantified and bounded by the following equation:

$$mP_{FANE,V} = mP(D_0, \bar{E}_0|H_0) \lambda P_{H_0} < mP(D_0|H_0) \lambda P_{H_0} \quad (3.7)$$

where \bar{E}_0 denotes no exclusion when using all satellites in view. The upper bound of equation 3.7 is the FA event, so the LOC contribution of V-ARAIM FANE can be controlled by setting detection thresholds.

When a fault is present, the probability of LOC with an exclusion function is:

$$mP_{FDNE,V} = m \sum_{i=1}^H \gamma P(D_0, \bar{E}_0|H_i) \lambda P_{H_i} < m \sum_{i=1}^H \gamma P(\bar{E}_0|H_i) \lambda P_{H_i} \quad (3.8)$$

Limiting the bound in equation 3.8 to meet $P_{FP,V,REQ}$ can be achieved by appropriately setting exclusion thresholds. The ARAIM exclusion tests will be introduced in the next chapter.

It must be clarified that to generate the quantitative results in section 3.3, we chose an example continuity requirement allocation and example scale factors. Because we seek to build a general method that rigorously accounts for all possible LOC

contributions, conservative values were selected. Therefore, the conclusion from those example analyses may not be suitable for all operational conditions. For instance, it is not always necessary to use $m = 2$, especially for airports with widely dispersed runways. In addition, less conservative fault probabilities—for example, based on historical data—may be used when computing continuity risk. Such changes could reduce the FD probability, and may potentially lead to the conclusion that exclusion is not required for V-ARAIM even if three or four constellations are used. Further, even though we use conservative values, the green line in Figure 3.2a shows the total LOC probability bound exceeds the requirement (8×10^{-6}) by only a small amount, which might be acceptable from an operational perspective. For this reason, in the later chapters of this thesis, V-ARAIM performance is investigated separately using the FD-only function and the FDE function.

3.4.2 Requirement for H-ARAIM Exclusion. Similar to Table 3.1, Table 3.2 lists an example H-ARAIM continuity requirement $C_{REQ,H}$ allocation among the FF condition, FP condition, and all other sources.

Table 3.2. H-ARAIM Continuity Budget Allocation

$P_{FF,H,REQ}$	$P_{FP,H,REQ}$	$P_{other,H,REQ}$
4×10^{-7} / hour	5×10^{-7} / hour	10^{-7} / hour

With an exclusion function implemented, the overall H-ARAIM LOC probability is given by equation 3.9. Equations 3.10 and 3.11 express the bounds on the FANE and FDNE contributions, which should be respectively limited to be smaller than $P_{FF,H,REQ}$ and $P_{FP,H,REQ}$ in Table 3.2.

$$P_{LOC,H} = P_{FANE,H} + P_{FDNE,H} + P_{other,H} \quad (3.9)$$

$$P_{FANE,H} = P(D_0, \bar{E}_0 | H_0) P_{H_0} < P(D_0 | H_0) P_{H_0} \quad (3.10)$$

$$P_{FDNE,H} = \sum_{i=1}^H P(D_0, \bar{E}_0 | H_i) P_{Hi} < \sum_{i=1}^H P(\bar{E}_0 | H_i) P_{Hi} \quad (3.11)$$

3.5 Loss of Continuity Contribution of Unscheduled Satellite Outages

In addition to SV faults, the increased number of measurements in multi-constellation ARAIM increases the satellite outage probability, which in turn increases the continuity risk. There are two types of outage: a scheduled satellite outage (SSO) is announced at least 48 hours in advance to the user, and USO, which typically results from sudden system malfunctions or maintenance occurring outside the scheduled period [5]. Since SSO is known before the operation, it impacts availability rather than continuity. Therefore, we only account for the impact of USO on ARAIM LOC. GPS SPS PS has specified that the prior probability of USO occurrence on a single satellite (P_{USO}) is less than 2×10^{-4} [5]. Assuming the other constellations can achieve the same probability as GPS, the total probability of the user undergoing USO has exceeded $C_{REQ,H}$ significantly. In response, a new method is derived in this section to rigorously account for the USO occurrence in the continuity risk equation. H-ARAIM will be employed as a vehicle to present this method, because LOC is a more serious event in H-ARAIM operations, and $C_{REQ,H}$ is much more stringent than $C_{REQ,V}$.

The principle of this approach is unifying all the LOC contributions from both measurement faults and USO into the P_{alert} in equation 3.1, and limiting those contributions by setting FDE thresholds. The allocation in Table 3.2 is also applied here, where 10^{-7} /hour is allocated to $P_{other,H}$ and 9×10^{-7} /hour is for the overall P_{alert} . By including all the USO conditions, equation 3.9 becomes:

$$P_{LOC,H} = \sum_{s=0}^H (P_{FANE|O_s} + P_{FDNE|O_s}) P_{O_s} + P_{other,H} \quad (3.12a)$$

$$= \sum_{s=0}^H \left(\sum_{i=0}^{H_s} P(D_s, \bar{E}_s | H_i, O_s) P_{Hi} \right) P_{O_s} + P_{other,H} \quad (3.12b)$$

where O_s represents the USO occurrence on satellite subset $s = 0, 1, \dots, H$, and s de-

notes all possible USO combinations including the OF condition (O_0), single-satellite USO, dual-satellite USO, etc. P_{O_s} is the prior probability of the event ‘ O_s ’. D_s indicates that detection occurs using the remaining satellites when there is a USO event ‘ O_s ’, where ‘ $s = 0$ ’ denotes all satellites are in view. \bar{E}_s implies no exclusion can be made using the remaining satellites under the condition ‘ O_s ’. In addition, since P_{H_i} and H_i are also conditioned on ‘ O_s ’, the fault hypotheses applies for the remaining satellites. Therefore, the total number of hypotheses is noted as H_s to distinguish from the all-in-view set.

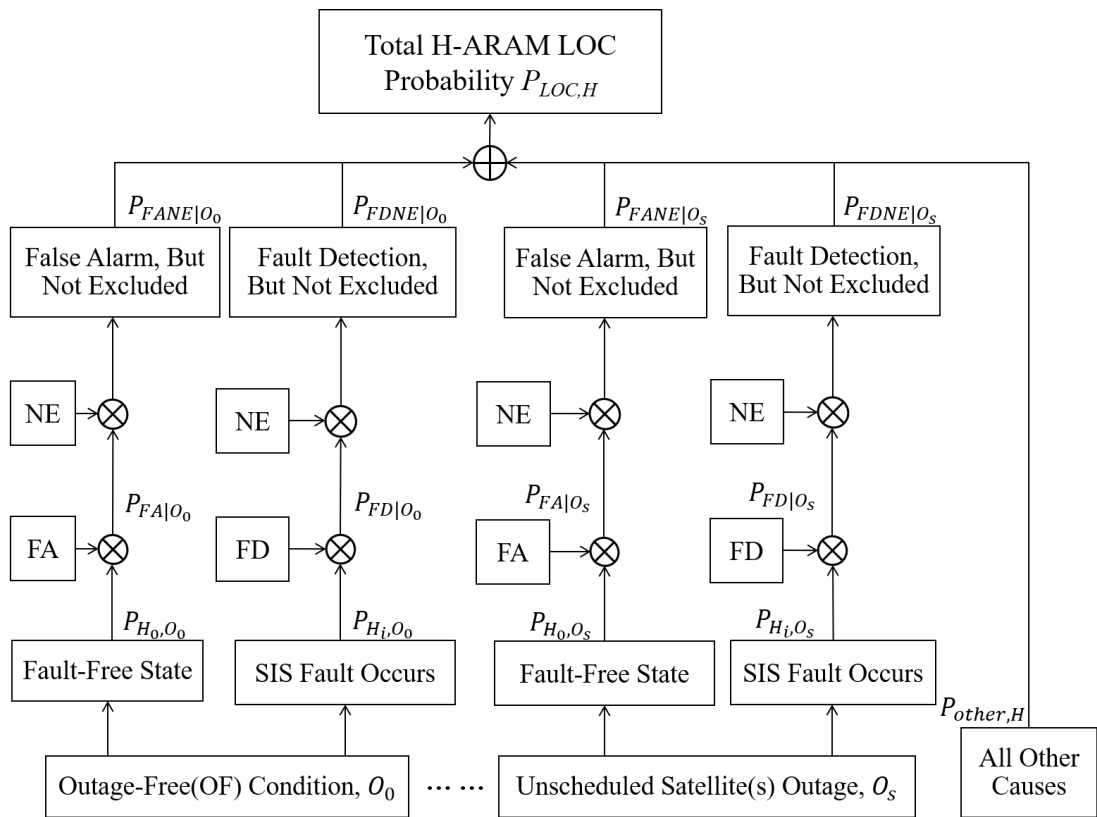


Figure 3.4. H-ARAIM LOC Tree.

Figure 3.4 shows a H-ARAIM continuity tree that visually expresses equation 3.12. It is expanded from Figure 3.1 by expressing $P_{alert,H}$ over all the USO conditions and associated fault modes. The LOC contributions can be controlled by setting the fault detection and exclusion threshold. Therefore, similar to section 3.4, the

requirements of the FDE function under USO scenario are given by limiting each contribution of Figure 3.4 to meet their allocated continuity budgets. The section provide two ways to allocate the $C_{REQ,H}$ among all the USO conditions, depending on whether or not the budgets for FANE and FDNE over ‘ O_s ’ are equally allocated.

3.5.1 Equal Allocation over USO Conditions. The overall H-ARAIM LOC equation 3.12 can be bounded as:

$$P_{LOC,H} < \sum_{s=0}^H \left(P(D_s|H_0, O_s) P_{H0} + \sum_{i=1}^{H_s} P(\bar{E}_k|H_i, O_s) P_{Hi} \right) P_{Os} + P_{other,H} \quad (3.13)$$

Under the USO condition ‘ O_s ’, the two terms inside the bracket of equation 3.13 respectively bound the FANE and FDNE events. Since the summation of P_{Os} over all USO events is 1, the same budgets as Table 3.2 can be applied in this case for setting FDE thresholds. Therefore, regardless of USO, there is only one $P_{FF,H,REQ}$ to set the detection threshold, and one $P_{FP,H,REQ}$ to set the exclusion threshold. Operationally, this allocation does not require the user to know whether there is a USO or not.

3.5.2 Non-Equal Allocation over USO Conditions. If the receiver always knows whether there is a USO present at *any* time epoch, the allocated continuity budget into ‘ O_s ’ may vary. Depending on the USO conditions during operation, the receiver can use different budgets to compute FDE thresholds. Therefore, the total budget for ‘ $P_{alert,H}$ ’ can be allocated optimally among the events ‘ O_s ’ to minimize the associated integrity risk. The optimization process is not addressed in this thesis, and an example case is presented in this subsection to demonstrate the idea and to make comparison with the equal allocation in the last subsection.

Depending on the presence of USO, equation 3.12 is divided into (a) FANE and FDNE under OF ($s = 0$) condition and (b) under USO ($s \neq 0$) cases:

$$P_{LOC,H} = P_{FANE,OF} + P_{FDNE,OF} + P_{FANE,USO} + P_{FDNE,USO} + P_{other,H} \quad (3.14)$$

$$\begin{aligned} <P(D_0|H_0, O_0) P_{H_0} P_{O_0} + \sum_{i=1}^{H_0} P(\bar{E}_0|H_i, O_0) P_{H_i} P_{O_0} + P_{other,H} \\ + \sum_{s=1}^H (P(D_s|H_0, O_s) P_{H_0}) P_{O_s} + \sum_{s=1}^H \left(\sum_{i=1}^{H_s} P(\bar{E}_k|H_i, O_s) P_{H_i} \right) P_{O_s} \end{aligned} \quad (3.15)$$

Table 3.3. H-ARAIM Continuity Budget Allocation among OF and USO Conditions

$P_{FF,OF,REQ}$	$P_{FP,OF,REQ}$	$P_{FF,USO,REQ}$	$P_{FP,USO,REQ}$
$2 \times 10^{-7} / \text{hour}$	$2 \times 10^{-7} / \text{hour}$	$2 \times 10^{-7} / \text{hour}$	$3 \times 10^{-7} / \text{hour}$

Table 3.3 lists the example requirement allocation for the four components in equation 3.14. The FDE thresholds can be obtained by respectively limiting each term to be smaller than the allocated requirements. Under the USO conditions, the thresholds can be set much tighter than under the OF conditions, because the last two components of equation 3.14 account for the USO prior probabilities. Therefore, their corresponding contributions to the integrity risk can be reduced. In addition, in $P_{FDNE,USO}$, the sum of the products of the fault and USO prior probabilities is generally very small. When the sum is already smaller than the requirement $P_{FP,USO,REQ}$, there is no need to perform the exclusion function under USO conditions. However, this approach assumes that the receiver always knows the USO conditions during flight, and the assumption itself is worth discussing. Operationally, the user can recognize the cases in which lock on a particular satellite is suddenly lost due to USO, but it is questionable whether the user knows USO conditions at the starting point of the operation. In particular, it is more challenging to determine when the lost satellite is reinstated after suffering from a USO. Therefore, both equal and non-equal allocations are investigated in later chapters to quantify ARAIM navigation performance.

CHAPTER 4

FAULT EXCLUSION SCHEME

This chapter presents a detailed, step-by-step description of a new SS based exclusion algorithm and derives the associated FDE integrity risk bound. The algorithm is primarily intended to serve as an exclusion function for H-ARAIM, but it can also be directly applied to improve V-ARAIM continuity when needed. Moreover, it can additionally be used to reduce the unavailable periods when an aircraft has detected a fault *prior* to the intended operation. Since the algorithm is implemented in real-time, the user may be exposed in USO conditions ‘ O_s ’ where $s \neq 0$. But to lighten the notations, the subscript ‘ O_s ’ or ‘ s ’ are eliminated in the first three sections, because the derivations are all under this condition. The USO notations come back in the last section for the predictive integrity risk (or PL) evaluation, and such cases will be clarified.

4.1 Real-Time FDE Algorithm

Figure 4.1 is the flow diagram that describes the real-time FDE procedure. It starts with evaluating integrity risk P_{HMI} (or PL) of the current geometry. The remaining FDE steps will be implemented only if the integrity risk requirement I_{REQ} (or AL) for the intended operation is met. The details of how to compute P_{HMI} (and PL) will be provided later in section 4.3. For continuity, the key design element is the follow-up exclusion step after detection, and the mechanism to determine which SV(s) to exclude, both of which will be described shortly. For H-ARAIM applications, the probability of GPS constellation fault is assumed to be 10^{-8} , so it can be used to exclude other constellation faults even in the dual-constellation case. However, for V-ARAIM operations, the GPS constellation fault probability cannot be assumed

negligible, so at least three constellations would be required to exclude a constellation fault.

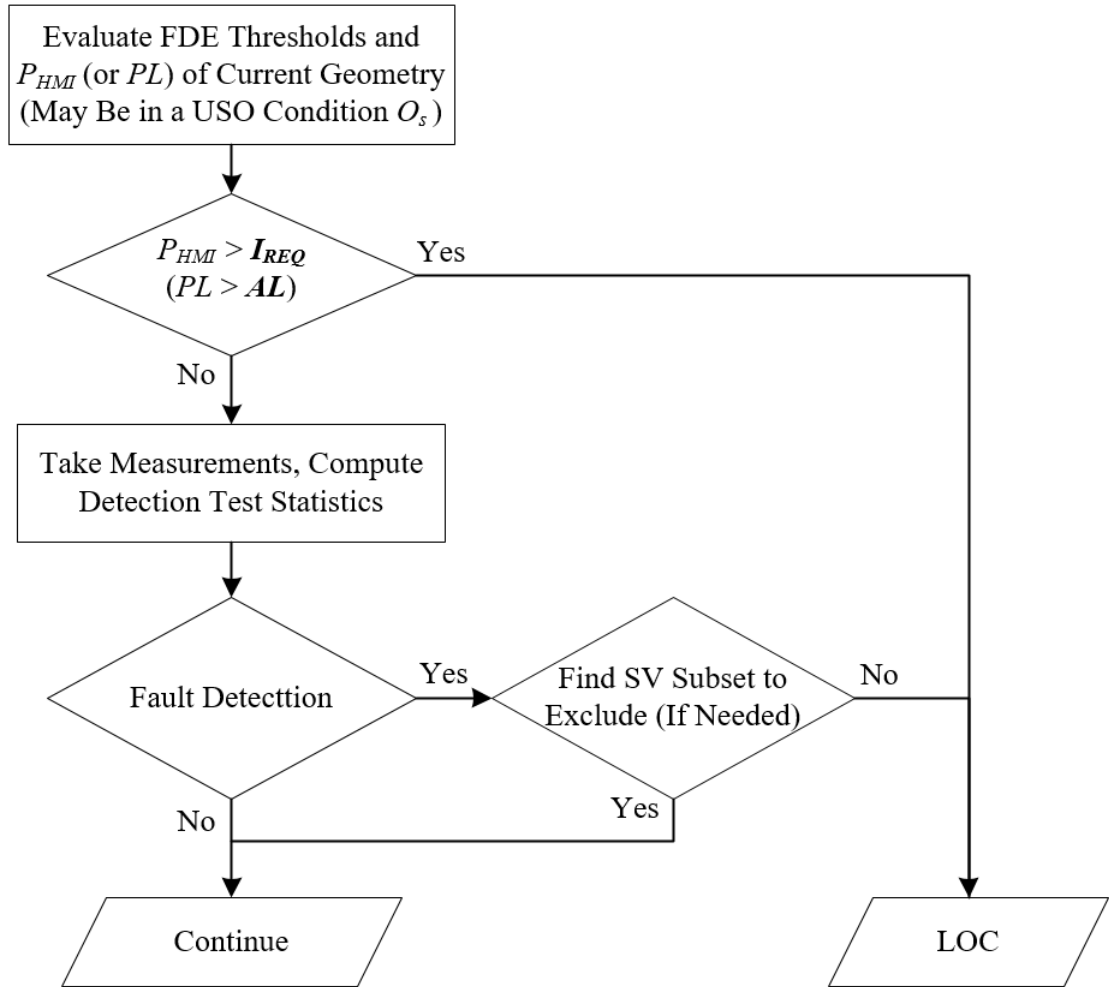


Figure 4.1. Flow Diagram of the Real-Time FDE Process.

The baseline multiple MHSS ARAIM detection algorithm has been described in section 2.4. Let the normalized detection test statistics express as [33]:

$$q_d = \frac{\Delta_d}{\sigma_{\Delta_d}} \quad (4.1)$$

Once an alarm occurs, the exclusion function will be executed. In this design, the exclusion function is composed of a two-step process. The first step determines the exclusion option order, by arraying all the q_d in a magnitude descending sequence.

The first exclusion option corresponds to the fault mode with maximum statistic. The principle behind formatting in this order is due to the distributions of SS detection statistics. Because the statistics are the differences between the all-in-view and satellite subset solutions in position domain, under a faulted condition it is most likely that the one corresponding to the actual fault is much larger than the others. To visualize this basis, a parity space representation will be demonstrated later. It is worth mentioning that the purpose of the first step is to provide an efficient route for the algorithm to quickly make the final exclusion decision. It is true that there are cases when the actual fault mode does not result in the maximum statistic, especially when the constellation is exposed to more than one SV failure. That is why the second step has to be applied.

In the second step, the final exclusion option is determined. It employs a second layer detection test to confirm there is no alarm in the satellite subset. The normalized exclusion statistics (or second layer detection statistics) are defined as:

$$q_{e,l} = \frac{\hat{x}_e - \hat{x}_{e,l}}{\sigma_{\Delta_{e,l}}} = \frac{\varepsilon_e - \varepsilon_{e,l}}{\sigma_{\Delta_{e,l}}}, \text{ for } l = 1 \dots h_e. \quad (4.2)$$

where $\hat{x}_{e,l}$ is the least squares position estimate using remaining satellites after excluding fault mode e , $e = 1, \dots, h$, except the ones in the second layer fault mode l , $l = 1, \dots, h_e$. $\sigma_{\Delta_{e,l}}$ is the standard deviation of the exclusion statistic $\Delta_{e,l}$, which is defined as the difference between \hat{x}_e and $\hat{x}_{e,l}$. $\varepsilon_{e,l}$ is the position estimate error of $\hat{x}_{e,l}$, normally distributed with bias $b_{e,l}$ and standard deviation $\sigma_{e,l}$.

This step goes through all the exclusion options following the order determined in step 1. For each option, the exclusion test compares each $q_{e,l}$ with its associated threshold $T_{e,l}$, which is determined by the continuity requirement. If all the exclusion statistics are within their thresholds, then the associated satellite(s) in the candidate fault mode is/are chosen to be excluded. However, it is possible that no exclusion can be made even after testing all the options. This case will result in LOC, and its

probability of occurrence has been captured in equations 3.8 and 3.11. In summary, two conditions will result in a satellite subset j being excluded (E_j): (a) there is no second layer detection after excluding this subset (\bar{D}_j); (b) this subset corresponds to the maximum detection statistic among the subsets that pass the exclusion test (MAX_j). The following subsection employs the example introduced in section 2.5 to help clarify this proposed algorithm.

4.1.1 Party Space Representation of the FDE Algorithm. Figure 4.2a is a recall of the detection problem of Figure 2.2, where the measurement and error models are specified in equation 2.44. Because measurement 1 is faulted, the associated fault mode line \mathbf{w}_1 is labeled red. As the fault magnitude varies, the parity vector \mathbf{p} will move along \mathbf{w}_1 with small deviation orthogonal to \mathbf{w}_1 due to nominal noise on measurements 2 and 3. In Figure 4.2a, the fault is detected, and the first step of the exclusion function will return an exclusion option order first attempting exclusion of measurement 1, then 2 and 3.

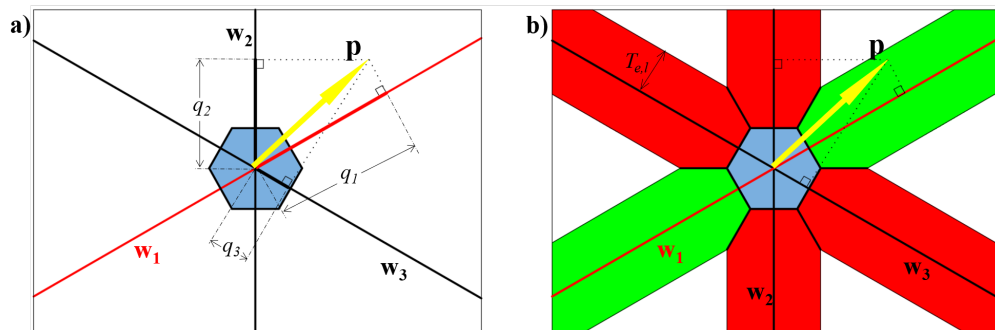


Figure 4.2. Parity Space Representation of ARAIM FDE Algorithm.

As shown in Figure 4.2b, the second exclusion step examines if there is second layer detection event. The green band corresponds to the correct exclusion event in which measurement 1 will be excluded. The red band result in wrong exclusion since measurements 2 and 3 will be excluded. The widths of those bands are determined by the magnitude of the exclusion threshold $T_{e,l}$. For this example, the exclusion function

first confirms there is no detection after excluding measurement 1. Therefore, the final exclusion decision is made at the first attempt, and there is no need to test other options.

4.2 Evaluating FDE Thresholds

With the FDE algorithm being specified, the events of fault detection (D_0) and no exclusion (\bar{E}_0) can be expressed in mathematical terms. The detection thresholds T_d and exclusion thresholds $T_{i,l}$ can be respectively computed based on the allocated continuity budgets in Table 3.2.

Since the upper bound term in equation 3.10 is identical to the FA equation 2.21 in section 2.4.3, equation 2.23 is used to evaluate T_d , where the $P_{FA,REQ}$ is replaced by the $P_{FF,H,REQ}$ of Table 3.2. According to the design, \bar{E}_0 occurs when no exclusion option can be validated, i.e., when a second layer detection occurs: $\bigcap_{e=1}^h \left(\bigcup_{l=1}^{h_e} |q_{e,l}| > T_{e,l} \right)$. Therefore, for H-ARAIM, equation 3.11 becomes:

$$P_{FDNE,H} < \sum_{i=1}^h P \left(\bigcap_{e=1}^h \left(\bigcup_{l=1}^{h_e} |q_{e,l}| > T_{e,l} \right) | H_i \right) P_{Hi} + P_{NM} \quad (4.3a)$$

$$< \sum_{i=1}^h P \left(\bigcup_{l=1}^{h_e} |q_{i,l}| > T_{i,l} | H_0 \right) P_{Hi} + P_{NM} \quad (4.3b)$$

$$< \sum_{i=1}^h \sum_{l=1}^{h_e} P(|q_{i,l}| > T_{i,l} | H_0) P_{Hi} + P_{NM} < P_{FP,H,REQ} \quad (4.3c)$$

The bound from equation 4.3a to 4.3b is noteworthy, where only one exclusion option associated with the fault hypothesis is considered, i.e., $e = i$. Since the actual fault is excluded, the second layer detection statistics in equation 4.3c are fault free (H_0). Equation 4.3c can be applied to set the exclusion thresholds over all the monitored fault hypotheses. In this work, an even allocation of $P_{FP,H,REQ}$ is adopted. Therefore,

$$T_{i,l} = Q^{-1} \left\{ \frac{P_{FP,H,REQ,Hi}}{2 \cdot h_e} \right\}, \text{ where } P_{FP,H,REQ,Hi} = \frac{P_{FP,H,REQ}}{h \cdot P_{Hi}} \quad (4.4)$$

It is worth clarifying that the derivations above are based on the requirements for H-ARAIM exclusion presented in section 3.4.2. When USO is considered in the $P_{LOC,H}$ of equation 3.12, this approach is only applicable for the case of equal allocation of $C_{REQ,H}$ over USO conditions, i.e., section 3.5.1. For the non-equal allocation case in section 3.5.2, the corresponding FDE thresholds are derived in Appendix A. Moreover, for V-ARAIM, if exclusion is implemented, this approach can also be applied. A minor modification may be needed to accommodate the multipliers in equations 3.7 and 3.8.

4.3 Bounding the Instantaneous Integrity Risk

As shown in Figure 4.1, before detection, the receiver does not know whether there is a fault detection or not and which satellite subset needs to be excluded. Therefore, the FDE integrity risk equation must account for the risk introduced by all possible exclusion options:

$${}^I P_{HMI} = P(HI_0, \bar{D}_0) + \sum_{j=1}^h P(HI_j, E_j, D_0) \quad (4.5)$$

where the upper left superscript ‘ I ’ in ${}^I P_{HMI}$ refers to the ‘instantaneous’ risk. HI_0 and HI_j respectively represent the events that hazardous information exists in (a) full-set position estimate and in (b) subset estimate after excluding satellites in fault mode j . The first term on the right side, which is identical to equation 2.9, is the integrity risk using the FD function only. The additional terms (i.e., the summation) carry the cost of increased integrity risk by implementing exclusion. Equation 4.5 can be bounded by employing the multiple fault hypothesis approach:

$${}^I P_{HMI} = \sum_{i=0}^h \max_{f_i} \left(\begin{array}{c} P(HI_0, \bar{D}_0 | H_i, f_i) \\ + \sum_{j=1}^h P(HI_j, \bar{D}_j, MAX_j, D_0 | H_i, f_i) \end{array} \right) P_{Hi} + P_{NM} \quad (4.6)$$

There is an expansion of notation from equation 4.5 to 4.6, where the exclu-

sion event E_j in the former is decomposed in terms of both \bar{D}_j and MAX_j . Under the hypothesis H_i , the actual fault vector is f_i , which can be fully described by its direction and magnitude [11]. The worst-case fault is obtained when the conditional FDE integrity risk for H_i (the summation over all exclusion options under hypothesis H_i) is maximized. However, directly evaluating ${}^I P_{HMI}$ using equation 4.6 is almost impossible because (a) searching for the worst-case fault over all exclusion options is an arduous task, especially when H_i is a multiple-satellite fault mode, and (b) the correlations between the events in each exclusion option are complex. In response, we seek a more computationally efficient upper bound.

$${}^I P_{HMI} < \sum_{i=0}^h P(HI_0, \bar{D}_0 | H_i) P_{Hi} + \sum_{i=0}^h \sum_{j=1}^h P(HI_j, \bar{D}_j, MAX_j, D_0 | H_i) P_{Hi} + P_{NM} \quad (4.7)$$

In equation 4.7, f_i have been implicitly selected to maximize each term *individually*. In contrast, in equation 4.6, a single fault mode is selected to maximize the *sum* of all the terms. Therefore, summing the maximized individual risks using equation 4.7 always bounds the maximized summed risk in equation 4.6.

The first summation term on the right side of equation 4.7 corresponds to the detection-only integrity risk, which is the same as equation 2.20 and its upper bound has been established in equation 2.28. Now turning our attention to the second (double summation) term on the right side of 4.7, define ${}^I P_{HMI,i,j}$ as the conditional integrity risk after excluding E_j under hypothesis H_i . For the FF condition, H_0 , since the position estimation error ε_j is expected to be significantly smaller than AL, ${}^I P_{HMI,0,j}$ can still be tightly bounded by eliminating all other information:

$${}^I P_{HMI,0,j} = P(HI_j, \bar{D}_j, MAX_j, D_0 | H_0) \quad (4.8a)$$

$$< P(HI_j | H_0) = P(|\varepsilon_j| > \ell | H_0) \quad (4.8b)$$

For the other fault hypotheses H_i , the exclusion events can be classified into

two categories: correct exclusion (CE) and wrong exclusion (WE). Equation 4.8b can also be applied to tightly bound the integrity risk of CE event, because if the actual faulted satellite subset S_i belongs to the excluded subset S_j , the post-exclusion position estimate \hat{x}_j is also FF. In regard to the WE event, the following bounding steps are employed, leading to a final upper bound of equation 4.9d that can be evaluated with great computational efficiency.

$${}^I P_{HMI,i,j} = P(HI_j, \bar{D}_j, MAX_j, D_0 | H_i) \quad (4.9a)$$

$$< P(HI_j, \bar{D}_j | H_i) = P\left(|\varepsilon_j| > \ell, \bigcap_{l=1}^{h_e} |q_{j,l}| < T_{j,l} | H_i\right) \quad (4.9b)$$

$$< P(|\varepsilon_j| > \ell, |q_{j,i}| < T_{j,i} | H_i) \quad (4.9c)$$

$$< P(|\varepsilon_{j,i}| + \sigma_{\Delta_{j,i}} T_{j,i} > \ell | H_i) \quad (4.9d)$$

In the progression from equation 4.9a to 4.9b, the knowledge of MAX_j and D_0 is eliminated, which implies the exclusion option order does not impact the final integrity risk upper bound. This is consistent with the original motivation of designating the order, which aims at speeding up the real-time exclusion decision-making process, not improving integrity. In summary, the overall FDE integrity risk associated with the proposed algorithm can be upper bounded and evaluated by substituting equations 2.28, 4.8 and 4.9d into equation 4.7 [24]:

$${}^I P_{HMI} < P(|\varepsilon_0| > \ell | H_0) P_{H_0} + \sum_{i=1}^h P(|\varepsilon_i| + \sigma_{\Delta_i} T_i > \ell | H_i) P_{H_i} \\ + \sum_{j=1}^h \left(P(|\varepsilon_j| > \ell | H_0) P_{H_0} + \sum_{\substack{i=1 \\ S_i \subseteq S_j}}^h P(|\varepsilon_j| > \ell | H_i) P_{H_i} \right. \\ \left. + \sum_{\substack{i=1 \\ S_i \not\subseteq S_j}}^h P(|\varepsilon_{j,i}| + \sigma_{\Delta_{j,i}} T_{j,i} > \ell | H_i) P_{H_i} \right) + P_{NM} \quad (4.10)$$

Alternatively, [39] has developed the corresponding PL approach to equation 4.10. The derivations of equation 4.11 and the method to solve it can respectively be

found in appendix D and E of [39].

$$\begin{aligned}
I_{REQ} < 2Q \left(\frac{PL - b_0}{\sigma_0} \right) + \sum_{i=1}^h Q \left(\frac{PL - b_i - \sigma_{\Delta_i} T_i}{\sigma_i} \right) P_{Hi} \\
+ \sum_{j=1}^h \left(2Q \left(\frac{PL - b_j}{\sigma_j} \right) + \sum_{\substack{i=1 \\ S_i \notin S_j}}^h Q \left(\frac{PL - b_{j,i} - \sigma_{\Delta_{j,i}} T_{j,i}}{\sigma_{j,i}} \right) P_{Hi} \right) + P_{NM}
\end{aligned} \tag{4.11}$$

4.4 Predictive Integrity Risk

To quantify the expected ARAIM navigation performance, an offline analysis is usually carried out. To do this, the integrity risk is predicted prior to the operations. In principle, the predictive integrity risk ${}^P P_{HMI}$ needs to characterize all the scenarios that the user may encounter in real-time. However, it is not feasible to exactly capture the complex and various operational environments in advance, because the actual satellite geometry may change due to many factors, such as the aircraft banking. Therefore, the evaluation of ${}^P P_{HMI}$ depends on the assumptions on the real-time operations. To control the variables when addressing the ARAIM navigation performance, it is first assumed that the predicted satellite geometries are identical to the actual real-time geometries. So the instantaneous integrity risks in equations 2.28 and 4.10 are the same as ${}^P P_{HMI}$, and they will be employed to respectively analyze the performance using FD function only and both FDE functions.

In addition, the impact of USO on the overall ARAIM navigation performance must be quantified; the corresponding continuity risk equation was provided in section 3.5. The associated predictive integrity risk, which accounts for the integrity threat when the user undergoes USO, can be expressed and bounded as:

$${}^P P_{HMI} = \sum_{s=0}^H P_{HMI|O_s} P_{O_s} < \sum_{s=0}^{h_{uso}} P_{HMI|O_s} P_{O_s} + P_{NM,USO} \tag{4.12}$$

where $P_{HMI|O_s}$ is the same as the ${}^I P_{HMI}$ in section 4.3 except the subscript ‘ O_s ’ is

recovered. $P_{NM,USO}$ accounts for the cases when USO occurs on multiple satellites simultaneously. It is very similar to P_{NM} : since their prior probabilities are very small, this term is regarded as a not monitored component. The methods for evaluating P_{NM} can also be applied here to determine h_{uso} and compute $P_{NM,USO}$, by replacing the P_{sat} and P_{const} with P_{USO} .

As suggested by equation 4.12, ${}^P P_{HMI}$ is a weighted sum of the conditional integrity risk under O_s . If the ‘equal allocation’ method for $C_{REQ,H}$ (section 3.5.1) is employed, the $P_{HMI|O_s}$ are the same for all $s = 0, 1, \dots, h_{uso}$:

$$P_{HMI|O_s} = P(HI_s, \bar{D}_s | O_s) + \sum_{j=1}^{h_s} P(HI_{j_s}, E_{j_s}, D_s | O_s) \quad (4.13)$$

Again, equation 4.13 is the same to 4.5 except the subscripts for USO events are recovered. So it can be solved using the upper bound of equation 4.10. If the ‘non-equal allocation’ approach (section 3.5.2) is used, depending on the allocation in Table 3.3, it may be concluded that exclusion function is not required under USO condition. Therefore, $P_{HMI|O_s}$ does not need to account for the exclusion options when $s \neq 0$, i.e.:

$$P_{HMI|O_s} = P(HI_s, \bar{D}_s | O_s) \quad (4.14)$$

Equation 4.14 can be upper bounded by equation 2.28. As a result, depending on whether or not equally allocating the continuity budget for FANE and FDNE over ‘ O_s ’, the predictive integrity risk ${}^P P_{HMI}$ can be computed by plugging equations 4.13 and/or 4.14 into 4.12.

CHAPTER 5

MULTI-CONSTELLATION ARAIM NAVIGATION PERFORMANCE

With the theoretical methods being derived in previous chapters, this chapter comprehensively investigates multi-constellation ARAIM navigation performance and addresses the impact of increased numbers of measurements on integrity and continuity. The analyses are performed based on the simulation conditions specified in Table 2.3. To investigate the achievable navigation performance with multiple constellations, GLONASS and Beidou are employed as additional sources to the dual-constellation (GPS + Galileo) scenario. Moreover, different values for the ISM parameters are used to demonstrate the sensitivity of ARAIM performance over different constellation qualities. The specific criteria will be provided in detail for each simulation. In Chapter 3, it was shown that an exclusion function must be implemented to improve H-ARAIM continuity, and whether or not an exclusion function is needed for V-ARAIM largely depends on the operational scenario. In general, airborne exclusion will likely not be required for dual-constellation V-ARAIM but may be needed when four constellations are employed. Therefore, the sections in this chapter respectively analyze the performance (a) using FD function only for V-ARAIM with *nominal* ISM parameters, (b) using FD function only for V-ARAIM with *degraded* ISM parameters, (c) applying both detection and exclusion functions for four-constellation V-ARAIM and dual-constellation H-ARAIM, and (d) applying the new method to account for the impact of USO on the navigation performance. The goal of the first two analysis is to quantify achievable V-ARAIM navigation performance over various numbers and qualities of the constellations to demonstrate the impact of increased measurement redundancy on navigation integrity. The last two analyses validate the exclusion scheme, and shows the resulting ARAIM availability

while meeting both integrity and continuity requirements.

5.1 Achievable V-ARAIM FD Navigation Performance with Multiple Constellations

This section addresses V-ARAIM navigation integrity as a function of the number of the constellations. The baseline 23 GLONASS and 27 Beidou, whose almanacs are also available in [21], are employed. It is first assumed that those two newly added constellations can provide GPS-equivalent performance. So the following nominal ISM values are applied for all four constellations: $P_{sat} = 10^{-5}$, $P_{const} = 10^{-4}$, $\sigma_{URA} = 1$ m, $b_{nom} = 0.75$ m. The analysis investigates the potential benefits to V-ARAIM performance by adding constellations with high performance, and therefore helps answer the following question: whether adding more measurements always improves navigation performance and what service levels can be achieved. Figure 5.1 demonstrates the achievable vertical VPL with two, three and four constellations.

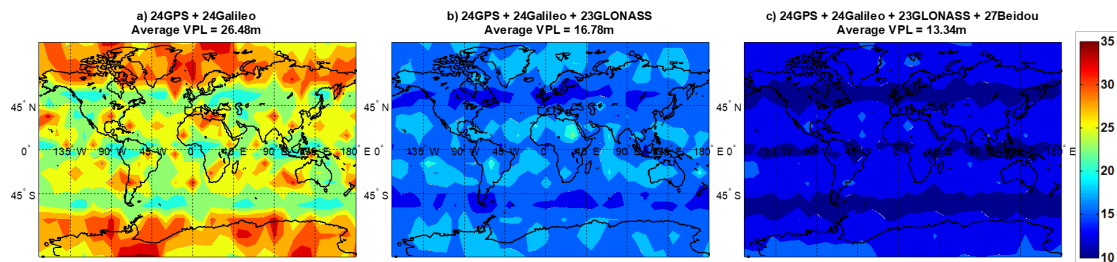


Figure 5.1. Achievable VPL Levels (in meters) Using Constellations with Equivalent Performance to GPS.

Table 5.1 expresses the performance in terms of 99.5% availability coverages with varying VAL. Because VAL is the most stringent requirement criterion, it is employed here to determine V-ARAIM availability. The results indicate that adding constellations with GPS-equivalent performance significantly improves V-ARAIM navigation integrity. With four constellations, high coverage can be achieved for VAL as low as 15m. However, Figure 5.1c shows that a VAL of 10 m, which is required for precision Category I approach, still cannot be attained.

Table 5.1. 99.5% Availability Coverage Using Constellations with Equivalent Performance to GPS

VAL	Two Constellations	Three Constellations	Four Constellations
15 m	0%	14%	94.75%
20 m	0%	97%	100%
35 m	98.37%	100%	100%

5.2 Sensitivity Analysis of V-ARAIM FD Navigation Performance to ISM

For V-ARAIM, the ISM values in the baseline simulations in the last two sections were based on the GPS performance. However, newly developed constellations may not achieve the same performance level. Moreover, even GPS only commits a minimum σ_{URA} of 2.4 m instead of 1 m. So those ISM values may be optimistic for all constellations. In response, sensitivity analyses to the ISM are carried out in following section.

5.2.1 Adding Constellations with Lower Performance Levels. Conservative ISM values may be used for constellations that are at the early phases of deployment, or if the historical observations on those constellations show a greater number of faults and/or larger errors than specified by the CSP. This analysis addresses the impact of such constellations on V-ARAIM performance. It is assumed GPS and Galileo constellations are subject to the nominal ISM values used in section 5.1, but two sets of conservative ISM values are considered for GLONASS and Beidou: (1) $P_{sat} = 10^{-4}$, $P_{const} = 10^{-4}$, $\sigma_{URA} = 2.4$ m, $b_{nom} = 1.5$ m; (2) $P_{sat} = 10^{-4}$, $P_{const} = 10^{-3}$, $\sigma_{URA} = 4.8$ m, $b_{nom} = 2$ m. Figures 5.2 and 5.3 respectively show the VPL maps for these two example cases by adding one and two constellations with limited performance level.

Table 5.2 shows 99.5% availability coverage results of the analyses. The two

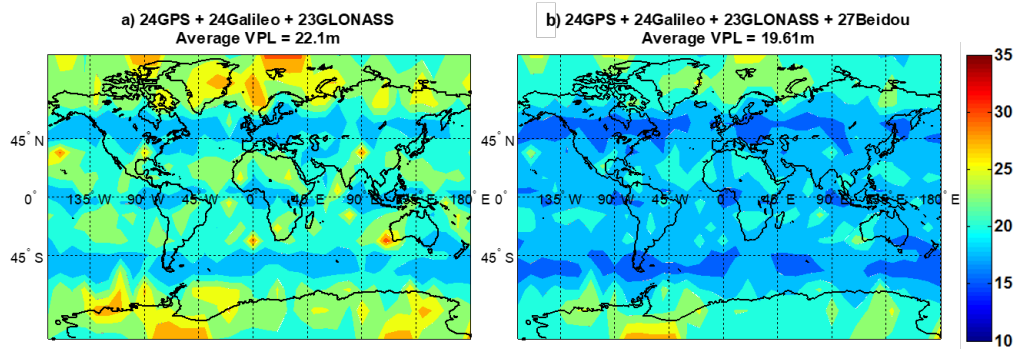


Figure 5.2. Achievable VPL Levels (in meters) Using Constellations with ISM Values in Set 1.

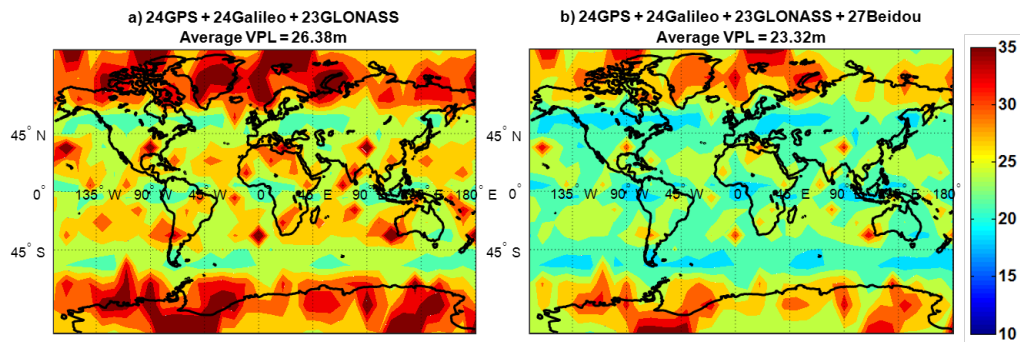


Figure 5.3. Achievable VPL Levels (in meters) Using Constellations with ISM Values in Set 2.

coverages in the 3rd and 4th columns are obtained using the ISM values of sets 1 and 2. It can be observed that new constellations with larger ISM values can still provide beneficial improvements to V-ARAIM navigation performance. However, when using the values in set 2, there is no significant change in the availability performance. Since adding new constellations always increases computational load, it is suggested that poor constellations such as the ones in Figure 5.3 not be used for ARAIM operations.

5.2.2 V-ARAIM FD Performance Using Currently Broadcast GPS σ_{URA} .

The third analysis investigates multi-constellation ARAIM performance using currently lowest broadcast σ_{URA} value. Although actual ranging error is significantly better, for now the GPS CSP commits only to a minimum σ_{URA} of 2.4 m. This analysis is achieved by using $\sigma_{URA} = 2.4$ m for all constellations, and other ISM values

Table 5.2. 99.5% Availability Coverage Using Constellations with Equivalent Performance to GPS

VAL	Two Constellations	Three Constellations	Four Constellations
20 m	0%	32.97% / 0%	76.03% / 0%
35 m	98.37%	100% / 98.83%	100% / 100%

are set the same as the ones used in section 5.1. The results in Fig. 7 and Table 7 indicate that even with the currently achieved σ_{URA} , LPV-200 operation can still be provided using three or four constellations.

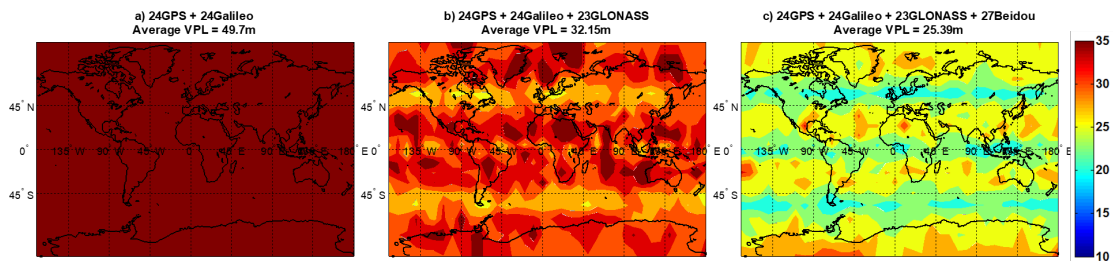


Figure 5.4. Achievable VPL Levels (in meters) Using Constellations with Currently Broadcast GPS σ_{URA} .

Table 5.3. 99.5% Availability Coverage Using Constellations with Currently Broadcast GPS σ_{URA}

VAL	Two Constellations	Three Constellations	Four Constellations
35 m	0%	85.15%	100%

5.3 Overall ARAIM Performance Using Both Detection and Exclusion

This section analyzes the overall ARAIM performance by implementing both detection and exclusion functions. In Section 3.3 (Figures 3.2 and 3.3), we identified specific scenarios that required V-ARAIM exclusion to improve continuity using four constellations. The results presented in Figure 5.5 are achieved using the nominal

ISM values in Section 5.1 for all constellations. It is shown that 100% availability coverage for LPV-200 can be achieved for V-ARAIM FDE, when requiring continuity requirements, in addition to integrity, can be simultaneously met. However, the average VPL in Figure 5.5 is decreased in comparison with Figure 5.1c, which reflects the cost of reducing continuity risk using the exclusion function.

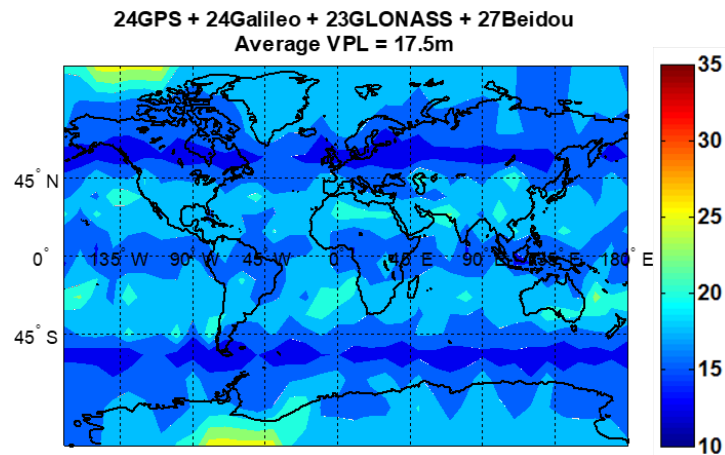


Figure 5.5. VPL Map (in meters) Using Four-Constellation V-ARAIM FDE.

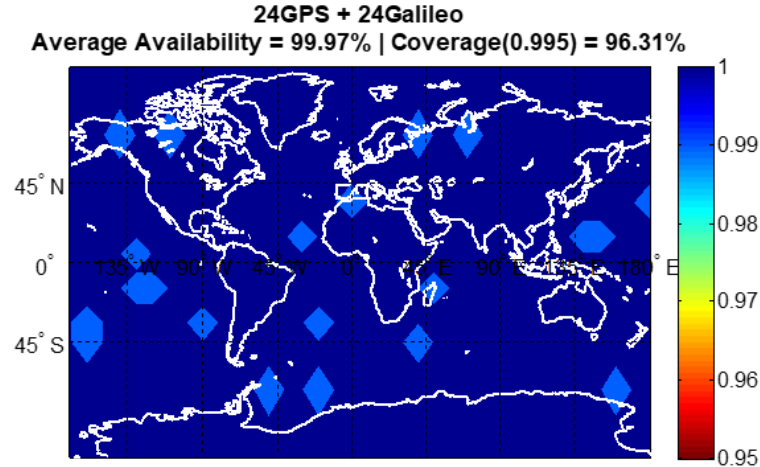


Figure 5.6. H-ARAIM Availability Map Using Dual-Constellation ARAIM FDE.

Figure 5.6 illustrates worldwide *availability performance* for RNP 0.1 using dual-constellation H-ARAIM FDE. In this simulation, the corresponding ISM values for H-ARAIM in Table 2.3 are employed. The result indicates that even with two

constellations, the proposed exclusion scheme (including the exclusion function itself and associated integrity risk bound) can provide high availability while fulfilling H-ARAIM integrity and continuity requirements.

5.4 Impact of USO on Navigation Performance

This section investigates the impact of the USO on the overall ARAIM navigation performance, using the rigorous methods developed in Chapters 3 and 4. Since USO only impacts continuity, from the operation perspective, it may not be necessary to always account for the simultaneous USOs on multiple SVs. Therefore, two analyses are carried out by (a) only accounting for single SV USOs and (b) rigorously accounting for the monitored USO modes using equation 4.12. The availability results are respectively presented in Figures 5.7 and 5.8.

Using the new method, the continuity and integrity risks are respectively evaluated using equations 3.12 and 4.12. The $C_{REQ,H}$ can be met by setting the FDE thresholds. To do this, two approaches have been described in Section 3.5. As noted in Figures 5.7 and 5.8, each analysis includes the results of using both equal (left) and non-equal (right) allocations.

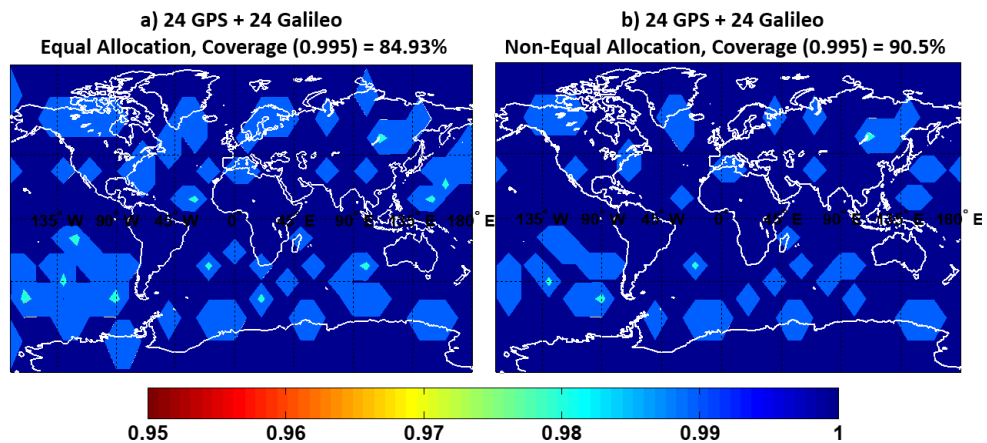


Figure 5.7. Overall H-ARAIM Availability when Accounting for Single SV USO.

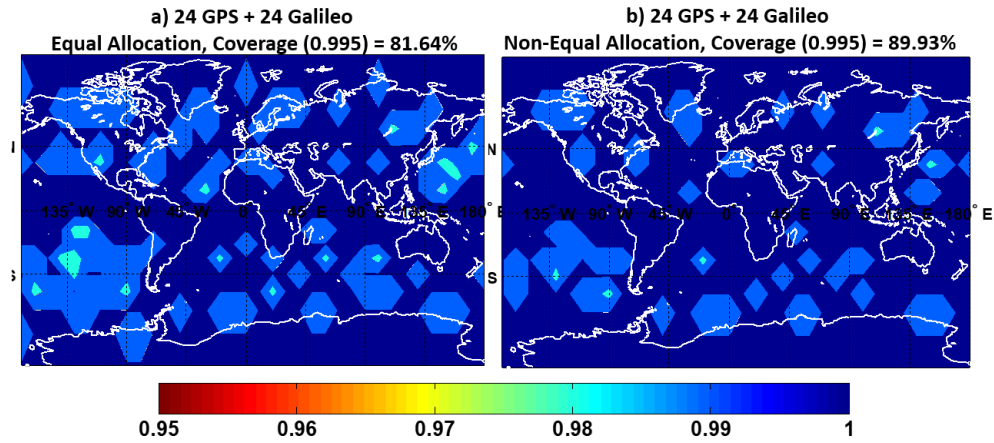


Figure 5.8. Overall H-ARAIM Availability when Accounting for Multiple SV USO.

High availabilities have been shown from the analyses, which indicates the USO does not significantly impact the ARAIM navigation performance. As mentioned in prior sections, the performance evaluated with ‘non-equal allocation’ can be further improved by optimally allocating the $C_{REQ,H}$, even though it may come at a cost in terms of computational load.

CHAPTER 6

IMPACT OF TEST STATISTIC TIME CORRELATION ON INTEGRITY AND CONTINUITY

In the current proposed ARAIM airborne algorithm and simulation methods, including the ones in the first three chapters of this thesis, the integrity and continuity risks are evaluated based on the FDE test at *one sample*. This is based on the assumption that the correlation times of the FDE test statistics are large in comparison to the exposure time interval. However, there has been some relevant GBAS research on the effect of time correlation on FA probabilities, suggesting that the actual FA probability over the exposure time can be significantly larger than previously expected [43, 44, 45, 46]. Even though the definition of test statistics and the specific operational scenario are different from GBAS, a similar problem exists in ARAIM. In particular, the exposure interval for en-route operation is much longer than for aircraft approach, so this effect may be aggravated for H-ARAIM. Therefore, this chapter investigates the impact of the test statistic time correlation on ARAIM integrity and continuity, rigorously derives the equations to evaluate the actual P_{HMI} and P_{FA} over the exposure interval, and validates the analytical results using experimental data.

6.1 Actual Integrity Risk over the Exposure Time

This section focuses on evaluating the actual P_{HMI} of the ARAIM FD function. Let T_E denote the exposure time, T_A denote the required TTA, and T_S be the sample interval. So the number of TTAs over the exposure time (N), the number of measurements over the exposure time (M), and the number of measurements over one TTA (L), are respectively:

$$N = \frac{T_E}{T_A}, M = \frac{T_E}{T_S}, \text{ and } L = \frac{T_A}{T_S} \quad (6.1)$$

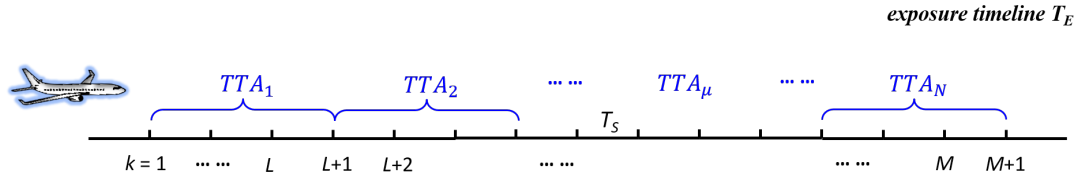


Figure 6.1. Numbers of TTAs and Time Epochs over the Exposure Interval.

Figure 6.1 shows the timeline of the exposure interval T_E . The tick marks, for which the intervals are T_S , are the time epochs denoted as $k = 1, 2, \dots, M + 1$. The subscript μ is the TTA index, $\mu = 1, 2, \dots, N$. The time epochs in each TTA_μ is $k = (\mu - 1)L + 1, \dots, \mu L + 1$.

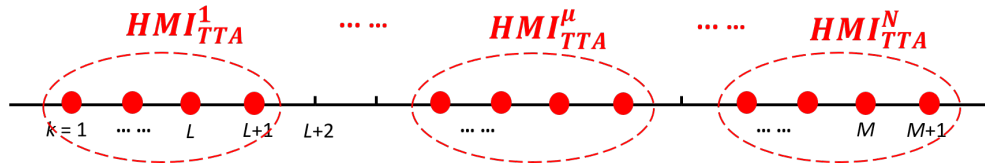


Figure 6.2. HMI Events over the Exposure Interval.

To evaluate the actual integrity risk P_{HMI}^{actual} , all the HMI events over the T_E need to be accounted for. According to ICAO, a HMI event will impact safety only if it lasts for a time period T_A . In Figure 6.2, such events are circled red and denoted as HMI_{TTA}^μ . Because a continuous HMI event over *any* TTA will result in an integrity threat, P_{HMI}^{actual} of the ARAIM FD function over this exposure time is:

$$P_{HMI}^{actual} = P \left\{ \bigcup_{\mu=1}^N HMI_{TTA}^\mu \right\} = P \left\{ \bigcup_{\mu=1}^N \left(\bigcap_{k=(\mu-1)L+1}^{\mu L+1} HMI_{sam}^k \right) \right\} \quad (6.2)$$

Equation 6.2 above includes the assumption that a detected fault is re-instated immediately in real-time operation. The use of this assumption corresponds to the worst-case integrity risk. Otherwise, there will be missing TTA intervals in T_E (μ will not be continuous from 1 to N), which results in a smaller P_{HMI}^{actual} . From the second to the third term, HMI_{TTA}^μ is further expressed in terms of the one sample HMI,

HMI_{sam}^k , which means that a joint event of *hazardous information exists* and *no detection occurs* at time epoch k . In the third term of equation 6.2, the intersection sign captures the fact that the HMI event will impact safety only if it exists over all the time epochs from $k = (\mu - 1)L + 1$ to $\mu L + 1$.

Comparing equation 6.2 to the one sample integrity risk P_{HMI}^{sam} of equation 2.9, it is not obvious which one will result in a larger integrity risk. On the one hand, the probability of having a continuous HMI over the TTA is smaller than P_{HMI}^{sam} , because there is more than one chance to detect the fault. On the other hand, there are multiple TTA intervals in the exposure time, which in turn increases P_{HMI}^{actual} . Therefore, a rigorous derivation is presented in this section to overbound the P_{HMI}^{actual} . By accounting for the multiple fault hypotheses, equation 6.2 becomes:

$$P_{HMI}^{actual} = \sum_{i=0}^H P \left\{ \bigcup_{\mu=1}^N HMI_{TTA}^{\mu} | H_i \right\} P \{ H_i \} \quad (6.3a)$$

$$= \sum_{i=0}^H \sum_{t=1}^N P \left\{ \bigcup_{\mu=t}^N HMI_{TTA}^{\mu} | H_i(t) \right\} P_{H_i}(t) \quad (6.3b)$$

From equation 6.3a to 6.3b, the fault hypotheses are explicitly expressed in terms of time. The index t defines the *onset* time of the fault, so $H_i(1)$, $H_i(2)$, ... $H_i(N)$ are mutually exclusive. In addition, because the fault onset at t only impacts the TTAs, μ starts from t under each $H_i(t)$. Equation 6.3b can be further bounded

by:

$$P_{HMI}^{actual} < \sum_{i=0}^H \left\{ \begin{aligned} &N \cdot P \{HMI_{TTA}|H_i(1)\} P_{Hi}(1) \\ &+ \sum_{t=2}^N (N-t+1) P \{HMI_{TTA}|H_i(t)\} P_{Hi}(t) \end{aligned} \right\} \quad (6.4a)$$

$$< \sum_{i=0}^H \left\{ \begin{aligned} &N \cdot P \{HMI_{TTA}|H_i\} MTTA \cdot R_{Hi} \\ &+ \frac{N^2}{2} \cdot P \{HMI_{TTA}|H_i\} T_A R_{Hi} \end{aligned} \right\} \quad (6.4b)$$

$$= \sum_{i=0}^H P \{HMI_{TTA}|H_i\} \left[N \cdot MTTA + \frac{N^2}{2} \cdot T_A \right] R_{Hi} \quad (6.4c)$$

$$< \left(N + \frac{N \cdot T_E}{2 \cdot MTTA} \right) \sum_{i=0}^H P \{HMI_{sam}|H_i\} P_{Hi} \quad (6.4d)$$

In equation 6.4a, hypothesis $H_i(1)$ is singled out because it must account for fault onsets occurring any time prior to epoch 1, which is the product of the MTTA and the failure rate R_{Hi} . In contrast, for the hypotheses at other time epochs, $H_i(t)$, only the fault onset between epochs $t-1$ and t needs to be accounted for. Since the conditional integrity risk $P \{HMI_{TTA}|H_i\}$ is independent of t , the common term in 6.4b is extracted to get 6.4c. As discussed earlier, since HMI_{TTA} is a joint event of HMI at all time epochs over TTA, from equation 6.4c to 6.4d, $P \{HMI_{TTA}|H_i\}$ can be upper bounded by $P \{HMI_{sam}|H_i\}$. Let $\beta = \left(N + \frac{N \cdot T_E}{2 \cdot MTTA} \right)$, equation 6.4d can be rewritten as:

$$P_{HMI}^{actual} < \beta P_{HMI}^{sam} \quad (6.5)$$

As the result, equation 6.5 shows a simple way to bound the P_{HMI}^{actual} by multiplying P_{HMI}^{sam} with the factor β . For V-ARAIM operations, the exposure time T_E is 150 sec since it is the duration of an aircraft approach to landing. For H-ARAIM, even though the $I_{REQ,H}$ is specified per hour, the actual H-ARAIM operation period can be much longer. Therefore, we treat T_E as a arbitrary value, and express $I_{REQ,H}$ per T_E , i.e., $I_{REQ,H} = T_E \times 10^{-7} / T_E$. Comparing the upper bound of equation 6.5

with the requirement $T_E \times 10^{-7}$, the most stringent navigation criterion is obtained when $\frac{\beta}{T_E}$ is maximized, because $\frac{\beta}{T_E}$ is the relative multiplier of P_{HMI}^{sam} as a function of T_E . Therefore:

$$\max_{T_E} \left(\frac{\beta}{T_E} \right) = \max_{T_E} \left(\frac{N}{T_E} + \frac{N}{2 \cdot MTTA} \right) \quad (6.6a)$$

$$= \max_{T_E} \left(\frac{1}{T_A} + \frac{T_E}{2 \cdot MTTA \cdot T_A} \right) \quad (6.6b)$$

Equation 6.6b clearly shows that the longer the exposure time is, the larger β must be. According to Table 2.1, the TTA requirements (T_A) for V- and H-ARAIM are 6 sec and 10 sec. Using T_E of 1 hour as an example for H-ARAIM, the values of β for H- and V-ARAIM are respectively 540 and 30, which indicates that evaluating the integrity risk at one sample time epoch will lead to overly optimistic results.

It must be clarified that even though equation 6.5 safely bounds the actual integrity risk, the final conclusion may be overly conservative. To derive a simple upper bound of equation 6.3b, the HMI_{TTA}^μ events are treated as independent. Therefore, equation 6.4a bounds 6.3b by summing up all the HMI_{TTA} after the fault onset time t , i.e., assuming all the following-up TTAs are affected. However, most faults will presents a sustained HMI threat for multiple TTA intervals. Deriving a more realistic upper bound on P_{HMI}^{actual} requires characterizing the fault profile over time, and this research is considered in the future work.

6.2 Actual False Alarm Probability over the Exposure Time

This section addresses the impact of test statistic time correlation on FA, and derives the equations to evaluate the actual FA probability over the exposure time interval. Using similar notation as the last section, the one sample FA at time epoch

k is expressed as:

$$P_{FA}^{sam,k} < P(D_0^k | H_0) = P\left(\bigcup_{d=1}^h |q_d^k| > T_d | H_0\right) \quad (6.7)$$

Equation 6.7 represents the same probability as in the FA equations in Chapter 2, except the superscript ‘*sam, k*’ is employed here to distinguish it from the following FA expressions. In addition, the prior probability of FF state P_{H_0} is removed because it is very close to 1. Therefore, the right two terms in equation 6.7 is larger than $P_{FA}^{sam,k}$. Recall that q_d^k is the normalized FD test statistic (scalar) at time epoch k , and T_d is the corresponding detection threshold.

The actual FA probability over the exposure time should account for all possible detection events within the time interval. Therefore:

$$P_{FA}^{actual} < P\left(\bigcup_{k=1}^M D_0^k | H_0\right) = 1 - P\left(\bigcap_{k=1}^M \bar{D}_0^k | H_0\right) \quad (6.8)$$

Equation 6.8 can be upper bounded follows. The derivations of equation 6.9 are presented in Appendix B.

$$P_{FA}^{actual} < 1 - P(\bar{D}_0^k | H_0) \left\{ 1 - \frac{P(\bar{D}_0^k, D_0^{k-1} | H_0)}{P(\bar{D}_0^k | H_0)} \right\}^{M-1} \quad (6.9)$$

Due to the correlations among the FD test statistics, even an upper bound of equation 6.9 can not be easily evaluated. Rather, we obtain an upper bound by respectively lower bounding $P(\bar{D}_0^k | H_0)$ and upper bounding $P(\bar{D}_0^k, D_0^{k-1} | H_0)$, i.e.:

$$P(\bar{D}_0^k | H_0) = 1 - P(D_0 | H_0) = 1 - P\left(\bigcup_{d=1}^h |q_d| > T_d | H_0\right) \quad (6.10a)$$

$$> 1 - \sum_{d=1}^h P(|q_d| > T_d | H_0) \quad (6.10b)$$

and

$$P(\bar{D}_0^k, D_0^{k-1} | H_0) = P\left(\bigcap_{d=1}^h |q_d^k| < T_d, \bigcup_{d=1}^h |q_d^{k-1}| > T_d | H_0\right) \quad (6.11a)$$

$$= P\left(\bigcup_{d=1}^h (|q_d^k| < T_d, |q_d^{k-1}| > T_d) | H_0\right) \quad (6.11b)$$

$$< \sum_{d=1}^h P(|q_d^k| < T_d, |q_d^{k-1}| > T_d | H_0) \quad (6.11c)$$

Therefore, the upper bound of P_{HMI}^{actual} can be obtained by solving equations 6.10b and 6.11c, and then substituting into 6.9. The probability in equation 6.11c corresponds to the *level crossing problem* described by Papoulis in [47]. The *level* here is the normalized threshold T_d , and the solution can be derived by combining separate intermediate results on page 486 and 492 of [47]:

$$P(|q_d^k| < T_d, |q_d^{k-1}| > T_d | H_0) = \frac{1}{\pi} \exp\left(-\frac{T_d^2}{2}\right) \arccos\left[\frac{R_q(T_S)}{R_q(0)}\right] \quad (6.12)$$

where $R_d(t)$ denotes the autocorrelation function of the normalized FD test statistic q . This expression is accurate when $\frac{R_q(T_S)}{R_q(0)}$ is close to 1, which is true for all the auto-correlation analysis in this work. According to equations 2.19 and 2.40:

$$q_d^k = \frac{1}{\sigma_{\Delta_d}} \mathbf{S}_{\Delta_d}^{(r)} (\mathbf{v}^k + \mathbf{f}^k) \quad (6.13)$$

Therefore, $R_d(t)$ can be evaluated using the following equation, where $E\{\mathbf{v}^k \mathbf{v}^{k+t}\}$ is a diagonal matrix that is composed of the autocorrelation functions of each measurement error.

$$R_q(t) = \frac{1}{\sigma_{\Delta_d}^2} \mathbf{S}_{\Delta_d}^{(r)} E\{\mathbf{v}^k \mathbf{v}^{k+t}\} \mathbf{S}_{\Delta_d}^{(r)T} \quad (6.14)$$

6.3 Characterizing Time Correlation of Measurement Error

In order to evaluate equation 6.14, the time profile of the measurement error must be characterized. This section respectively derives the autocorrelation functions

for user error, tropospheric error and signal-in-space error. Because those functions will be used for FA evaluation, the derivations are in an average sense.

The ARAIM tropospheric error model specifies the standard deviation of zenith tropospheric delay σ_{ZTD} of 0.12 m [21]. And this number is multiplied by an obliquity factor $OB(\theta)$ to get the standard deviation of the tropospheric error σ_{tropo} :

$$\sigma_{tropo} = \sigma_{ZTD}OB(\theta) = 0.12 \frac{1.001}{\sqrt{0.002001 + \left(\sin\left(\frac{\pi\theta}{180}\right)\right)^2}} \quad (6.15)$$

In addition, [7] also points out that tropospheric error shall be modeled using a First-Order Gauss-Markov process with a 30 minute correlation time τ_{tropo} . Therefore, the autocorrelation function of the tropospheric error is:

$$R_{tropo}(t) = \sigma_{tropo}^2 e^{-|t|/\tau_{tropo}} \quad (6.16)$$

The airborne user error, which includes multipath and receiver noise, is characterized using flight data collected on a Boeing 787 aircraft. According to the code-minus-carrier results shown in Appendix C, it is suitable to apply an average zero-mean normal distribution with $\sigma_{user} = 0.38$ m for the raw user error, and an average time constant $\tau_{user} = 14$ sec. Given a carrier-smoothing time constant τ_{CSC} , the autocorrelation function of the carrier-smoothed-code $R_{user}(t)$ is also derived in Appendix C:

$$R_{user}(t) = \kappa \sigma_{user}^2 \frac{\tau_{user}}{\tau_{CSC}^2 - \tau_{user}^2} (\tau_{CSC} e^{-|t|/\tau_{CSC}} - \tau_{user} e^{-|t|/\tau_{user}}) \quad (6.17)$$

where κ is the iono-free scale factor:

$$\kappa \equiv \frac{f_{L1}^4 + f_{L5}^4}{(f_{L1}^2 - f_{L5}^2)^2} \quad (6.18)$$

For the GPS SV orbit/clock error, it is shown in [26] that σ_{URE} has been decreasing over the past 5 years. In 2017, the average σ_{URE} over all GPS satellites

was 0.5 m, so this value is applied in our analysis. Appendix D illustrates the time profile of the SV orbit/clock error, where a long time constant is observed. By linearly interpolating the lag times between 0 and 15 minutes, the following autocorrelation function is derived:

$$R_{SIS}(t) = 1 - \frac{1 - 0.945}{15 \times 60} t \quad (6.19)$$

6.4 Analytical Results

Using the theoretical methods established in section 6.2 and the error models described in section 6.3, this section analyzes the impact of test statistic time correlation on FA probability, by respectively evaluating $P_{FA}^{sam,k}$ and P_{FA}^{actual} . H-ARAIM is employed for this analysis since it has a longer exposure time T_E . The sample interval $T_S = 0.5$ sec is applied.

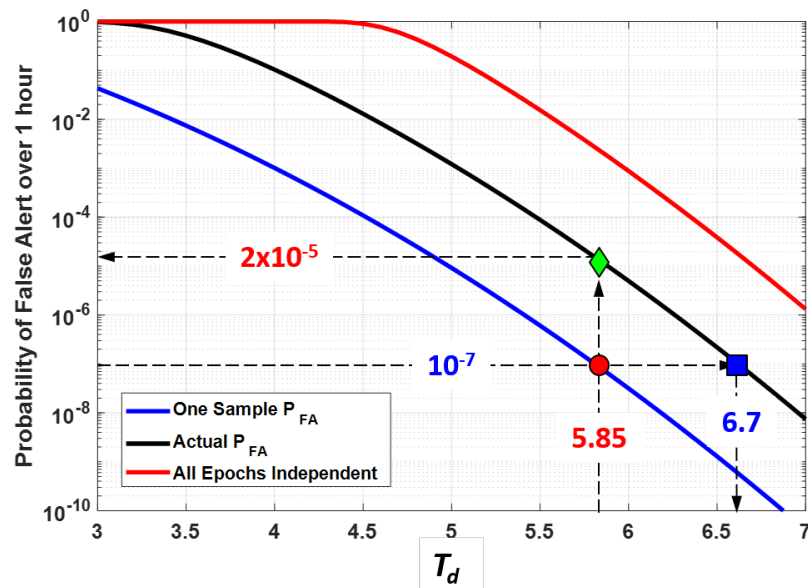


Figure 6.3. H-ARAIM P_{FA} over 1 hour.

In Figure 6.3, the blue line corresponds to the one sample P_{FA} , which is evaluated using equation 6.7. The black and red lines represent the actual P_{FA} that are computed by equation 6.9. These two lines are obtained by respectively

(a) applying the autocorrelation functions in section 6.3 and (b) assuming white measurement error. As shown in the figure, if the detection thresholds are set based on the FA requirement of 10^{-7} , the actual P_{FA} reaches 2×10^{-5} , which is more than two orders of magnitude higher than expected. To mitigate this impact, the detection threshold T_d needs to be increased from 5.85 to 6.7.

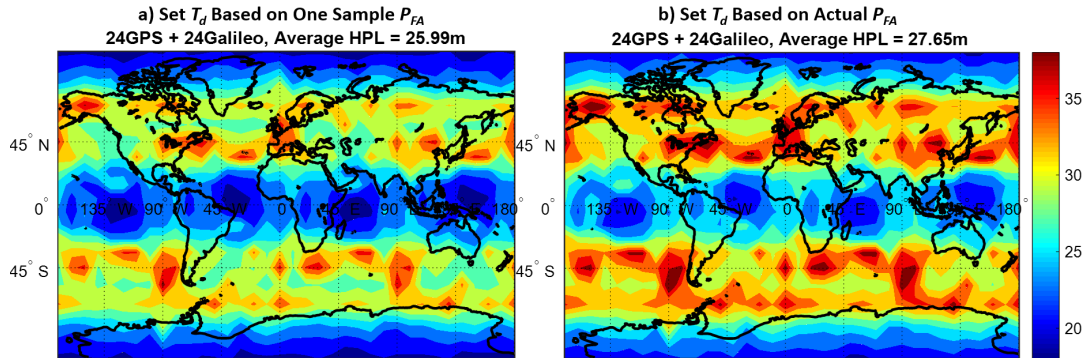


Figure 6.4. H-ARAIM HPL Maps by Increasing the Detection Threshold.

Figure 6.4 shows the H-ARAIM worldwide HPL maps evaluated by increasing the T_d to accommodate the corresponding FA requirement. The results are obtained under baseline simulation conditions listed in Table 2.3. The figure on the left is identical to figure 2.4, which corresponds to the one sample P_{FA} scenario. Figure 6.4b applies the conclusion of figure 6.3, i.e., it accounts for the impact of test statistic time correlation on FA probability. After increasing the detection threshold T_d , the same level of HPL is still maintained. In the mean time, the actual FA probability at the airborne user has been reduced to meet the requirement.

6.5 Experimental Results Using Collected Data

This section validates the analytical results on P_{FA} . The experimental FA probability is obtained by processing the GNSS observation data, which is collected using the ARAIM prototype built by the Navigation Laboratory at IIT [39]. Three days data were processed with a sample interval of 10 sec. With the measurements, the

test statistics q_d are evaluated at each time epoch, and the FA events are identified by comparing q_d with T_d . The FA probability is then computed by dividing the number of FA events with the total time period, i.e., 72 hours. Based on the definition of P_{FA} , multiple FAs within one hour interval are counted as one FA event. For example, if there are 4 detections over the 72 hours, the P_{FA} is (a) $\frac{4}{72}$ if those detections occur in different hours, and is (b) $\frac{1}{72}$ if those detections occur within the same hour.

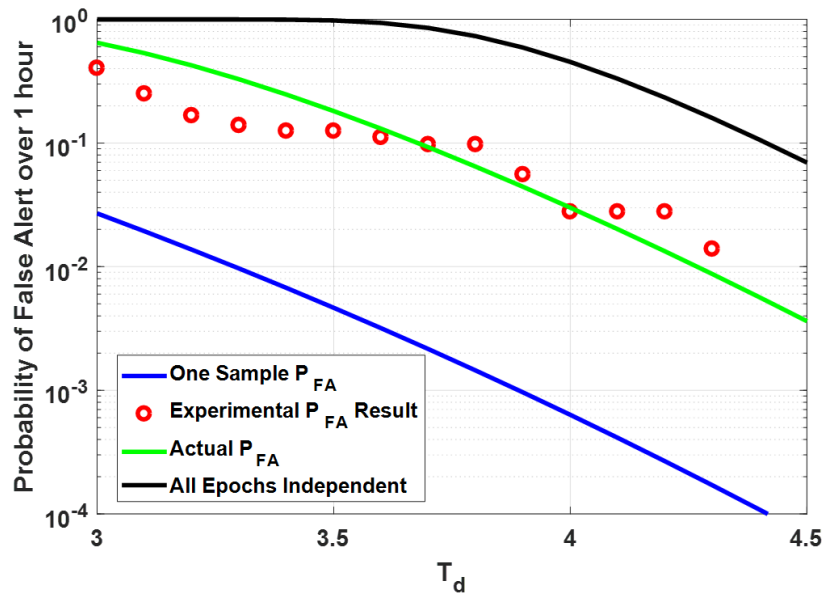


Figure 6.5. H-ARAIM FA Probability Evaluated Using Experimental Data.

Since the satellite orbit/clock and tropospheric errors are the same for both the airborne and ground GNSS receivers, the SIS and tropospheric error models derived in section 6.3 can be applied for the ARAIM prototype. However, the user error profile is highly dependent on the multipath environment and receiver quality. In particular, the time behavior shown in section 6.3 was established using flight data. But the prototype receiver used here is stationary, so the time constant of the user error is expected to be much longer than 14 sec. In response, a separate analysis is first carried out in Appendix E to characterize the multipath and receiver noise of this ARAIM prototype. Using a standard deviation of $\sigma_{user} = 0.6$ m and assuming the

time constant τ_{user} is 150 sec for this environment, the FA probability is evaluated and shown in Figure 6.5.

In comparison with the results of Figure 6.3, the predicted actual P_{FA} (green line) is larger in Figure 6.5. This is because of the different sample intervals T_S applied under these two scenarios. As expected, the experimental P_{FA} (red dots) decreases following the actual P_{FA} line. Moreover, the FA probabilities are far greater than the one sample P_{FA} result (blue line), which confirms our prior conclusions. Due to the limited time length for data collection, the resolution of the experimental result is restricted to $\frac{1}{72}$. It will be considered in future work to collect more data and redo this analysis. Nevertheless, Figure 6.5 still verifies that because of the time correlation of the test statistics, the actual FA probability is significantly larger than expected. This issue can be mitigated by increasing the detection thresholds.

CHAPTER 7

OFFLINE GROUND MONITOR TO VALIDATE ISM

Unlike the last four chapters, in which the contributions apply for the airborne user receiver, this chapter focuses on the ARAIM ground segment. A dedicated offline ground monitor is designed and analyzed to validate the ISM broadcast to the users. To achieve this, GNSS satellite orbits and clocks must be estimated. There are many sophisticated orbit determination processes such as the one used by the international GNSS service (IGS), whose performance is specified in terms of accuracy. In contrast, the proposed offline ARAIM architecture is mainly intended for safety-critical aviation applications, in which integrity is of the primary concern. This monitor employs a straightforward approach to estimate satellite orbit/clock, which aims at facilitating ISM generation and validation. It takes advantage of the existing SBAS ground infrastructure. A worldwide network of sparsely distributed reference stations is considered, and parametric satellite orbital models are employed in the estimators, whose derivation and implementation are described step by step. Two separate analyses, covariance analysis and model fidelity evaluation, are carried out to respectively assess the impact of measurement errors and of residual model errors on the monitors estimated orbit/clock.

7.1 Offline Monitor Concept and Required Performance

To validate the ISM, online and offline ARAIM architectures have been investigated [48, 20]. Offline architectures have generally been perceived as preferable because they do not require a real-time communication link between users and ground segment, and therefore eliminate the connectivity risk. An offline ARAIM monitor would rely on post-processed GNSS measurements to bound errors in the CSP broad-

cast navigation message on a long-term basis. To do this, prior research has taken truth satellite positions and clock biases from the IGS network [49, 26]. However, given that ARAIM is intended to operate over several decades, monitor dependence on external systems or organizations with little or no stake in civil aviation must be carefully considered, and ideally, avoided. Most importantly, ARAIM will serve safety critical applications, any potential safety risks must be properly accounted for and quantified. The IGS, the national geospatial intelligence agency (NGA), and others currently provide high-accuracy satellite orbit/clock products. But none of these agencies make specific commitments on the reliability of their products, or on the processes used to obtain those products. Further, data gaps exist in those products, especially during satellite fault events, which are crucial to ARAIM. In response, this work develops a new approach to define and validate ISM parameters by designing a dedicated ARAIM offline ground monitor architecture.

Using an offline monitor, the update rate of the ISM may vary from a month to year depending on the need. A large amount of data will be processed at the ground to obtain the ISM, which is expected to bound the SIS performance until the next update. To achieve this, differences between broadcast ephemeris and the monitors estimated satellite orbit/clock will be first evaluated over time, and then these will be used to validate (or modify, if needed) the ISM parameter values. In this chapter, b_{nom} and σ_{URA} will be mainly considered. Since the monitors orbit/clock estimation errors will directly contribute to the validated ISM, it is necessary to first define the required accuracy of the monitors orbit/clock estimator.

Equation 7.1 shows the relationship among the actual standard deviation of broadcast satellite orbit/clock error σ_{ACTUAL} (actual σ_{URA}), the standard deviation of the monitors estimated orbit/clock error $\sigma_{MONITOR}$, and the validated standard

deviation of the satellite orbit/clock error $\sigma_{VALIDATE}$ (validated σ_{URA}).

$$\sigma_{VALIDATE} = \sqrt{\sigma_{ACTUAL}^2 + \sigma_{MONITOR}^2} \quad (7.1)$$

Figure 7.1 plots $\sigma_{VALIDATE}$ versus $\sigma_{MONITOR}$ over different σ_{ACTUAL} values. For example, the figure shows that for $\sigma_{URA} = 2.4$ m, having $\sigma_{MONITOR}$ is less than 1.73 m is sufficient for validation. According to the most recent study on GPS SIS performance to support ARAIM, the maximum actual σ_{URA} is observed on space vehicle number (SVN) 61, where σ_{ACTUAL} is 1.65 m, and for most satellites it is much smaller [26]. The red curve is of most interest because it is expected future performance of the GPS constellation will provide σ_{ACTUAL} of 1 m, or less. And dual-constellation ARAIM availability simulations in Chapter 2 have revealed LPV-200 approach can only be supported when σ_{ACTUAL} of both constellations are approximately 1 m. The figure shows slow growth of $\sigma_{VALIDATE}$ as $\sigma_{MONITOR}$ increases. Even when $\sigma_{MONITOR}$ reaches half of σ_{ACTUAL} at the end of the curve, the achievable validated σ_{URA} is still around 1.1 m.

In addition to $\sigma_{MONITOR}$, the estimated satellite orbit/clock error may have a non-zero mean, denoted by $b_{MONITOR}$. This term is accounted as one component of the validated ISM parameter, b_{nom} . However, using baseline SS ARAIM user algorithm, as shown in equation 2.29, the absolute value of b_{nom} is additive for each measurement. This causes the integrity risk bound to become loose as the number of measurements increases, thereby degrading availability performance. Therefore, it is desirable to mitigate any contributions of $b_{MONITOR}$ to the validated b_{nom} .

From the analysis and discussion above, it can be seen that the required accuracy of the offline monitor is significantly lower than the precise satellite orbit/clock products by IGS or NGA. Instead, it is the reliability of the monitors estimator output that is key. In other words, even though the monitors satellite orbit/clock estimates

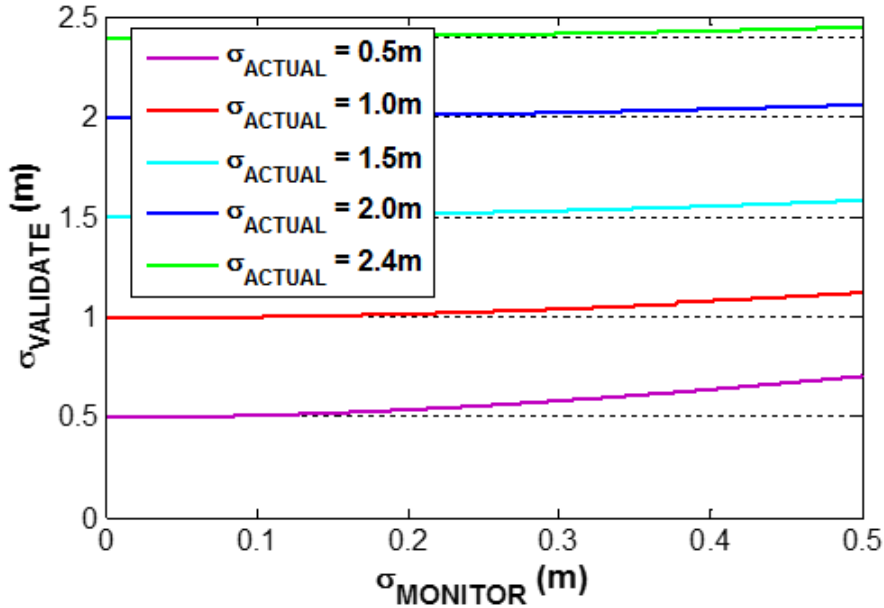


Figure 7.1. σ_{VALIDATE} vs. σ_{MONITOR} over Varying σ_{ACTUAL} Values.

may have larger errors, their stable performance and consistent availability enables ISM validation without missing data gaps. Therefore, in the estimator design it is not necessary to pursue a complicated orbit determination process. We can instead use the simple, transparent approach described in the next section.

7.2 Offline Monitor Architecture

This section describes the offline monitor architecture step-by-step. A network of worldwide sparsely distributed RS is employed to collect code and carrier measurements over time. In the selection of sites for the RS, we take advantage of the satellite based augmentation system (SBAS) ground infrastructures since they are already existing and are designed to support civil aviation applications. Figure 7.2 (left) shows all of the existing SBAS RS from different countries or regions, and Figure 7.2 (right) shows the network of 20 RS used in this work. To obtain a roughly uniform global distribution, five non-SBAS RS sites are added. This network ensures that each satellite can continuously be tracked by at least two reference stations,

but does not allow reverse positioning (four RS simultaneously observing a SV are required to directly estimate the satellite position). Instead, the offline monitor uses parametric orbit models to determine SV trajectories.

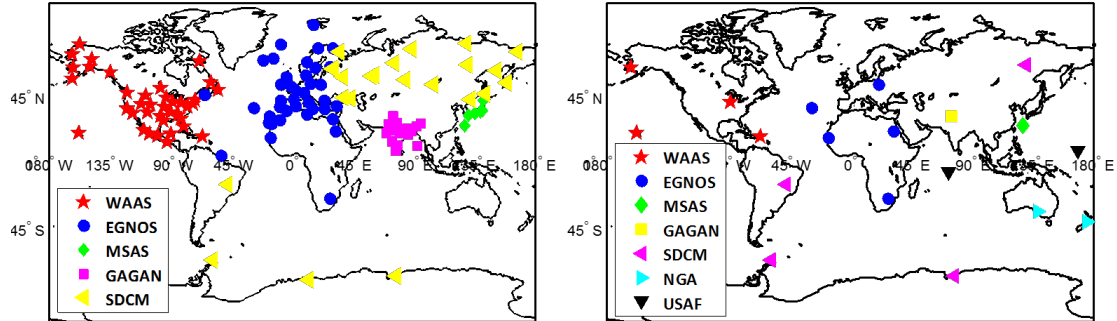


Figure 7.2. All Existing SBAS Stations (Left) and Example Network of 20 RS Used in This Work (Right) (Figure Courtesy of Dr. Michael Jamoom).

Two candidate GPS orbit models, legacy and CNAV, are investigated. Both models are valid for medium earth orbit (MEO) SVs, with 15 orbit parameters being used for the legacy GPS orbit model and 17 parameters for the newer CNAV model [50]. Throughout this thesis, it is assumed no satellite maneuvers occur, because the orbit models will not be valid while the spacecraft is thrusting. Maneuvers occur rarely, and they can be handled by simply initiating a new estimator after the maneuver. However, these details of practical implementation are beyond the scope of this work and will not be considered further.

Let \mathbf{p}_i^{orb} be the 15×1 (or 17×1 , depending on which orbit model is used) vector of orbit model parameters for SV i , and let $\mathbf{g}_{orb,k}$ be the non-linear function that determines SV orbit from these parameters. The true SV position $\mathbf{x}_{i,k}$ of SV i at time epoch k can be expressed as:

$$\mathbf{x}_{i,k} = \mathbf{g}_{orb,k}(\mathbf{p}_i^{orb}) + \boldsymbol{\nu}_{i,k}^{orb} \quad (7.2)$$

where $\boldsymbol{\nu}_{i,k}^{orb}$ is the deviation of the model output from the true satellite position $\mathbf{x}_{i,k}$. $\boldsymbol{\nu}_{i,k}^{orb}$ represents the models inability to perfectly capture the true orbit, and this will

be further analyzed in later sections. The GPS orbit model is valid over a four-to-six-hour time interval noted T_{FIT} [50]. Sensitivity to T_{FIT} has been evaluated in [51]. A four-hour fitting interval, which is the most common value for GPS ephemeris, will be used in this work.

Both RS and SV are equipped with atomic clocks, and a quadratic polynomial is usually employed to model their nominal errors over four hours. However, most SV faults are caused by their clocks, and for the monitor to clearly observe them, no assumption can be made on the SV clock dynamics. As for the RS, whose clock faults can be detected at the ground, it is feasible to apply quadratic clock model. To assess the potential benefit of using such a model for the RS clocks, we analyze two cases: (a) applying a quadratic polynomial to model RS clock errors, and (b) making no assumption on RS clocks, (i.e., punctually estimating RS clock states). Under scenario (a), let $b_{j,k}$ be the clock bias of RS j at time k ; it can be modeled as:

$$b_{j,k} = g_{clk,k}(\mathbf{p}_j^{clk}) + \nu_{j,k}^{clk} \quad (7.3)$$

Similar to equation 7.2, \mathbf{p}_j^{clk} in equation 7.3 is the 3×1 vector of clock parameters including α_{f0}^j , α_{f1}^j , α_{f2}^j [50], and $\nu_{j,k}^{clk}$ is the clock model error. $g_{clk,k}(\mathbf{p}_j^{clk})$ is a linear function (in the clock parameters) that can be expressed as:

$$g_{clk,k}(\mathbf{p}_j^{clk}) = \alpha_{f0}^j + \alpha_{f1}^j (t_k - t_{ref}) + \alpha_{f2}^j (t_k - t_{ref})^2 \quad (7.4)$$

where t_k and t_{ref} are respectively the true time and a specific reference time.

Dual-frequency, ionosphere-free code and carrier measurements for SV i , from RS j , at time epoch k , are expressed by the following two equations:

$${}^{i,j}\rho_k = \|\mathbf{x}_j - \mathbf{x}_{i,k}\| - \tau_{i,k} + b_{j,k} + {}^{i,j}\varepsilon_{tropo,k} + {}^{i,j}\varepsilon_{RNM,\rho,k} \quad (7.5)$$

$${}^{i,j}\phi_k = \|\mathbf{x}_j - \mathbf{x}_{i,k}\| - \tau_{i,k} + b_{j,k} + {}^{i,j}\eta + {}^{i,j}\varepsilon_{tropo,k} + {}^{i,j}\varepsilon_{RNM,\phi,k} \quad (7.6)$$

where \mathbf{x}_j denotes the known location of RS j in an Earth-Centered Earth-Fixed (ECEF) reference frame. $\mathbf{x}_{i,k}$ is the unknown location of SV i at time k . $\tau_{i,k}$ and $b_{j,k}$ are respectively the unknown clock offsets of SV i and RS j at time k . ${}^{i,j}\eta$ is the carrier phase cycle ambiguity for SV i at RS j . $\|\bullet\|$ denotes the Euclidean norm operator, which provides the distance between RS j and SV i in this case.

The error terms in equations 7.5 and 7.6 account for residual tropospheric delay noted ${}^{i,j}\varepsilon_{tropo,k}$, and receiver noise and multipath (RNM) errors denoted by ${}^{i,j}\varepsilon_{RNM,\rho,k}$ for code and ${}^{i,j}\varepsilon_{RNM,\phi,k}$ for carrier. It is assumed that the standard deviations of the raw code and carrier measurement RNM error hold typically values of 0.5 m and 0.01 m, respectively. These standard deviations are multiplied by 2.588 to account for the ionosphere-free combination at L1 and L5 frequencies. To account for the temporal and spatial correlation of zenith tropospheric deal (ZTD), a first order Gauss-Markov process with a two-hour correlation time is applied. Assuming the RS have access to data from weather stations, the value of 0.05 m is used as the standard deviation of residual ZTD. This value is scaled for lower elevation satellites using the tropospheric mapping function given in equation 6.15.

To estimate the SV orbit parameters and clocks, the measurement equations 7.5 and 7.6 and the orbit/clock model equations 7.2 and 7.3 need to be linearized and incorporated into one filter. For illustrative purposes, only code measurements will be shown in the following derivations. Equation 7.5 is first linearized at $\mathbf{x}_{i,k}^*$:

$${}^{i,j}\delta\rho_k = {}^{i,j}\mathbf{e}_k^T \boldsymbol{\delta}\mathbf{x}_{i,k} - \tau_{i,k} + b_{j,k} + {}^{i,j}\varepsilon_{\rho,k} \quad (7.7)$$

where $\boldsymbol{\delta}$ denotes the deviation from nominal values, e.g., $\boldsymbol{\delta}\mathbf{x}_{i,k} = \mathbf{x}_{i,k} - \mathbf{x}_{i,k}^*$. ${}^{i,j}\mathbf{e}_k$ is the 3×1 line of sight (LOS) vector between SV i and RS j at time k in ECEF. ${}^{i,j}\varepsilon_{\rho,k}$ denotes the code measurement error, including ${}^{i,j}\varepsilon_{tropo,k}$ and ${}^{i,j}\varepsilon_{RNM,\rho,k}$.

In the next step, the orbit model is linearized at ${}^*\mathbf{p}_i^{orb}$ where $\mathbf{x}_{i,k}^* = \mathbf{g}_{orb,k}({}^*\mathbf{p}_i^{orb})$.

Substituting the linearized orbit model equation and the clock error model equation 7.4 into the code measurement, equation 7.7 becomes:

$${}^{i,j}\delta\rho_k = {}^{i,j}\mathbf{e}_k^T \mathbf{A}_{i,k}^{orb} \delta\mathbf{p}_i^{orb} - \tau_{i,k} + b_{j,k} + {}^{i,j}\varepsilon_{\rho,k} \quad (7.8)$$

where $\mathbf{A}_{i,k}^{orb}$ is the Jacobian matrix for the SV orbit model in equation 7.2, which is 3×15 for the GPS legacy orbit model and 3×17 for the CNAV model. It is composed of numerically-derived partial derivatives of the position coordinates of SV i at time k ($\mathbf{x}_{i,k} = [x_{i,k} \ y_{i,k} \ z_{i,k}]^T$) with respect to the orbit parameters $\mathbf{p}_i^{orb} = [p_1 \ \cdots \ p_{15}]^T$:

$$\mathbf{A}_{i,k}^{orb} = \begin{bmatrix} \frac{\partial x_{i,k}}{\partial p_1} & \frac{\partial y_{i,k}}{\partial p_1} & \frac{\partial z_{i,k}}{\partial p_1} \\ \vdots & \vdots & \vdots \\ \frac{\partial x_{i,k}}{\partial p_{15}} & \frac{\partial y_{i,k}}{\partial p_{15}} & \frac{\partial z_{i,k}}{\partial p_{15}} \end{bmatrix}^T \quad (7.9)$$

and $\mathbf{A}_{j,k}^{clk}$ is a 1×3 vector that expresses equation 7.4 in a more compact form:

$$\mathbf{A}_{j,k}^{clk} = [1 \ (t_k - t_{ref}) \ (t_k - t_{ref})^2]^T.$$

7.3 Estimator Design

Once the linearized single measurement equation 7.8 is derived, the estimator can be defined. The parameters to be estimated (states) include SV orbit parameters $\delta\mathbf{p}_i^{orb}$, SV clock $\tau_{i,k}$, RS clock model parameters \mathbf{p}_i^{clk} , and cycle ambiguities ${}^{i,j}\eta$. All of these states can be simultaneously estimated using either a *batch* or *Kalman filter* implementation. The batch estimator is presented in this section, and the alternative Kalman Filter approach is provided in Appendix F. The states are estimated over T_{FIT} of 4 hours, using a 4 min sample period to avoid modelling correlation between samples due to RS multipath. In addition, to obtain observability, all the clock error states, including both SV and RS clocks, are measured with respect the clock of RS 1.

The batch estimator is established by stacking all code and carrier measurements over the fit interval T_{FIT} . Measurements for all SVs from 1 to I are collected by all RS from 1 to J , at all time epochs from 1 to K . The resulting observation equation is written as:

$$\begin{bmatrix} {}^{1,1}\delta\rho_K \\ {}^{1,2}\delta\rho_K \\ \vdots \\ {}^{1,J}\delta\rho_K \\ \vdots \\ {}^{i,j}\delta\rho_K \\ \vdots \\ {}^{I,J}\delta\rho_K \\ {}^{1,1}\delta\phi_K \\ \vdots \\ {}^{I,J}\delta\phi_K \end{bmatrix} = \begin{bmatrix} {}^{1,1}\mathbf{B}_K & \mathbf{0}_{K \times 15} \cdots \mathbf{0}_{K \times 15} & \mathbf{I}_{K \times K} & \mathbf{0}_{K \times K} \cdots \mathbf{0}_{K \times K} & \mathbf{0}_{K \times 3} & \cdots & \mathbf{0}_{K \times 3} & \mathbf{0}_{K \times 1} & \cdots & \mathbf{0}_{K \times 1} \\ {}^{1,2}\mathbf{B}_K & \mathbf{0}_{K \times 15} \cdots \mathbf{0}_{K \times 15} & \mathbf{I}_{K \times K} & \mathbf{0}_{K \times K} \cdots \mathbf{0}_{K \times K} & \mathbf{A}_{2,K}^{cl} & \cdots & \mathbf{0}_{K \times 3} & \mathbf{0}_{K \times 1} & \cdots & \mathbf{0}_{K \times 1} \\ \vdots & \vdots & \ddots & \vdots & \ddots & \ddots & \vdots & \vdots & \ddots & \vdots \\ {}^{1,J}\mathbf{B}_K & \mathbf{0}_{K \times 15} \cdots \mathbf{0}_{K \times 15} & \mathbf{I}_{K \times K} & \mathbf{0}_{K \times K} \cdots \mathbf{0}_{K \times K} & \mathbf{0}_{K \times 3} & \cdots & \mathbf{A}_{J,K}^{cl} & \mathbf{0}_{K \times 1} & \cdots & \mathbf{0}_{K \times 1} \\ \vdots & \vdots & \ddots & \vdots & \ddots & \ddots & \vdots & \vdots & \ddots & \vdots \\ {}^{i,j}\delta\rho_K & \mathbf{0}_{K \times 15} & {}^{i,j}\mathbf{B}_K \cdots \mathbf{0}_{K \times 15} & \mathbf{0}_{K \times K} & \mathbf{I}_{K \times K} \cdots \mathbf{0}_{K \times K} & \mathbf{0}_{K \times 3} & \mathbf{A}_{j,K}^{cl} \cdots \mathbf{0}_{K \times 3} & \mathbf{0}_{K \times 1} & \cdots & \mathbf{0}_{K \times 1} \\ \vdots & \vdots & \ddots & \vdots & \ddots & \vdots & \ddots & \vdots & \ddots & \vdots \\ {}^{I,J}\delta\rho_K & \mathbf{0}_{K \times 15} \cdots \mathbf{0}_{K \times 15} & {}^{I,J}\mathbf{B}_K & \mathbf{0}_{K \times K} \cdots \mathbf{0}_{K \times K} & \mathbf{I}_{K \times K} & \mathbf{0}_{K \times 3} \cdots \mathbf{0}_{K \times 3} & \mathbf{A}_{J,K}^{cl} & \mathbf{0}_{K \times 1} & \cdots & \mathbf{0}_{K \times 1} \\ {}^{1,1}\delta\phi_K & {}^{1,1}\mathbf{B}_K & \mathbf{0}_{K \times 15} \cdots \mathbf{0}_{K \times 15} & \mathbf{I}_{K \times K} & \mathbf{0}_{K \times K} \cdots \mathbf{0}_{K \times K} & \mathbf{0}_{K \times 3} & \cdots & \mathbf{0}_{K \times 3} & \mathbf{1}_{K \times 1} & \cdots & \mathbf{0}_{K \times 1} \\ \vdots & \vdots & \ddots & \vdots & \ddots & \vdots & \ddots & \vdots & \vdots & \ddots & \vdots \\ {}^{I,J}\delta\phi_K & \mathbf{0}_{K \times 15} \cdots \mathbf{0}_{K \times 15} & {}^{I,J}\mathbf{B}_K & \mathbf{0}_{K \times K} \cdots \mathbf{0}_{K \times K} & \mathbf{I}_{K \times K} & \mathbf{0}_{K \times 3} \cdots \mathbf{0}_{K \times 3} & \mathbf{A}_{j,K}^{cl} & \mathbf{0}_{K \times 1} & \cdots & \mathbf{1}_{K \times 1} \end{bmatrix} \begin{bmatrix} \delta\mathbf{p}_1^{orb} \\ \vdots \\ \delta\mathbf{p}_I^{orb} \\ \hline \tau_{1,K} \\ \vdots \\ \tau_{I,K} \\ \hline \mathbf{p}_2^{cl} \\ \vdots \\ \mathbf{p}_J^{cl} \\ \hline {}^{1,1}\eta \\ \vdots \\ {}^{I,J}\eta \end{bmatrix} + \begin{bmatrix} {}^{1,1}\boldsymbol{\varepsilon}_{\rho,K} \\ {}^{1,2}\boldsymbol{\varepsilon}_{\rho,K} \\ \vdots \\ {}^{1,J}\boldsymbol{\varepsilon}_{\rho,K} \\ \vdots \\ {}^{i,j}\boldsymbol{\varepsilon}_{\rho,K} \\ \vdots \\ {}^{I,J}\boldsymbol{\varepsilon}_{\rho,K} \\ \hline {}^{1,1}\boldsymbol{\varepsilon}_{\phi,K} \\ \vdots \\ {}^{I,J}\boldsymbol{\varepsilon}_{\phi,K} \end{bmatrix} \quad (7.10)$$

In equation 7.10, four groups of states are distinguished by the dashed thin lines. The notations are worth clarifying: $\mathbf{0}_{a \times b}$ is an $a \times b$ matrix of zeros, $\mathbf{1}_{a \times b}$ is an $a \times b$ matrix of ones, and $\mathbf{I}_{a \times a}$ is an $a \times a$ identity matrix. In addition, the product of LOS vector and Jacobian matrix in equation 7.8 is defined as ${}^{i,j}\mathbf{B}_k$, i.e., ${}^{i,j}\mathbf{B}_k = {}^{i,j}\mathbf{e}_k^T \mathbf{A}_{i,k}^{orb}$. Since measurements at all time epochs are incorporated in equation 7.10, capital ‘ K ’ is used to denote the time sequence. Therefore,

$${}^{i,j}\delta\rho_K = \begin{bmatrix} {}^{i,j}\delta\rho_1 \\ \vdots \\ {}^{i,j}\delta\rho_K \end{bmatrix}, \quad {}^{i,j}\mathbf{B}_K = \begin{bmatrix} {}^{i,j}\mathbf{B}_1 \\ \vdots \\ {}^{i,j}\mathbf{B}_K \end{bmatrix}, \quad \boldsymbol{\tau}_{i,K} = \begin{bmatrix} \tau_{i,1} \\ \vdots \\ \tau_{i,K} \end{bmatrix} \quad \text{and} \quad {}^{i,j}\boldsymbol{\varepsilon}_{\rho,K} = \begin{bmatrix} {}^{i,j}\boldsymbol{\varepsilon}_{\rho,1} \\ \vdots \\ {}^{i,j}\boldsymbol{\varepsilon}_{\rho,K} \end{bmatrix} \quad (7.11)$$

It is obvious from equation 7.10 that this equation is very large due to the

substantial number of measurements in the fit interval.

It is also important to note that not all SVs will be visible to all RS during the fitting interval. To lighten the notations, these cases are not explicitly expressed in equations 7.10 and 7.11. But the corresponding rows must be removed whenever the measurements are unavailable.

To simplify equation 7.10, let \mathbf{z} , \mathbf{H} , \mathbf{s} , and $\boldsymbol{\varepsilon}$ be respectively defined as the measurement vector, observation matrix, state vector, and error vector. Then equation 7.10 becomes $\mathbf{z} = \mathbf{H}\mathbf{s} + \boldsymbol{\varepsilon}$, and the states can be evaluated using the LS estimator from Chapter 2:

$$\hat{\mathbf{s}} = (\mathbf{H}^T \mathbf{V}^{-1} \mathbf{H})^{-1} \mathbf{H}^T \mathbf{V}^{-1} \mathbf{z} \quad (7.12)$$

where \mathbf{V} is the covariance matrix of the measurement error vector $\boldsymbol{\varepsilon}$. The SV orbit parameters $\delta \mathbf{p}_i^{orb}$ and clock $\tau_{i,k}$ can be extracted from the full-state estimate vector $\hat{\mathbf{s}}$. Then, the estimated SV positions are obtained by substituting the estimated orbit model parameters into equation 7.2.

At this point, the offline monitors orbit and clock estimator has been fully established, and the estimation process has been described in detail. The derivations were done for the case where the legacy orbit model is applied and RS clock errors are modeled using a quadratic polynomial. For cases when the CNAV orbit model is used or RS clocks are not modeled, the expression of equation 7.10 needs to be modified to accommodate the corresponding scenario.

There will be two error sources contributing the monitors SV orbit/clock estimation error: (a) measurement error and (b) residual model error. To respectively quantify their impacts on the monitors performance, two separate analyses are carried

out in the following section: covariance analysis and model fidelity analysis.

7.4 Monitor Performance Analysis

7.4.1 Covariance Analysis. Covariance analysis is employed to investigate the contribution of measurement error on $\sigma_{MONITOR}$. According to equation 7.10, the covariance matrix of the full-state vector \mathbf{s} can be computed by:

$$\mathbf{\Sigma} = (\mathbf{H}^T \mathbf{V}^{-1} \mathbf{H})^{-1} \quad (7.13)$$

To evaluate the position and clock estimate error covariance of SV i at time epoch k , we first build the covariance matrix of the SV orbit parameters and clock $\mathbf{D}_{i,k}$, by extracting the corresponding elements from $\mathbf{\Sigma}$. Therefore, $\mathbf{D}_{i,k}$ is 16×16 if a legacy orbit model is employed. Then, the 4×4 covariance matrix $\mathbf{P}_{LL,i,k}$ of satellite position and clock in the local-level (LL) reference frame (along-track, cross-track, radial) can be evaluated by:

$$\mathbf{P}_{LL,i,k} = \begin{bmatrix} \mathbf{R}_{LL,i,k} & 0 \\ 0 & 1 \end{bmatrix} \mathbf{C}_{i,k} \mathbf{D}_{i,k} \mathbf{C}_{i,k}^T \begin{bmatrix} \mathbf{R}_{LL,i,k} & 0 \\ 0 & 1 \end{bmatrix}^T \quad (7.14)$$

where $\mathbf{R}_{LL,i,k}$ is the ECEF to LL rotation matrix, and $\mathbf{C}_{i,k}$ is defined as:

$$\mathbf{C}_{i,k} = \begin{bmatrix} \mathbf{A}_{i,k}^{orb} & 0 \\ 0 & 1 \end{bmatrix} \quad (7.15)$$

To investigate the SIS in range domain, we evaluate the maximum SISRE standard deviation at the worst-case user location. This is achieved by projecting $\mathbf{P}_{LL,i,k}$ along LOS for all locations within SV footprint [27]. And the worst-case SISRE standard deviation $\sigma_{SISRE,i,k}$ is defined as the maximum projection. In Figure 7.3, the projection region is shaded in light blue, and the black dashed line is one

example projection line $\mathbf{G}_{i,m}$, where m is the index of the lines. Therefore, $\sigma_{SISRE,i,k}^2$ is evaluated by:

$$\sigma_{SISRE,i,k}^2 = \max_{m=1,\dots,ALL} (\mathbf{G}_{i,m} \mathbf{P}_{LL,i,k} \mathbf{G}_{i,m}^T) \quad (7.16)$$

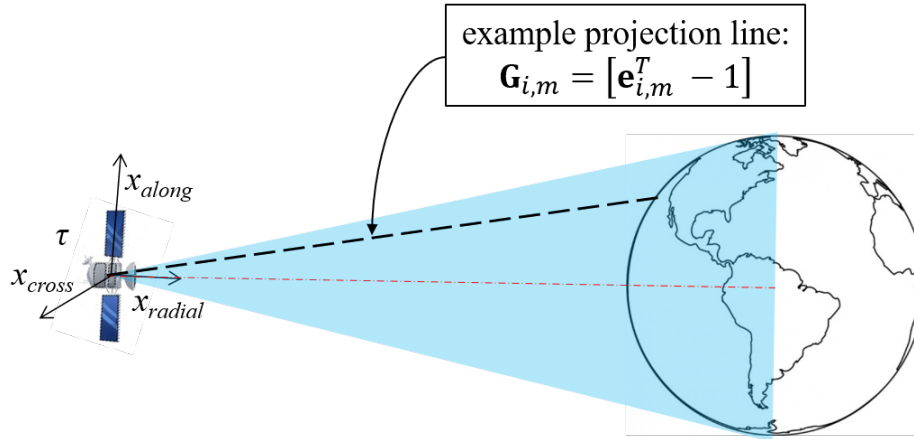


Figure 7.3. Covariance Matrix Projections along LOS for All Locations.

To explore the potential benefits of employing orbit/clock models to the estimation process, the covariance analyses are performed under 4 scenarios:

- CASE 1: legacy orbit model, quadratic RS clock model
- CASE 2: legacy orbit model, free RS clock states
- CASE 3: CNAV orbit model, quadratic RS clock model
- CASE 4: CNAV orbit model, free RS clock states

In the analyses, the measurements over a fitting interval T_{FIT} are taken as one data set, with each data set starting at regular one-hour intervals over a day. SV positions are computed from the GPS almanac also downloaded from [21].

Figure 7.4 shows standard deviation profiles of an example satellite (PRN 5) over one fitting interval. Three light blue lines are the orbit error deviations in the

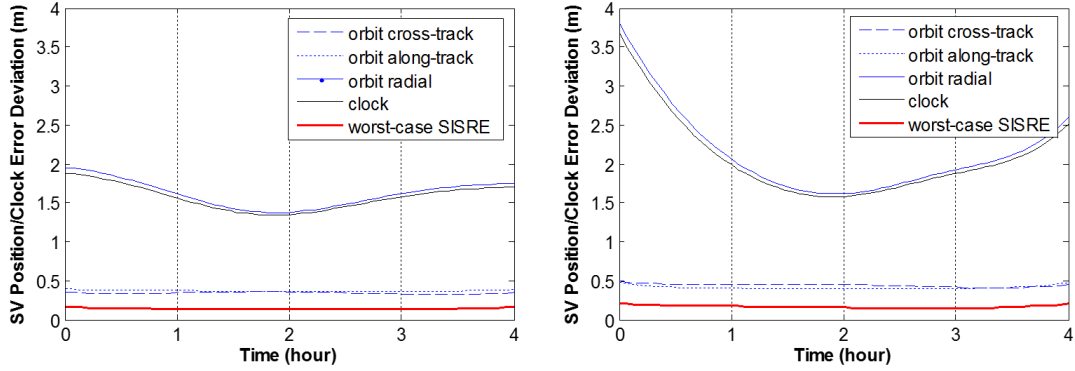


Figure 7.4. Example Profiles of Error Deviations along One Fitting Interval for Case 1 (Left) and Case 4 (Right).

along-track, cross-track, and radial directions. The black thin lines represent the satellite clock error deviation. The red thick lines are of greatest interest because they show the worst-case SISRE standard deviation, evaluated using equation 7.16. In both cases shown in the Figure 7.4, the orbit radial and clock components are highly correlated, which results in significantly smaller σ_{SISRE} than each individual term. Comparing the two figures, even though the orbit radial and clock terms are increased for case 4, there is no noticeable difference between the two red lines. The central two-hour values are taken as the final results of each fitting interval. Therefore, only the data between Hour 1 and Hour 3 in Figure 7.4 will be considered.

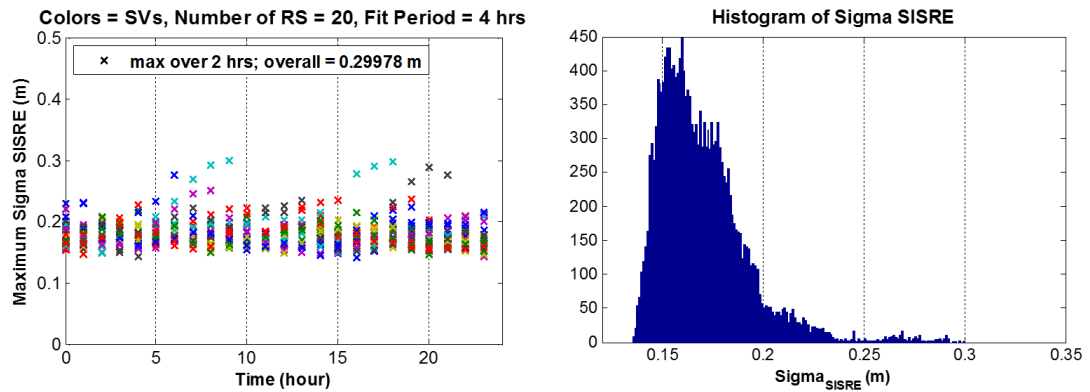


Figure 7.5. Maximum σ_{SISRE} over One Day (Left) and Their Distribution (Right) for Case 4.

The left plot of Figure 7.5 shows the maximum σ_{SISRE} profiles over a one-day period. Each column represents the largest σ_{SISRE} values of that fitting interval, and satellites are distinguished by different colors. The distribution of σ_{SISRE} is captured by the histogram on the right, which shows that a large majority σ_{SISRE} values are well below 0.25 m, and the maximum σ_{SISRE} is 0.3 m.

Table 7.1. Maximum σ_{SISRE} Values under Four Scenarios

	Quadratic Model for RS Clock	Free RS Clock
Legacy Orbit Model	CASE 1: 0.277 m	CASE 2: 0.287 m
CNAV Orbit Model	CASE 3: 0.283 m	CASE 4: 0.300 m

Table 7.1 summarizes the covariance analysis results by presenting the maximum σ_{SISRE} values of the four cases. At the first sight of this table, it can be observed that there are only small variations among the values. So, from the perspective of mitigating the contribution of measurement error on $\sigma_{MONITOR}$, no significant benefit is obtained by using different orbit/clock models. As expected, case 4 results in the largest σ_{SISRE} because it has the largest number of unknown parameters to be estimated. Based on these results, we recommend not using a quadratic model for RS clock error since there is little benefit from it, and not using it simplifies the estimator and allows for seamless performance in the event of an RS clock fault (because clock errors are estimated at each epoch individually). Therefore, cases 1 and 3 are no longer investigated, and only the impact of the orbit model error on the monitors performance will be addressed.

7.4.2 Orbit Model Fidelity Analysis. In this subsection, the residual model error is evaluated for two candidate orbit models: legacy and CNAV. To do this, precise GPS orbit data is first fed as measurements into equation 7.2, and then the orbit parameters \mathbf{p}_i^{orb} are estimated using a non-linear least squares algorithm [53].

IGS data \mathbf{x}^{IGS} is employed as the truth orbit, and the CSP broadcast ephemeris $\bar{\mathbf{p}}_i^{orb}$ parameter vector was used as the initial guess in the estimation process. Once \mathbf{p}_i^{orb} is estimated the residual error can be computed by subtracting \mathbf{x}^{IGS} with the models output. Therefore, for SV i at time epoch k , the ECEF residual is:

$$\mathbf{r}_{i,k} = \mathbf{x}_{i,k}^{IGS} - \mathbf{g}_{orb,k}(\hat{\mathbf{p}}_i^{orb}) \quad (7.17)$$

where $\hat{\mathbf{p}}_i^{orb}$ is the estimated orbit parameter vector. Finally, $\mathbf{r}_{i,k}$ can be expressed in the LL frame as:

$$\mathbf{r}_{LL,i,k} = \mathbf{R}_{LL,i,k}\mathbf{r}_{i,k} = [r_{A,i,k} \ r_{C,i,k} \ r_{R,i,k}] \quad (7.18)$$

In equation 7.18, the three components of the last vector represent the residual error in three dimensions: along-track, cross-track, and radial. To evaluate the ranging error from $\mathbf{r}_{LL,i,k}$, multiple analytical expressions can be found in the literature [29, 49, 5, 54]. In this work, the following equation is considered for orbit-only SISRE:

$$r_{SISRE,i,k} = 0.98r_{R,i,k} + 0.24sgn(r_{R,i,k})\sqrt{r_{A,i,k}^2 + r_{C,i,k}^2} \quad (7.19)$$

Equation 7.19 is very similar to the one in [5], except the SV clock term is removed. The derivation can be found in the reference and will not be restated here.

This analysis utilizes IGS data of the first month of 2016, i.e., 01/01/2016 - 01/31/2016. Similar to the covariance analysis, the data is fit to the model over T_{FIT} of 4 hours, and each fitting interval starts at 2 hours over a day. The sample period is 15 mins, and only the 2-hour central results are recorded.

Figure 7.6 shows the residual SISRE error for an example SV (PRN 5) on 01/06/2016. In each individual figure, the color-code helps distinguish fit intervals. Vertical t_{oe} -lines indicate the time of ephemeris, which is at the center of each 2-hour window. The results show that the residual SISRE of CNAV orbit model is significantly smaller than that of legacy orbit model.

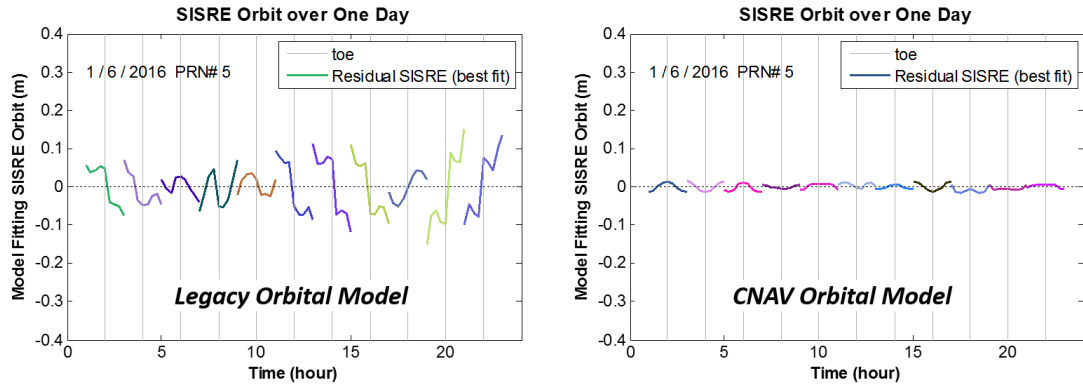


Figure 7.6. Best Fit Residual SISRE Orbit over One Day.

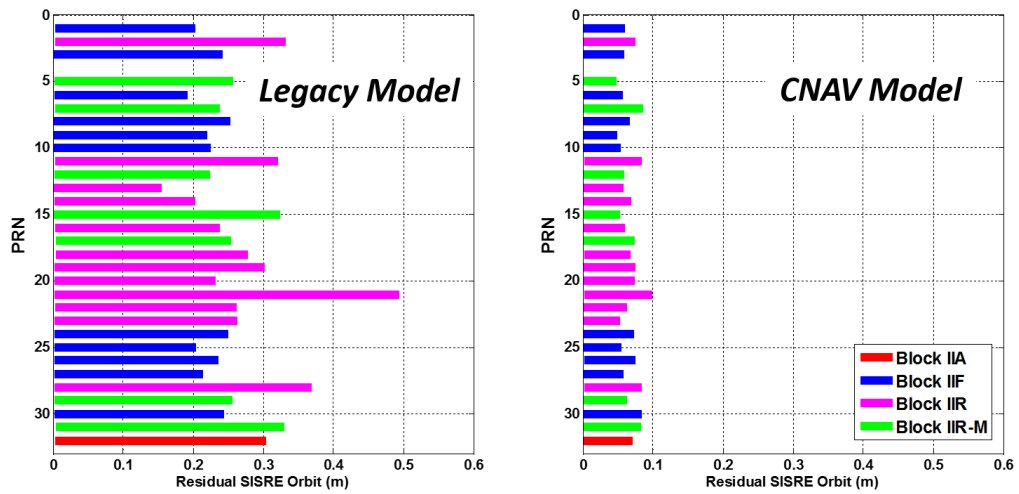


Figure 7.7. Residual SISRE Orbit Ranges.

Figures 7.7 and 7.8 provide a more general view of the residual SISRE profile by processing all of the IGS data. The SISRE ranges in Figure 7.7 are expressed in terms of GPS SV blocks. Using the GPS legacy orbit model, the maximum SISRE is 0.5 m and SISRE root-mean-square (RMS) is 0.089 m. These two values are respectively reduced to 0.1 m and 0.022 m with the CNAV model. In Figure 7.8, the data is overbounded using a Gaussian distribution with mean at b_{ob} and standard deviation of σ_{ob} . By comparing the two orbit models, it can be observed that employing the CNAV model will dramatically reduce the residual error. The CNAV model fidelity error can

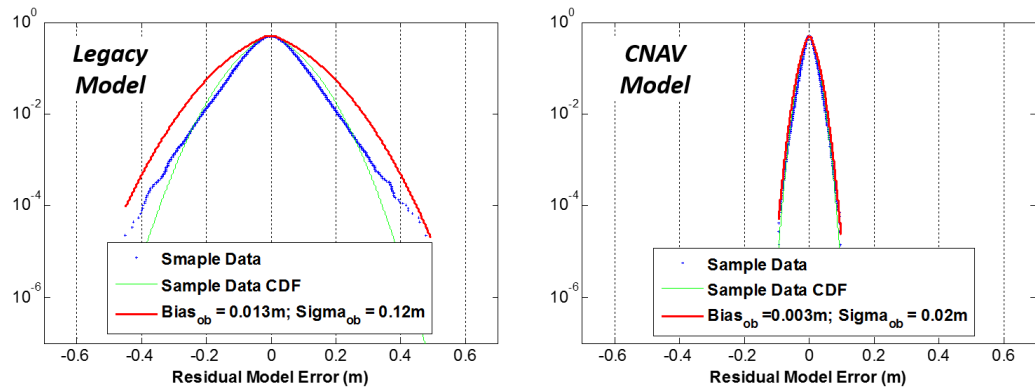


Figure 7.8. Residual SISRE Orbit Overbound.

be quantified using a Gaussian bound with approximately zero-mean, 2 cm standard deviation, which does not cause a significant contribution to the monitors orbit/clock error. Given that contribution of CNAV model error is negligible compared to the effect of measurement error shown in Table 7.1, and that the same is not true for the legacy model, it is recommended to use the CNAV orbit model for the ARAIM offline monitors orbit estimator.

CHAPTER 8

CONCLUSION

GNSS has been foreseen to have the capability of independently supporting aircraft navigation from takeoff, through en-route flight and final approach to landing. To achieve this goal, the most significant technical challenges are ensuring navigation integrity and continuity. Future multi-constellation GNSS will provide dramatically increased measurement redundancy and reduced measurement error, which opens the possibility of resolving these issues by leveraging the existing RAIM concept. Therefore, this dissertation comprehensively develops new ARAIM architecture including both airborne user algorithm and ground monitor.

8.1 ARAIM Navigation Performance

While ARAIM fault detection function ensures navigation integrity, fault exclusion function may be needed to improve continuity. According to the theoretical basis established in this thesis, an airborne H-ARAIM exclusion function is always required, whereas V-ARAIM exclusion is likely needed only if four constellations are applied or/and the constellations are subject to large fault probabilities. The analyses on the V-ARAIM FD navigation performance suggest adding more GNSS measurements could significantly improve navigation integrity, even if those measurements are subject to large fault probabilities and errors. In addition, implementing the proposed exclusion scheme provides high availability for both H- and V-ARAIM (for those scenarios when exclusion function is required). And those high navigation performance will not be noticeably degraded due to the satellite USO. Moreover, the impact of the test statistic time correlation is mainly on continuity. This impact can be mitigated by increasing the detection thresholds, while achieving the same level of

ARAIM service availability.

8.2 ARAIM Offline Monitor Performance

Both covariances and model fidelities are analyzed to assess the impact of RS measurement error and model fitting error on the proposed monitors performance: the most robust implementation with the overall lowest SV orbit/clock errors is achieved by making no assumptions on SV or RS clock dynamics and by using the CNAV orbit model. This monitor is predicted to achieve a signal in space range error standard deviation $\sigma_{MONITOR}$ of about 0.3 m, which will allow validation ARAIM user range accuracies σ_{URA} of 1.05 m if the actual σ_{URA} is 1 m.

8.3 Summary of Achievements

The focus of this research has been (a) the developments of new methods to improve navigation integrity and continuity using ARAIM, and (b) the investigation of the achievable ARAIM navigation performance and its robustness against multiple impacts. Areas of contributions are discussed in the following subsections.

8.3.1 Develop the Theory to Quantify ARAIM Continuity Risk. In this dissertation, the ARAIM continuity requirements are interpreted with respect to different operation scenarios, where the assumptions are laid out and the rationale is clarified. The V- and H-ARAIM continuity risks are respectively quantified by accounting for the impact of both fault occurrences and USO. New methods are introduced to limit the impact of each source on navigation continuity. The cases when an airborne fault exclusion function is required are identified.

8.3.2 Develop Fault Exclusion Scheme and New Bound on the Associated Integrity Risk. A SS based fault exclusion algorithm is designed to improve ARAIM navigation continuity. This algorithm can be executed efficiently in real-time with a low probability of wrong exclusion. To ensure safety, a second-layer

detection test is performed to verify that the satellite subset after exclusion is fault free. The associated integrity risk equations are bounded step by step, by accounting for all the exclusion options.

8.3.3 Analyzing Multi-Constellation ARAIM Performance. Using the new methods derived in this thesis, the ARAIM navigation performance is comprehensively investigated over various numbers and qualities of constellations. The results are presented in terms of specific ARAIM operation scenarios.

8.3.4 Investigate the Impact of Test Statistic Time Correlation on ARAIM Integrity and Continuity Risk. This work investigates the impact of ARAIM test statistic time correlation on both integrity and continuity, by deriving new methods to rigorously evaluate the risks over the exposure time. Both the analytical and experimental results show that the time correlation of test statistics does not cause a noticeable integrity risk increment, but the actual false alarm probability is in a two orders of magnitude higher than previously thought. A feasible solution to reduce the false alarm probability is provided, without degrading the ARAIM navigation availability.

8.3.5 Design an ARAIM Offline Ground Monitor to Validate the ISM. A new design of a ARAIM offline ground monitor is introduced in this dissertation, which aims at validating the ISM broadcast to the users. The proposed architecture utilizes a worldwide network of sparsely distributed reference stations, and parametric satellite orbital models to estimate the satellite position and clock. The results of the analyses on the monitor's performance indicate this monitor design is adequate for ARAIM ISM validation.

8.4 Recommendations for Future Work

A number of recommendations for future work are given in the following sub-

sections to speed up the pace of the application of ARAIM.

8.4.1 Reduce the Computational Load of ARAIM User Algorithm. The current baseline ARAIM user algorithm defines the test statics as the difference between full-set and subset position estimates, which requires the receiver to compute multiple positions in real-time implementation. This is not a significant problem for dual-constellation ARAIM, because the user usually only needs to monitor single SV and constellation fault modes. However, the number of monitored fault modes will increase exponentially when more than two constellations are employed. As a consequence, the receiver needs to evaluate a large amount of subset position estimates. This is especially concerning when exclusion function is implemented in real-time. Therefore, a feasible solution should be found to improve the computational efficiency for future multi-constellation ARAIM. There have been relevant research efforts on this topic [56, 55, 57, 58], but those existing methods usually come at a high cost of reduced navigation performance. Therefore, more analyses needs to be carried out to capture those tradeoffs.

8.4.2 Extend the Investigation of Test Statistic Time Correlation on ARAIM FDE Function. The focus of Chapter 6 is on the ARAIM FD function, whereas the proposed methods can also be applied for the fault exclusion function. A comprehensive investigation of the impact of the test statistic time correlation on ARAIM airborne algorithm may be desired. With exclusion function, the LOC events will be described as a joint event of detection but NE, so the time profiles of both detection and exclusion test statistics need to be characterized. In addition, a large amount of the observation data should be collected for theory validation.

8.4.3 Prototyping ARAIM Offline Monitor. The results shown in Chapter 7 have motivated the prototyping of the offline monitor concept using experimental data. Raw ranging observations collected at IGS RS can be used as a surrogate for

SBAS RS data, which are not publicly accessible. Since L5 measurements are not yet available for all satellites as assumed in ARAIM, L1 and L2 can be used instead to remove the ionospheric delay. Even though the offline monitoring methodology is straightforward, many practical issues may arise when building and implementing the prototype. For example, format anomalies and missing bits in the observation files make it challenging to correctly extract data; the iteration loop of the non-linear orbit and clock estimation process does not always converge; error models used in the analyses may not be suitable to characterize the error profiles of the collected data. Therefore, research efforts may also need to be put on resolving the above issues, and it is expected the prototype to provide performance consistent with the analyses.

8.4.4 Establishing the Mechanism to Validate the ISM. As mentioned in section 2.2, current work on determining the ISM parameters are mostly based on the CSP commitment and the observations of historical data. So they are not applicable for newly deployed constellations. Even for the GPS, the characterized historical constellation performance only validates the CSP commitment, not the ISM. Therefore, new methods should be developed to validate the ISM. And a communication mechanism between the CSP and the aviation users may also need to be established.

8.5 Closing

High navigation integrity and continuity for civil aviation users can be provided by dual-frequency, multi-constellation ARAIM.

APPENDIX A
DERIVATION OF EQUATIONS TO COMPUTE FDE THRESHOLDS USING
NON-EQUAL $C_{REQ,H}$ ALLOCATION

This appendix derives the equations to compute the FDE thresholds when different continuity budgets are allocated to USO conditions. The first term of equation 3.14 in the main text can be bounded by:

$$\begin{aligned} P_{FANE,OF} &< P \left(\bigcup_{d=1}^{h^0} |q_d^0| > T_d^0 | H_0, O_0 \right) P_{H_0} P_{O_0} \\ &< \sum_{d=1}^{h^0} P (|q_d^0| > T_d^0 | H_0, O_0) P_{H_0} P_{O_0} < P_{FF,OF,REQ} \end{aligned} \quad (\text{A.1})$$

where the upper right superscript ‘0’ represents the OF condition O_0 . Based on the allocated $P_{FF,OF,REQ}$ in Table 3.3, the first layer H-ARAIM detection thresholds T_d^0 under OF condition can be computed:

$$T_d^0 = Q^{-1} \left\{ \frac{P_{FF,OF,REQ}}{2P_{H_0}P_{O_0} \cdot h^0} \right\} \quad (\text{A.2})$$

The second term of equation 3.14 can be bounded by:

$$\begin{aligned} P_{FDNE,OF} &< \sum_{i=1}^{h^0} P \left(\bigcap_{e=1}^{h^0} \left(\bigcup_{l=1}^{h_e^0} |q_{e,l}^0| > T_{e,l}^0 \right) | H_i, O_0 \right) P_{H_i} P_{O_0} + P_{NM,Fault} P_{O_0} \\ &< \sum_{i=1}^{h^0} P \left(\bigcup_{l=1}^{h_e^0} |q_{i,l}^0| > T_{i,l}^0 | H_i, O_0 \right) P_{H_i} P_{O_0} + P_{NM,Fault} P_{O_0} \\ &< \sum_{i=1}^{h^0} \sum_{l=1}^{h_e^0} P (|q_{i,l}^0| > T_{i,l}^0 | H_i, O_0) P_{H_i} P_{O_0} + P_{NM,Fault} P_{O_0} < P_{FP,OF,REQ} \end{aligned} \quad (\text{A.3})$$

where $P_{NM,Fault}$ is the not monitored fault modes. Thus, the exclusion thresholds $T_{i,l}^0$ under OF condition can be evaluated:

$$T_{i,l}^0 = Q^{-1} \left\{ \frac{P_{FP,OF,REQ,H_i}}{2 \cdot h_e^0} \right\}, \text{ where } P_{FP,OF,REQ,H_i} = \frac{P_{FP,OF,REQ} - P_{NM,Fault} P_{O_0}}{h^0 \cdot P_{H_i} \cdot P_{O_0}} \quad (\text{A.4})$$

A similar approach to OF condition can be applied to compute FDE thresholds after USO has occurred, except the prior probabilities of USO are much smaller than

P_{O_0} . Therefore, the third term of equation 3.14 can be expressed as:

$$\begin{aligned}
P_{FANE,USO} &< \sum_{s=1}^h P \left(\bigcup_{d=1}^{h^s} |q_d^s| > T_d^s | H_0, O_s \right) P_{H_0} P_{O_s} + P_{H_0} P_{NM,USO} \\
&< \sum_{s=1}^h \sum_{d=1}^{h^s} P (|q_d^s| > T_d^s | H_0, O_s) P_{H_0} P_{O_s} + P_{H_0} P_{NM,USO} < P_{FF,USO,REQ}
\end{aligned} \tag{A.5}$$

where the upper right superscript 's' represents the USO condition O_s , $P_{NM,USO}$ is the not monitored USO modes. So, the detection threshold T_d^s under USO conditions can be evaluated by:

$$T_d^s = Q^{-1} \left\{ \frac{P_{FF,USO,REQ} - P_{H_0} P_{NM,USO}}{2P_{H_0} P_{O_s} \cdot h \cdot h^s} \right\} \tag{A.6}$$

The last term of equation 3.14 can be expressed as:

$$\begin{aligned}
P_{FDNE,USO} &< \sum_{s=1}^h \sum_{i=1}^{h^s} P \left(\bigcap_{e=1}^{h_e^s} \left(\bigcup_{l=1}^{h_e^s} |q_{e,l}^s| > T_{e,l}^s \right) | H_i, O_s \right) P_{H_i} P_{O_s} + P_{NM,Fault} P_{NM,USO} \\
&< \sum_{s=1}^h \sum_{i=1}^{h^s} P \left(\bigcup_{l=1}^{h_e^s} |q_{i,l}^s| > T_{i,l}^s | H_i, O_s \right) P_{H_i} P_{O_s} + P_{NM,Fault} P_{NM,USO} \\
&< \sum_{s=1}^h \sum_{i=1}^{h^s} \sum_{l=1}^{h_e^s} P (|q_{i,l}^s| > T_{i,l}^s | H_i, O_s) P_{H_i} P_{O_s} + P_{NM,Fault} P_{NM,USO} < P_{FP,USO,REQ}
\end{aligned} \tag{A.7}$$

Therefore, the exclusion thresholds $T_{i,l}^s$ under USO conditions can be evaluated:

$$T_{i,l}^s = Q^{-1} \left\{ \frac{P_{FP,USO,REQ,H_i}}{2 \cdot h_e^s} \right\}, \text{ where } P_{FP,USO,REQ,H_i} = \frac{P_{FP,USO,REQ} - P_{NM,Fault} P_{NM,USO}}{h \cdot h^s \cdot P_{H_i} \cdot P_{O_s}} \tag{A.8}$$

APPENDIX B

DERIVATION OF THE ACTUAL FA PROBABILITY UPPER BOUND

In equation 6.8, the probability of no detection over the exposure time is:

$$P\left(\bigcap_{k=1}^M \bar{D}_0^k | H_0\right) = P(\bar{D}_0^M | \bar{D}_0^{M-1}, \dots, \bar{D}_0^1, H_0) P(\bar{D}_0^{M-1} | \bar{D}_0^{M-2}, \dots, \bar{D}_0^1, H_0) \dots P(\bar{D}_0^2 | \bar{D}_0^1, H_0) P(\bar{D}_0^1 | H_0) \quad (\text{B.1})$$

Because events $\bar{D}_0^1, \dots, \bar{D}_0^M$ are positively correlated, the following lower bound can be used:

$$P\left(\bigcap_{k=1}^M \bar{D}_0^k | H_0\right) \geq P(\bar{D}_0^M | \bar{D}_0^{M-1}, H_0) P(\bar{D}_0^{M-1} | \bar{D}_0^{M-2}, H_0) \dots P(\bar{D}_0^2 | \bar{D}_0^1, H_0) \cdot P(\bar{D}_0^1 | H_0) = P(\bar{D}_0^1 | H_0) \prod_{k=2}^M P(\bar{D}_0^k | \bar{D}_0^{k-1}, H_0) \quad (\text{B.2})$$

where

$$P(\bar{D}_0^k | \bar{D}_0^{k-1}, H_0) = \frac{P(\bar{D}_0^k, \bar{D}_0^{k-1} | H_0)}{P(\bar{D}_0^{k-1} | H_0)} \quad (\text{B.3})$$

and

$$P(\bar{D}_0^k | H_0) = P(\bar{D}_0^k, \bar{D}_0^{k-1} | H_0) + P(\bar{D}_0^k, D_0^{k-1} | H_0) \quad (\text{B.4})$$

which is the same as

$$P(\bar{D}_0^k, \bar{D}_0^{k-1} | H_0) = P(\bar{D}_0^k | H_0) - P(\bar{D}_0^k, D_0^{k-1} | H_0) \quad (\text{B.5})$$

Combining the equations above:

$$P\left(\bigcap_{k=1}^M \bar{D}_0^k | H_0\right) \geq P(\bar{D}_0^1 | H_0) \prod_{k=2}^M \frac{P(\bar{D}_0^k | H_0) - P(\bar{D}_0^k, D_0^{k-1} | H_0)}{P(\bar{D}_0^{k-1} | H_0)} \quad (\text{B.6})$$

We assume that the sensor error process is stationary over the time interval of interest, i.e., k consecutive samples, so that

$$P(\bar{D}_0^1 | H_0) = P(\bar{D}_0^k | H_0) = P(\bar{D}_0^{k-1} | H_0) \quad (\text{B.7})$$

Now plug equations B.7 and B.6 into 6.8, then the upper bound of P_{FA}^{actual} becomes:

$$P_{FA}^{actual} < 1 - P(\bar{D}_0^k | H_0) \left\{ 1 - \frac{P(\bar{D}_0^k, D_0^{k-1} | H_0)}{P(\bar{D}_0^k | H_0)} \right\}^{M-1} \quad (\text{B.8})$$

which is the same as equation 6.9.

APPENDIX C
DERIVATION OF THE AUTOCORRELATION FUNCTION OF THE USER
ERROR

The Boeing Company and the Thales Group provided airborne data to create autocorrelation models for multipath and receiver noise. Raw code-minus-carrier data, with ionospheric effects removed, was used generate the autocorrelation models.

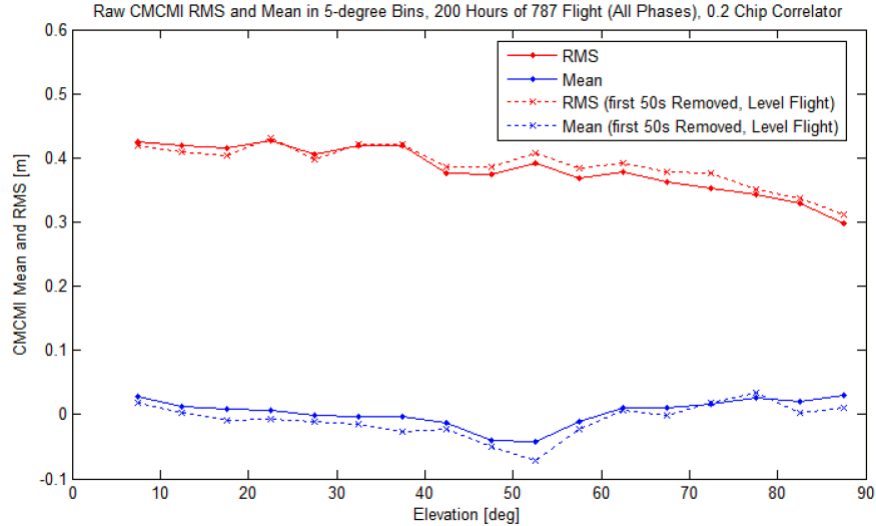


Figure C.1. Airborne Mean and Standard Deviation.

Figure C.1 shows the sample means and standard deviations binned by satellite elevation. The results suggest that it is reasonable to assume zero mean and average standard deviation of $\sigma_{user} = 0.38$ m for all elevations.

Figure C.2 shows a composite of autocorrelation traces of the flight data. A number traces with long correlation times are clearly evident; these are caused by antenna group delay, and must be accounted for in the autocorrelation model.

Figure C.3 consolidates the autocorrelation data into empirical cumulative distribution functions for a number of discrete lag times. The median lag time at $x = \frac{1}{e}$ is about 14 seconds, which is the τ_{user} value used for the analyses in Chapter 6.

To derive the autocorrelation function of the ‘‘Hatch Filter’’ output (carrier-smoothed-code), let p defined as the raw pseudorange, \bar{p} is the smoothed pseudorange,

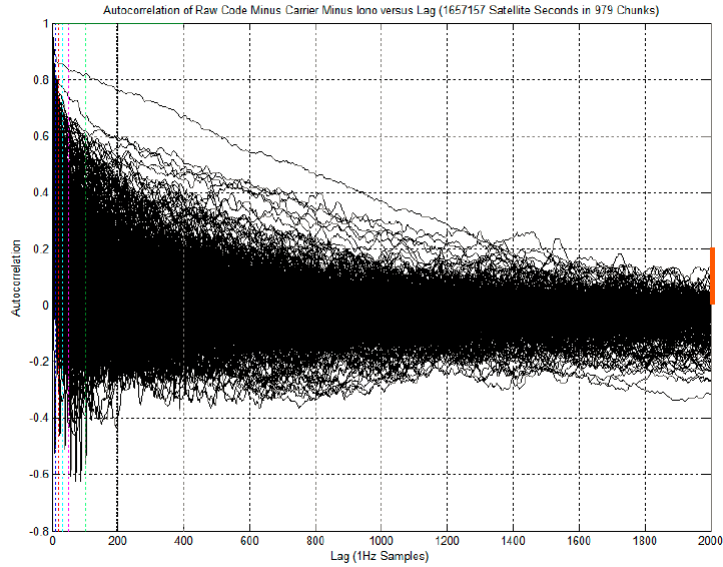


Figure C.2. Airborne Autocorrelation Traces.

and ϕ is the carrier phase. Recall that τ_{CSC} is the carrier-smoothing time constant, the filter can be expressed in continuous in the following form:

$$\tau_{CSC}\dot{\bar{p}}(t) + \bar{p}(t) = \tau_{CSC}\dot{\phi}(t) + p(t) \quad (\text{C.1})$$

Taking the Laplace Transform gives [46]:

$$E_{\bar{p}}(s) = \frac{\tau_{CSC}s}{\tau_{CSC}s + 1} E_{\phi}(s) + \frac{1}{\tau_{CSC}s + 1} E_p(s) \quad (\text{C.2})$$

where we assume:

$$E_{\phi} = \frac{\sqrt{N_{\phi}}}{\tau_{user}s + 1}, \text{ and } E_p = \frac{\sqrt{N_p}}{\tau_{user}s + 1} \quad (\text{C.3})$$

In equation C.3, N_{ϕ} and N_p are white noise inputs. It is noteworthy that the user time constant τ_{user} need not be the same for code and carrier, but in this derivation, it will be assumed they are the same. Then the standard deviations of

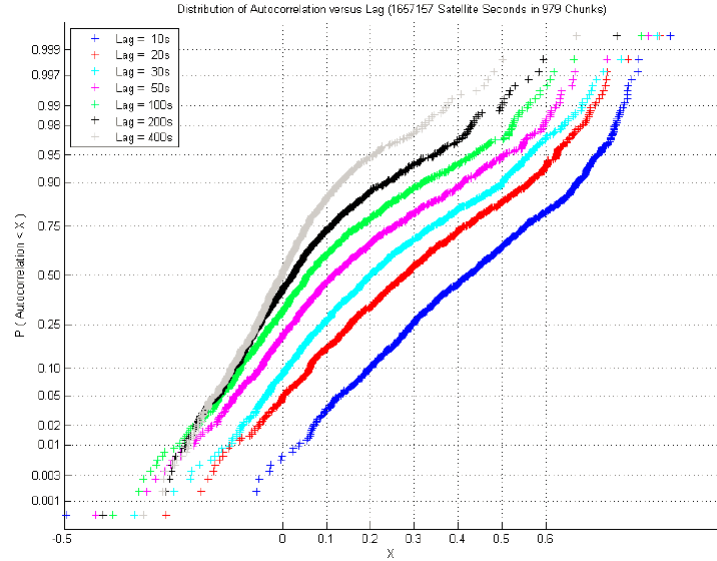


Figure C.3. Airborne Autocorrelation Distributions at Various Lag Times.

the code and carrier can be computed by:

$$\begin{aligned}
 \sigma_p^2 &= N_p \int_{-\infty}^{+\infty} \frac{1}{\tau_{user}^2 (2\pi f)^2 + 1} df \\
 &= \frac{N_p}{2\pi} \int_{-\infty}^{+\infty} \frac{1}{\tau_{user}^2 \omega^2 + 1} d\omega \\
 &= \frac{N_p}{2\pi} \frac{1}{\tau_{user}} \left(\frac{\pi}{2} + \frac{\pi}{2} \right) = \frac{N_p}{2\tau_{user}}
 \end{aligned} \tag{C.4}$$

Similarly, it can be derived that:

$$\sigma_\phi^2 = \frac{N_\phi}{2\tau_{user}} \tag{C.5}$$

Substituting equations C.4 and C.5 into equation C.3, and then into equation C.2:

$$E_{\bar{p}}(s) = \frac{\tau_{CSC} s}{\tau_{CSC} s + 1} \frac{\sqrt{2\tau_{user}\sigma_\phi^2}}{\tau_{user} s + 1} + \frac{1}{\tau_{CSC} s + 1} \frac{\sqrt{2\tau_{user}\sigma_p^2}}{\tau_{user} s + 1} \tag{C.6}$$

Then, the power spectral density (PSD) function is:

$$\begin{aligned}
 PSD_{\bar{p}}(s) &= 2\tau_{CSC}^2 \tau_{user} \sigma_\phi^2 \frac{-s^2}{(-\tau_{CSC}^2 s^2 + 1)(-\tau_{user}^2 s^2 + 1)} \\
 &\quad + 2\tau_{user} \sigma_p^2 \frac{1}{(-\tau_{CSC}^2 s^2 + 1)(-\tau_{user}^2 s^2 + 1)}
 \end{aligned} \tag{C.7}$$

Let the two terms on the right side of equation C.7 respectively defined as $PSD_{\bar{p}/\phi}$ and $PSD_{\bar{p}/p}$, and let $s = j\omega$. Therefore:

$$PSD_{\bar{p}/\phi}(\omega) = 2\tau_{CSC}^2 \tau_{user} \sigma_\phi^2 \frac{\omega^2}{(\tau_{CSC}^2 \omega^2 + 1)(\tau_{user}^2 \omega^2 + 1)} \quad (C.8)$$

$$PSD_{\bar{p}/p}(\omega) = 2\tau_{user} \sigma_p^2 \frac{1}{(\tau_{CSC}^2 \omega^2 + 1)(\tau_{user}^2 \omega^2 + 1)} \quad (C.9)$$

Taking the inverse Fourier transformation, the autocorrelation functions can be obtained:

$$R_{\bar{p}/\phi}(\Delta t) = \frac{1}{2\pi} \int_{-\infty}^{+\infty} PSD_{\bar{p}/\phi}(\omega) \cos(\omega \Delta t) d\omega \quad (C.10)$$

$$R_{\bar{p}/p}(\Delta t) = \frac{1}{2\pi} \int_{-\infty}^{+\infty} PSD_{\bar{p}/p}(\omega) \cos(\omega \Delta t) d\omega \quad (C.11)$$

To solve for equation C.10, equation C.8 is first rewritten as:

$$PSD_{\bar{p}/\phi} = \frac{2\sigma_\phi^2}{\tau_{user}} \frac{\omega^2}{(\omega^2 + a^2)(\omega^2 + b^2)} \quad (C.12)$$

where $a = \tau_{CSC}^{-1}$ and $b = \tau_{user}^{-1}$.

To accommodate the expression of the Fourier transformation table, $PSD_{\bar{p}/\phi}$ is further expressed as:

$$\begin{aligned} PSD_{\bar{p}/\phi} &= \frac{2\sigma_\phi^2}{\tau_{user}} \omega^2 \left(\frac{1}{(\omega^2 + a^2)(\omega^2 + b^2)} \right) \\ &= \frac{2\sigma_\phi^2}{\tau_{user}} \omega^2 \left(\frac{A}{\omega^2 + a^2} + \frac{B}{\omega^2 + b^2} \right) \\ &= \frac{2\sigma_\phi^2}{\tau_{user}} \left(-\frac{Aa}{2} \frac{2a}{\omega^2 + a^2} - \frac{Bb}{2} \frac{2b}{\omega^2 + b^2} \right) \end{aligned} \quad (C.13)$$

where $A = \frac{1}{b^2 - a^2}$ and $B = \frac{-1}{b^2 - a^2}$.

Therefore, the autocorrelation function of equation C.10 can be solved:

$$\begin{aligned} R_{\bar{p}/\phi}(\Delta t) &= \frac{2\sigma_\phi^2}{\tau_{user}} \frac{1}{2} \frac{1}{\tau_{CSC}^{-2} - \tau_{user}^{-2}} \left(\frac{e^{-|\Delta t|/\tau_{CSC}}}{\tau_{CSC}} - \frac{e^{-|\Delta t|/\tau_{user}}}{\tau_{user}} \right) \\ &= \sigma_\phi^2 \frac{\tau_{CSC} \tau_{user}}{\tau_{user}^2 - \tau_{CSC}^2} \left(\frac{e^{-|\Delta t|/\tau_{CSC}}}{\tau_{CSC}} - \frac{e^{-|\Delta t|/\tau_{user}}}{\tau_{user}} \right) \end{aligned} \quad (C.14)$$

Similar approach can be applied to derive the autocorrelation function $R_{\bar{p}/p}$, the key steps are listed in the following equations:

$$\begin{aligned}
 PSD_{\bar{p}/p} &= \frac{2\tau_{user}\sigma_p^2}{\tau_{CSC}^2\tau_{user}^2} \frac{1}{(\omega^2 + a^2)(\omega^2 + b^2)} \\
 &= \frac{2\tau_{user}\sigma_p^2}{\tau_{CSC}^2\tau_{user}^2} \left(\frac{A}{\omega^2 + a^2} + \frac{B}{\omega^2 + b^2} \right) \\
 &= \frac{2\tau_{user}\sigma_p^2}{\tau_{CSC}^2\tau_{user}^2} \frac{A}{2} \left(\frac{1}{a} \frac{2a}{\omega^2 + a^2} - \frac{1}{b} \frac{2b}{\omega^2 + b^2} \right)
 \end{aligned} \tag{C.15}$$

$$R_{\bar{p}/p}(\Delta t) = \frac{\sigma_p^2\tau_{user}}{\tau_{CSC}^2 - \tau_{user}^2} (\tau_{CSC}e^{-|\Delta t|/\tau_{CSC}} - \tau_{user}e^{-|\Delta t|/\tau_{user}}) \tag{C.16}$$

Because $R_{\bar{p}/\phi} \ll R_{\bar{p}/p}$ and $\sigma_\phi \ll \sigma_p$, the autocorrelation function of the carrier-smoothed-code $R_{\bar{p}}$ can be approximated by equation C.16, which is the same as equation 6.17 after removing the iono-free factor κ .

APPENDIX D
DERIVATION OF THE AUTOCORRELATION FUNCTION OF THE
SIGNAL-IN-SPACE ERROR

According to the results in [26] (figure D.1), the SIS error has been decreasing over the last five years. The black bold line in figure D.1 corresponds to the average user position error over all the satellites. In 2017, the 95 % error bound is 1 m, which corresponds to σ_{URE} of 0.5 m.

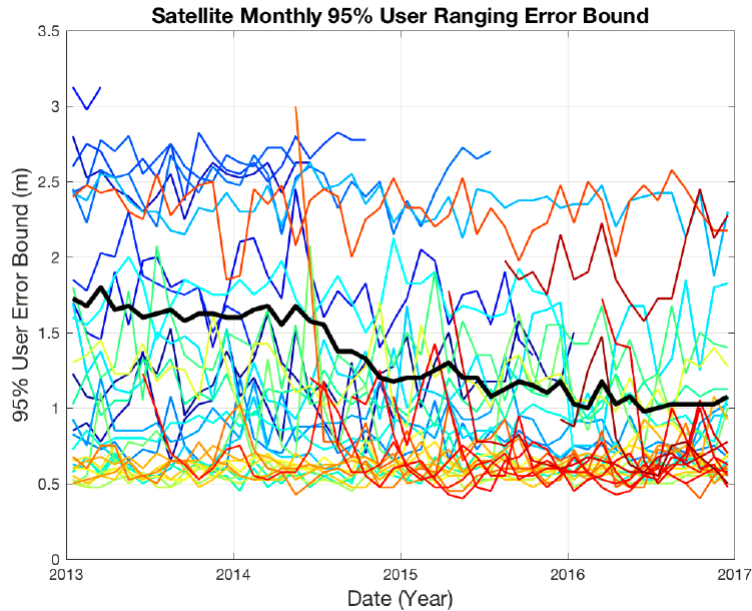


Figure D.1. Monthly 95 % Bound of User Position Error on Each Satellite (Figure Courtesy of Dr. Todd Walter).

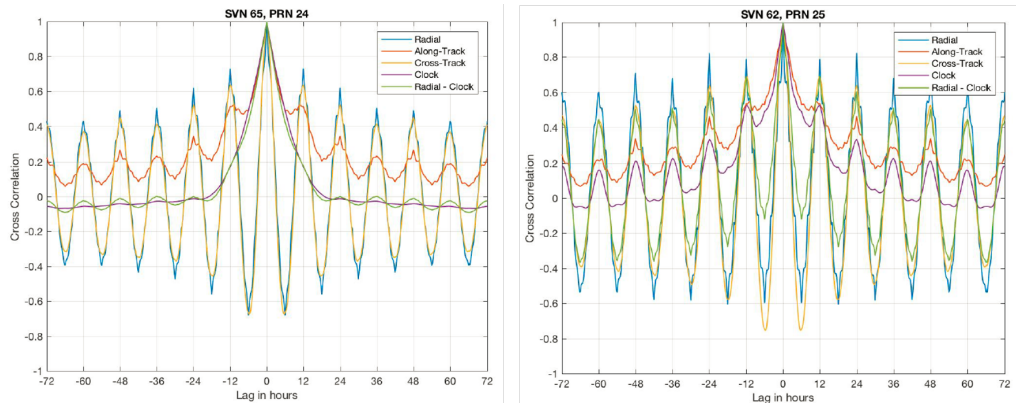


Figure D.2. Autocorrelation of SIS Error for Two Example Satellites (Figure Courtesy of Dr. Todd Walter).

The SIS error has very long correlation time [60, 61, 26]. The autocorrelations for two example satellites are shown in figure D.2, for which PRN 24 is equipped

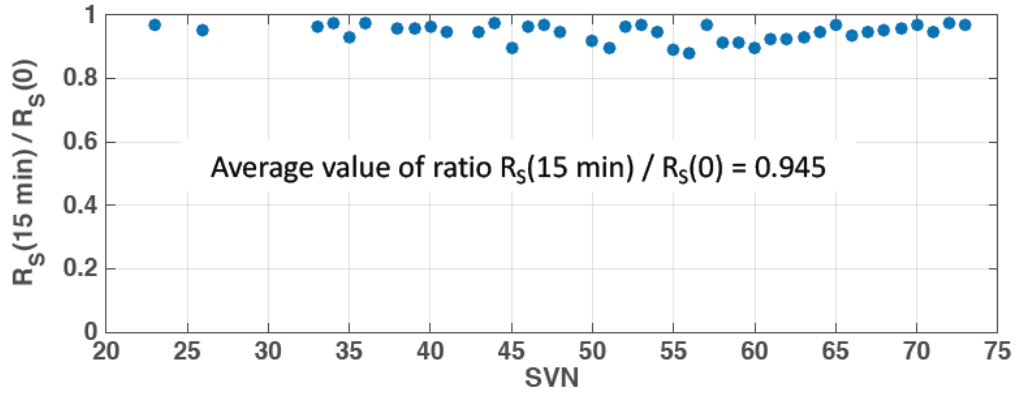


Figure D.3. SIS Error Autocorrelation Ratios.

with a cesium clock and PRN 25 has a rubidium clock. The radial-minus-clock autocorrelation data is employed and averaged over all the GPS satellites. The data sample interval is 15 min, and the ratios of $R_{SIS}(15min)$ over $R_{SIS}(0)$ are shown in figure D.3.

Using the average value of ratio (0.945), and by linearly interpolating the lag times between 0 and 15 min, the autocorrelation function of SIS error can be written as:

$$\frac{1 - R_{SIS}(t)}{1 - 0.945} = \frac{t}{15 \times 60} \quad (\text{D.1})$$

which is the same as equation 6.19.

APPENDIX E
CHARACTERIZING THE USER ERROR PROFILE OF THE IIT ARAIM
PROTOTYPE

Figure E.1 shows the aggregate code minus carrier (CMC) CDF using GPS observation data of L1 and L2 frequency. The results are very similar for both cases, where the average standard deviation σ_{user} is about 0.38 m and the overbound sigma is larger than 0.7 m. Because the CDF of the data points show a wide tail, the actual σ_{user} is expected to be in between 0.38 m and 0.7 m. That is why $\sigma_{user} = 0.6$ m is applied in the analysis in section 6.5.

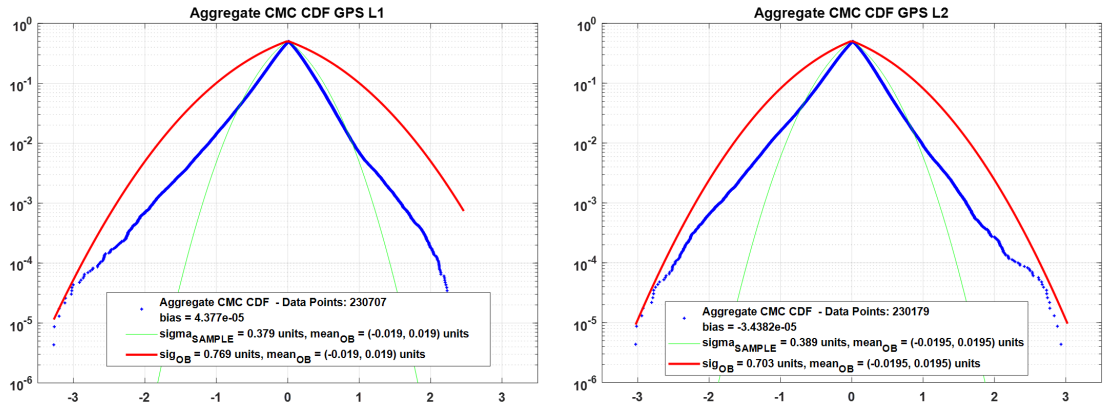


Figure E.1. CMC CDF Using Data Collected by IIT Prototype.

APPENDIX F

KALMAN FILTER APPROACH FOR THE OFFLINE GROUND MONITOR

In addition to the batch estimator, this appendix derives a Kalman Filter (KF) approach for the offline monitor in Chapter 7. The KF implementation is more computationally efficient, and it allows us to cross-check with the results from batch estimator. At one time epoch k , the measurement equation is expressed as:

$$\begin{bmatrix} {}^{1,1}\delta\rho_k \\ {}^{1,2}\delta\rho_k \\ \vdots \\ {}^{1,J}\delta\rho_k \\ \vdots \\ {}^{i,j}\delta\rho_k \\ \vdots \\ {}^{I,J}\delta\rho_k \\ {}^{1,1}\delta\phi_k \\ \vdots \\ {}^{I,J}\delta\phi_k \end{bmatrix} = \begin{bmatrix} {}^{1,1}\mathbf{B}_k & \mathbf{0}_{1\times 15} \cdots \mathbf{0}_{1\times 15} & 1 & \cdots & \mathbf{0}_{1\times K} & \mathbf{0}_{1\times 3} & \cdots & \mathbf{0}_{1\times 3} & 0 \cdots 0 & OB & 0 & \cdots 0 \\ {}^{1,2}\mathbf{B}_k & \mathbf{0}_{1\times 15} \cdots \mathbf{0}_{1\times 15} & 1 & \cdots & \mathbf{0}_{1\times K} & \mathbf{A}_{2,k}^{clk} & \cdots & \mathbf{0}_{1\times 3} & 0 \cdots 0 & 0 & OB & \cdots 0 \\ \vdots & \vdots & \vdots & \vdots & \vdots & \vdots & \ddots & \vdots & \vdots & \vdots & \vdots & \ddots \\ {}^{1,J}\mathbf{B}_k & \mathbf{0}_{1\times 15} \cdots \mathbf{0}_{1\times 15} & 1 & \cdots & \mathbf{0}_{1\times K} & \mathbf{0}_{1\times 3} & \cdots & \mathbf{A}_{J,k}^{clk} & 0 \cdots 0 & 0 & \cdots 0 & OB \\ \vdots & \vdots & \vdots & \vdots & \vdots & \vdots & \ddots & \vdots & \vdots & \vdots & \vdots & \ddots \\ {}^{i,j}\mathbf{B}_k & \mathbf{0}_{1\times 15} \cdots \mathbf{0}_{1\times 15} & \mathbf{0}_{1\times K} & 1 \cdots & \mathbf{0}_{1\times K} & \mathbf{0}_{1\times 3} & \mathbf{A}_{j,k}^{clk} & \cdots \mathbf{0}_{1\times 3} & 0 \cdots 0 & 0 & OB & \cdots 0 \\ \vdots & \vdots & \vdots & \vdots & \vdots & \vdots & \vdots & \vdots & \vdots & \vdots & \vdots & \ddots \\ {}^{I,J}\mathbf{B}_k & \mathbf{0}_{1\times 15} \cdots \mathbf{0}_{1\times 15} & {}^{I,J}\mathbf{B}_k & \mathbf{0}_{1\times K} & \cdots & 1 & \mathbf{0}_{1\times 3} & \cdots & \mathbf{A}_{J,k}^{clk} & 0 \cdots 0 & 0 & \cdots 0 & OB \\ {}^{1,1}\mathbf{B}_k & \mathbf{0}_{1\times 15} \cdots \mathbf{0}_{1\times 15} & 1 & \cdots & \mathbf{0}_{1\times K} & \mathbf{0}_{1\times 3} & \cdots & \mathbf{0}_{1\times 3} & 1 \cdots 0 & OB & 0 & \cdots 0 \\ \vdots & \vdots & \vdots & \vdots & \vdots & \vdots & \ddots & \vdots & \vdots & \vdots & \vdots & \ddots \\ {}^{I,J}\mathbf{B}_k & \mathbf{0}_{1\times 15} \cdots \mathbf{0}_{1\times 15} & {}^{I,J}\mathbf{B}_k & \mathbf{0}_{1\times K} & \cdots & 1 & \mathbf{0}_{1\times 3} & \cdots & \mathbf{A}_{J,k}^{clk} & 0 \cdots 1 & 0 & \cdots 0 & OB \end{bmatrix} \begin{bmatrix} \delta\mathbf{p}_1^{orb} \\ \vdots \\ \delta\mathbf{p}_I^{orb} \\ \tau_{1,K} \\ \vdots \\ \tau_{I,K} \\ \mathbf{p}_2^{clk} \\ \vdots \\ \mathbf{p}_J^{clk} \\ \vdots \\ {}^{i,j}\eta \\ \varepsilon_{tropo,1,k}^{ZTD} \\ \vdots \\ \varepsilon_{tropo,J,k}^{ZTD} \end{bmatrix} + \begin{bmatrix} {}^{1,1}\varepsilon_{\rho,k}^{RNM} \\ {}^{1,2}\varepsilon_{\rho,k}^{RNM} \\ \vdots \\ {}^{1,J}\varepsilon_{\rho,k}^{RNM} \\ \vdots \\ {}^{i,j}\varepsilon_{\rho,k}^{RNM} \\ \vdots \\ {}^{I,J}\varepsilon_{\rho,k}^{RNM} \\ {}^{1,1}\varepsilon_{\phi,k}^{RNM} \\ \vdots \\ {}^{I,J}\varepsilon_{\phi,k}^{RNM} \end{bmatrix} \quad (\text{F.1})$$

Comparing to equation 7.10, the additional states $\varepsilon_{tropo,j,k}^{ZTD}$ in equation F.1 represent the residual ZTD at RS j , and OB is the obliquity factor. We use state augmentation to account for time correlation of the tropospheric ZTD error [52]. Because $\varepsilon_{tropo,j}^{ZTD}$ is modeled as a first order Gauss-Markov process (FOGMP), the associated dynamic model of the KF approach is:

$$\begin{bmatrix} \mathbf{s}_{k+1} \\ \varepsilon_{tropo,k+1}^{ZTD} \end{bmatrix} = \begin{bmatrix} \mathbf{I} & \mathbf{0} \\ \mathbf{0} & e^{-T/\mu}\mathbf{I}_{J\times J} \end{bmatrix} \begin{bmatrix} \mathbf{s}_k \\ \varepsilon_{tropo,k}^{ZTD} \end{bmatrix} + \begin{bmatrix} \mathbf{0} \\ \mathbf{1}_{J\times 1} \end{bmatrix} \omega_{tropo,k}^{ZTD} \quad (\text{F.2})$$

In equation F.2, the first row accounts for the states of equation 7.10, which do not change over time. The second row shows the dynamics of FOGMP, where T is the sample period and μ is the time constant. $\varepsilon_{tropo,k}^{ZTD}$ is obtained by stacking $\varepsilon_{tropo,j,k}^{ZTD}$

of all RS, and the variance of $\omega_{tropo,k}^{ZTD}$ is $(1 - e^{-2(T/\mu)}) \sigma_{ZTD}^2$ [59]. As a result, with both the measurement equation and dynamic model available, the nominal KF steps [52] can be implemented to estimate SV orbit/clock.

BIBLIOGRAPHY

- [1] B. Pervan. *Navigation integrity for aircraft precision landing using the global positioning system*. PhD thesis, Department of Aeronautics and Astronautics, Stanford University, Stanford, CA, 1996.
- [2] Y. C. Lee. Analysis of Range and Position Comparison Methods as a Means to Provide GPS Integrity in the User Receiver. In *Proceedings of the 42nd Annual Meeting of The Institute of Navigation*, pages 1–4, Seattle, WA, 1986.
- [3] B. W. Parkinson and P. Axelrad. Autonomous GPS Integrity Monitoring Using the Pseudorange Residual. *NAVIGATION, Journal of The Institute of Navigation*, 35(2):255–274, 1988.
- [4] RTCA SC-159. *Minimum Operational Performance Standards for Airborne Supplemental Navigation Equipment Using Global Positioning System (GPS)*. RTCA, Incorporated, July 1991.
- [5] Assistant Secretary of Defense for Command, Control, Communications and Intelligence. *Global Positioning System Standard Positioning Service Performance Standard*. Washington, DC, 2008. Available at <http://www.gps.gov/technical/ps/2008-SPS-performance-standard.pdf>.
- [6] RTCA SC-159. *Minimum Aviation System Performance Standards for the Local Area Augmentation System (LAAS)*. RTCA, Incorporated, 2004.
- [7] RTCA SC-159. *Minimum Operational Performance Standards for Global Positioning System/Wide Area Augmentation System Airborne Equipment*. RTCA, Incorporated, 2006.
- [8] J. Blanch, T. Walter, P. Enge, Y. C. Lee, B. Pervan, M. Rippl, A. Spletter and V. Kropp. Baseline Advanced RAIM User Algorithm and Possible Improvements. *IEEE Transactions on Aerospace and Electronic Systems*, 51(1):713–732, 2015.
- [9] *Phase II of the GNSS Evolutionary Architecture Study*. February 2010. Available at https://www.faa.gov/about/office_org/headquarters_offices/ato/service_units/techops/navservices/gnss/library/documents/media/GEASPhaseII_Final.pdf.
- [10] P. Misra and P. Enge. *Global Positioning System: Signals, Measurements and Performance Second Edition*. Lincoln, MA: Ganga-Jamuna Press, 2006.
- [11] M. Joerger, F. C. Chan and B. Pervan. Solution Separation Versus Residual-Based RAIM. *NAVIGATION, Journal of The Institute of Navigation*, 61(4):273–291, 2014.
- [12] G. Gibbons. Munich Summit Charts Progress of GPS, GLONASS, Galileo, BeiDou GNSSes. *Inside GNSS*, 2012.
- [13] P. Enge, N. Enge, T. Walter and L. Eldredge. Aviation Benefits from Satellite Navigation. *New Space*, 2014.
- [14] I. Leveson. The L2C Study: Benefits of the New GPS Civil Signal. *Inside GNSS*, July/August 2006.

- [15] GPS World Staff. The System: GLONASS in April, What Went Wrong. *GPS World*, June 2014.
- [16] FAA AC 20-138B. *Airworthiness Approval of Positioning and Navigation Systems*. September, 2010.
- [17] FAA-E-2892d. *System Specification for the Wide Area Augmentation System*. March 28, 2012.
- [18] Y. C. Lee, K. V. Dyke, B. Declene, J. Studenny and M. Beckmann. Summary of RTCA SC-159 GPS Integrity Working Group Activities. *NAVIGATION, Journal of The Institute of Navigation*, 43(3):307–362, 1996.
- [19] EU-U.S. Cooperation on Satellite Navigation, Working Group C. *ARAIM Technical Subgroup Interim Report Issue 1.0*. December 19, 2012. Available at <https://www.gps.gov/policy/cooperation/europe/2013/working-group-c/ARAIM-report-1.0.pdf>.
- [20] EU-U.S. Cooperation on Satellite Navigation, Working Group C. *ARAIM Technical Subgroup Milestone 2 Report*. November 28, 2014. Available at <https://www.gps.gov/policy/cooperation/europe/2015/working-group-c/ARAIM-milestone-2-report.pdf>.
- [21] EU-U.S. Cooperation on Satellite Navigation, Working Group C. *ARAIM Technical Subgroup Milestone 3 Report*. February 25, 2016. Available at <http://www.gps.gov/policy/cooperation/europe/2016/working-group-c/ARAIM-milestone-3-report.pdf>.
- [22] ICAO, Annex 10. *Aeronautical Telecommunications, Volume 1 (Radio Navigation Aids), Amendment 84*. published 20 July 2009, effective 19 November 2009.
- [23] M. Joerger, S. Stevanovic, F. C. Chan, S. Langel and B. Pervan. Integrity Risk and Continuity Risk for Fault Detection and Exclusion Using Solution Separation ARAIM. In *Proceedings of the 26th International Technical Meeting of The Satellite Division of the Institute of Navigation*, pages 2702–2722, Nashville, TN, 2013.
- [24] M. Joerger and B. Pervan. Fault Detection and Exclusion Using Solution Separation and Chi-Squared RAIM. *IEEE Transactions on Aerospace and Electronic Systems*, 52(2):726–742, 2016.
- [25] M. Joerger, S. Langel and B. Pervan. Integrity Risk Minimisation in RAIM Part 2: Optimal Estimator Design. *The Journal of Navigation*, 69(4):709–728, 2016.
- [26] T. Walter, K. Gunning, and J. Blanch. Validation of the Unfaulted Error Bounds for ARAIM. In *Proceedings of the ION 2017 Pacific PNT Meeting*, pages 1–19, Honolulu, HI, 2017.
- [27] T. Walter and J. Blanch. Characterization of GNSS Clock and Ephemeris Errors to Support ARAIM. In *Proceedings of the ION 2015 Pacific PNT Meeting*, pages 920–931, Honolulu, HI, 2015.
- [28] T. Walter, J. Blanch, M. Joerger and B. Pervan. Determination of Fault Probabilities for ARAIM. In *Proceedings of the IEEE/ION PLANS 2016*, pages 451–461, Savannah, GA, 2016.

- [29] L. Heng, G. X. Gao, T. Walter and P. Enge. Automated Verification of Potential GPS Signal-In-Space Anomalies Using Ground Observation Data. In *Proceedings of the IEEE/ION PLANS 2012*, pages 1111–1118, Myrtle Beach, SC, 2012.
- [30] L. Heng. *Safe Satellite Navigation with Multiple Constellations: Global Monitoring of GPS and GLONASS Signal-in-Space Anomalies*. PhD thesis, Department of Aeronautics and Astronautics, Stanford University, Stanford, CA, December 2012.
- [31] J. Blanch, T. Walter, P. Enge and V. Kropp. A Simple Position Estimator that Improves Advanced RAIM Performance. *IEEE Transactions on Aerospace and Electronic Systems*, 51(3):2485–2489, 2015.
- [32] Y. C. Lee, and M. McLaughlin. Feasibility Analysis of RAIM to Provide LPV-200 Approaches with Future GPS. In *Proceedings of the 20th International Technical Meeting of the Satellite Division of The Institute of Navigation*, pages 2898–2910, Fort Worth, TX, 2007.
- [33] Y. Zhai, M. Joerger and B. Pervan. H-ARAIM Exclusion: Requirements and Performance. In *Proceedings of the 29th International Technical Meeting of The Satellite Division of the Institute of Navigation*, pages 1713–1725, Portland, OR, 2016.
- [34] Y. Zhai, M. Joerger and B. Pervan. Bounding Continuity Risk in H-ARAIM FDE. In *Proceedings of the ION 2017 Pacific PNT Meeting*, pages 20–35, Honolulu, HI, 2017.
- [35] J. Blanch, T. Walter and P. Enge. Exclusion for Advanced RAIM: Requirements and a Baseline Algorithm. In *Proceedings of the 2014 International Technical Meeting of The Institute of Navigation*, pages 99–107, San Diego, CA, 2014.
- [36] J. Blanch, T. Walter and P. Enge. A Simple Satellite Exclusion Algorithm for Advanced RAIM. In *Proceedings of the 2016 International Technical Meeting of The Institute of Navigation*, pages 239–244, Monterey, CA, 2016.
- [37] Y. Zhai, M. Joerger and B. Pervan. Continuity and Availability in Dual-Frequency Multi-Constellation ARAIM. In *Proceedings of the 28th International Technical Meeting of The Satellite Division of the Institute of Navigation*, pages 664–674, Tampa, FL, 2015.
- [38] E. Bang, C. Milner, C. Christophe and P. Estival. ARAIM Test Statistic Correlation. In *Proceedings of the 2018 International Technical Meeting of The Institute of Navigation*, pages 99–113, Reston, VA, 2018.
- [39] R. Cassel. *Real-Time ARAIM Using GPS, GLONASS, and Galileo*. M.S. thesis, Department of Mechanical, Materials, and Aerospace Engineering, Illinois Institute of Technology, Chicago, IL, 2017.
- [40] I. E. Potter and M. C. Suman. Threshold-less Redundancy Management With Arrays of Skewed Instruments. *AGARDOGRAPH*, 224, 15-11 to 15-25, 1977.
- [41] M. Sturza. Navigation System Integrity Monitoring Using Redundant Measurements. *NAVIGATION, Journal of The Institute of Navigation*, 35(4):483–502, 1988.
- [42] J. Blanch, T. Walter and P. Enge and V. Kropp. RAIM with Optimal Integrity and Continuity Allocations under Multiple Failures. *IEEE Transactions on Aerospace and Electronic Systems*, 46(3):1235–1247, 2010.

- [43] M. Brenner. Concern Regarding Mean Time Between Trials for a Smoothed Signal. *RTCA SC-159/WG-4/30*, August, 2001.
- [44] C. Shively and C. Varner. Impact of Carrier Smoothing on Event Probabilities in LAAS. In *Proceedings of the 58th Annual Meeting of The Institute of Navigation and CIGTF 21st Guidance Test Symposium*, pages 195–205, Albuquerque, NM, 2002.
- [45] J. Rife and P. Misra. Impact of Time-Correlation of Monitor Statistic on Continuity of Safety-Critical Operations. *NAVIGATION, Journal of The Institute of Navigation*, 59(4):303–315, 2012.
- [46] B. Pervan, S. Khanafseh and J. Patel. Test Statistic Auto- and Cross-correlation Effects on Monitor False Alert and Missed Detection Probabilities. In *Proceedings of the 2017 International Technical Meeting of The Institute of Navigation*, pages 562–590, Monterey, CA, 2017.
- [47] A. Papoulis. *Probability, Random Variables, and Stochastic Processes*. McGraw-Hill, 1965.
- [48] J. Blanch, T. Walter, P. Enge, B. Pervan, M. Joerger, S. Khanafseh, J. Burns, K. Alexander, J. P. Boyero, Y. C. Lee, V. Kropp, C. Milner, C. Macabiau, N. Suard, G. Berz and M. Rippl. Architectures for Advanced RAIM: Offline and Online. In *Proceedings of the 27th International Technical Meeting of The Satellite Division of the Institute of Navigation (ION GNSS+ 2014)*, pages 787–804, Tampa, FL, 2014.
- [49] S. Perea, M. Meurer, M. Rippl, M. Belabbas and M. Joerger. URA/SISA Analysis for GPS and Galileo to Support ARAIM. *NAVIGATION, Journal of The Institute of Navigation*, 64(2):237–254, 2017.
- [50] Global Positioning System Directorate Systems Engineering and Integration. *Interface Specification IS-GPS-200*. Revision H, 2013. Available at <http://www.gps.gov/technical/icwg/IS-GPS-200H.pdf>.
- [51] M. Joerger, Y. Zhai and B. Pervan. Online Monitor Against Clock and Orbit Ephemeris Faults in ARAIM. In *Proceedings of the ION 2015 Pacific PNT Meeting*, pages 932–945, Honolulu, HI, 2015.
- [52] R. G. Brown and P. Hwang. *Introduction to Random Signals and Applied Kalman Filtering*. 4th Ed, Wiley, 2012.
- [53] J. Crassidis and J. Junkins. *Optimal Estimation of Dynamic Systems*. Chapman & Hall/CRC, 2004.
- [54] S. Malys, M. Larezos, S. Gottschalk, S. Mobbs, B. Winn, W. Feess, M. Menn, E. Swift, M. Merrigan and W. Mathon. The GPS Accuracy Improvement Initiative. In *Proceedings of the 10th International Technical Meeting of the Satellite Division of The Institute of Navigation (ION GPS 1997)*, pages 375–384, Kansas City, MO, 1997.
- [55] Y. C. Lee. A New Improved RAIM Method Based on the Optimally Weighted Average Solution (OWAS) Under the Assumption of a Single Fault. In *Proceedings of the 2006 National Technical Meeting of The Institute of Navigation*, pages 574–586, Monterey, CA, 2006.

- [56] Y. C. Lee, R. Braff, J. P. Fernow, D. Hashemi, M. P. McLaughlin and D. O. Laughlin GPS and Galileo with RAIM or WAAS for Vertically Guided Approaches. In *Proceedings of the 18th International Technical Meeting of the Satellite Division of The Institute of Navigation (ION GNSS 2005)*, pages 1801–1825, Long Beach, CA, 2005.
- [57] M. Orejas and J. Skalicky Clustered ARAIM. In *Proceedings of the 2016 International Technical Meeting of The Institute of Navigation*, pages 224–230, Monterey, CA, 2016.
- [58] T. Walter, J. Blanch and V. Kropp Satellite Selection for Multi-Constellation SBAS. In *Proceedings of the 29th International Technical Meeting of The Satellite Division of the Institute of Navigation (ION GNSS+ 2016)*, pages 1350–1359, Portland, OR, 2016.
- [59] M. Joereger. *Carrier Phase GPS Augmentation Using Laser Scanners and Using Low Earth Orbiting Satellites*. Ph.D. thesis, Department of Mechanical, Materials, and Aerospace Engineering, Illinois Institute of Technology, Chicago, IL, 2009.
- [60] S. Perea, M. Meurer, M. Rippl, M. Belabbas and M. Joerger and B. Pervan. URA/SISA Analysis for GPS-Galileo ARAIM Integrity Support Message. In *Proceedings of the 28th International Technical Meeting of The Satellite Division of the Institute of Navigation*, pages 735–745, Tampa, FL, 2015.
- [61] O. Montenbruck, U. Hugentobler, R. Dach, P. Steigenberger and A. Hauschild. Apparent clock variations of the Block IIF-1 (SVN62) GPS satellite. *GPS Solutions*, 16(3):303–313, 2012.